CONTROLS ON MASS AND THERMAL LOADING TO AN OIL SANDS END PIT LAKE FROM UNDERLYING FLUID FINE TAILINGS

A thesis submitted to the College of

Graduate and Postdoctoral Studies

In Partial Fulfillment of the Requirements

for the Degree of Doctor of Philosophy

In the Department of Civil, Geological,

and Environmental Engineering

University of Saskatchewan

Saskatoon

Canada

By

KATHRYN ANNE HEARSON DOMPIERRE

PERMISSION TO USE STATEMENT AND DISCLAIMER

In presenting this thesis in partial fulfillment of the requirements for a postgraduate degree from the University of Saskatchewan, I agree that the University libraries may make it freely available. I further agree that permission for copying this thesis in any manner, in whole or in part, for scholarly purposes may be granted by the professors supervising my thesis work or, in their absence, by the head of the Department of Civil Engineering or the dean of the College of Graduate and Postdoctoral Studies. It is understood that any copying, publication, or use of this thesis or parts thereof for financial gain shall not be allowed without my written permission. It is also understood that recognition shall be given to me and to the University of Saskatchewan in any scholarly use, which may be made of any material in my thesis. Requests should be addressed to:

Head of the Department of Civil Engineering
University of Saskatchewan
57 Campus Drive
Saskatoon, Saskatchewan S7N 5A9
Canada

OR:

Dean of the College of Graduate and Postdoctoral Studies
University of Saskatchewan
107 Administration Place
Saskatoon, Saskatchewan S7N 5A2
Canada

Reference in this thesis to any specific commercial products, process, or service by trade name, trademark, manufacturer, or otherwise, does not constitute or imply its endorsement, recommendation, or favoring by the University of Saskatchewan. The views and opinions of the author expressed herein do not state or reflect those of the University of Saskatchewan, and shall not be used for advertising or product endorsement purposes.

I certify that the version submitted is the same as that approved by my advisory committee.

ABSTRACT

End pit lakes (EPLs) are a relatively new strategy proposed for reclaiming oil sands surface mines. An EPL is formed within a depleted mine pit, with fluid fine tailings (FFT) stored below a water cover. Fluid fine tailings are a by-product of the oil sands bitumen extraction process with high water contents, low bearing capacities, and elevated concentrations of various constituents. This thesis considers mass and heat transfer between the FFT and overlying water cover at the first EPL, Base Mine Lake (BML). The study objectives were: (1) characterize the FFT thermal properties and the thermal regime in BML; (2) assess FFT settlement rates and characteristics; and (3) evaluate a range of potential mechanisms for mass and heat movement, including diffusion or conduction, and mixing of the FFT due to unstable density profiles or fluid movement within the water cover. These objectives were achieved through a combination of field investigations, laboratory testing, and numerical modelling, and the results were published in three manuscripts comprising the main body of the thesis. Overall, FFT is the largest (Cl) mass source to the BML water cover. The dominant transport mechanism was advective mass transport or convective heat transport due to tailings settlement; however, tailings disturbance near the FFT-water interface may also contribute to mass release. The predicted pore water fluxes based on the advective or convective regimes were similar to previously estimated FFT settlement rates and decreased throughout the studied period from approximately 1.46 m/a in 2013 to 2014, to 0.73 m/a in 2014 to 2015. Declining advection rates indicate that diffusive mass transport and conductive heat transfer will likely become more significant in the future. The results also confirmed that EPL design should consider the size of the water cover, volume and characteristics of the FFT, and operational controls, as these factors will likely influence EPL success as a sustainable reclamation landscape.

ACKNOWLEDGEMENTS

A heartfelt thank you to…

Lee Barbour, for sharing his wisdom and humility, allowing me to reach my own conclusions while unobtrusively guiding me in the right direction, helping me see the big picture, and acting as a true role model.

Matthew Lindsay, for providing valuable mentorship and advice, while patiently waiting to officially be my co-supervisor.

My advisory committee, Howard Wheater, Grant Ferguson, Andrew Ireson, and Karl-Erich Lindenschmidt, and committee chair, Bruce Sparling, for taking the time to share their knowledge and guide me through this process.

Syncrude Canada Ltd., NSERC, and the University of Saskatchewan Department of Civil and Geological Engineering, for funding my research, as well as the Global Institute for Water Security for providing office space and administrative support.

The Syncrude Canada Ltd. Environmental Research Team, for assisting with field work and logistics, allowing me to take part in the Base Mine Lake advisory group, and for their constant support and willingness to listen to my suggestions – especially Geoff Halferdahl and Janna Lutz.

My research colleagues in engineering, geology, soil science, and SENS, for providing laboratory assistance, technical advice, and general support throughout my thesis.

And my biggest cheerleaders, my family and friends, who were there every step of the way and have made me who I am today – especially Phil, Mom and Dad, Mark, Carly, Bobbi, and AJ/UC.

PERMISSION TO REPRODUCE

The second chapter of this thesis was originally published by the NRC Research Press in the *Canadian Geotechnical Journal* (Dompierre and Barbour, 2016*b*). The authors retain the copyright for manuscripts published by the NRC Research Press after 2009 so no further permission was required for the purposes of this thesis.

The third chapter of this thesis is reprinted from the *Journal of Contaminant Hydrology*, 189, K.A. Dompierre and S.L. Barbour, Characterization of physical mass transport through oil sands fluid fine tailings in an end pit lake: a multi-tracer study, 12-26, copyright (2016), with permission from Elsevier. License: 3943110164176.

TABLE OF CONTENTS

LIST OF TABLES

LIST OF FIGURES

LIST OF ABBREVIATIONS

^{2}H	deuterium
^{18}O	oxygen-18
AOSR	Athabasca oil sands region
BML	Base Mine Lake
CEMA	Cumulative Environmental Management Association
Ca	calcium
CH_4	methane
Cl	chloride
CO_2	carbon dioxide
COSIA	Canada's Oil Sands Innovation Alliance Inc.
EC	electrical conductivity
Eh	redox potential
EPL	end pit lake
Fe	iron
FIS	fixed interval sampler
FFT	fluid fine tailings
K	potassium
masl	metres above sea level
MLSB	Mildred Lake Settling Basin
Mg	magnesium
Na	sodium
NH_3	ammonia
OSPW	oil sands process water
P	platform
S	station
SO_4	sulfate
TMF	Tailings Management Framework
XRD	X-ray diffraction

LIST OF SYMBOLS

α_L longitudinal dispersivity (m)

λ thermal conductivity of the entire soil matrix – FFT in this case (W/m/K)

λ_b thermal conductivity of bitumen (W/m/K)

λ_g thermal conductivity of gas bubbles (W/m/K)

λ_s thermal conductivity of the soil solids (W/m/K)

λ_w thermal conductivity of the pore water (W/m/K)

$\emptyset_{cond}$ vertical conductive heat flux (J/m^2/s)

$\emptyset_{conv}$ vertical convective heat flux (J/m^2/s)

$\emptyset_z$ total vertical heat flux (J/m^2/s)

ρ_b density of bitumen (kg/m^3)

ρ_s density of the soil solids (kg/m^3)

ρ_w density of the pore water (kg/m^3)

C mass concentration of solute (mg/L)

C_v volumetric heat capacity of the entire soil matrix – FFT (J/m^3/K)

C_f volumetric heat capacity of the soil pore fluid (J/m^3/K)

c_b specific heat capacity of bitumen (J/kg/K)

c_s specific heat capacity of the solid particles (J/kg/K)

c_w specific heat capacity of the pore water (J/kg/K)

D^* coefficient of molecular diffusion (m^2/s)

D_h hydrodynamic dispersion in the direction of flow (m^2/s)

dM change in mass stored in the BML water cover (g)

dS net water flux over the BML water surface (m^3 or mm)

Ei exponential integral

f_b volumetric bitumen content of soil (volume of bitumen divided by the total volume)

f_g volumetric gas bubble content of soil (volume of gas divided by the total volume)

f_s volumetric solids content of soil (volume of solids divided by the total volume)

f_w volumetric water content of soil (volume of water divided by the total volume)

I_M total mass (Cl) associated with the BML inputs (g)

I_W total water contributed to BML from inputs (m^3 or mm)

J_{adv} advective mass flux (g/m^2/s)

J_{diff} diffusive mass flux (g/m^2/s)

J_z total vertical mass flux (g/m^2/s)

$M_{p_{in}}$ mass (Cl) associated with the pump-in water (g)

$M_{p_{out}}$ mass (Cl) associated with the pump-out water (g)

M_{prec} mass (Cl) associated with precipitation (g)

M_{pw} mass (Cl) associated with the FFT pore water released to the water cover (g)

M_{ro} mass (Cl) associated with runoff entering BML (g)

n porosity (m^3/m^3)

O_M total mass (Cl) associated with the BML outputs (g)

O_W total water removed by BML outputs (m^3 or mm)

q heating rate (W/m)

q_z vertical volumetric pore water flux (m^3/m^2/s)

r heating radius; distance between the heating wire and thermistor (m)

ΔT change in temperature (K)

T temperature (K)

t time (s)

t_0 time when heating stops (s)

V volume (m^3)

v_z vertical pore velocity (m/s)

z depth (m)

CHAPTER 1 – INTRODUCTION AND BACKGROUND

Development of the Canadian oil sands has expanded rapidly over the past 15 years. As of September 2015, there were over 140 operating oil sands projects, 11 under construction, and 20 more approved for development (Government of Alberta, 2016). Approximately 10.5 billion barrels of bitumen (1.7×10^9 m^3) had been extracted from the oil sands deposits by the end of 2014 (Alberta Energy Regulator, 2015).

Some of the largest and longest running projects are the surface mining operations located in the Athabasca oil sands region (AOSR), north of Fort McMurray, Alberta. In 2014, surface mining accounted for 45 % of bitumen produced from the oil sands (Alberta Energy Regulator, 2015). Surface mining involves the removal of vegetation, organic soils, and overburden materials (formations overlying the ore) to access the oil sands ore, which is then transported to upgrading facilities for bitumen extraction.

Fluid fine tailings (FFT) are a by-product of the bitumen extraction process. These tailings have high water contents, low settlement rates (Kasperski and Mikula, 2011), and contain elevated concentrations of salts, naphthenic acids, and residual bitumen and naphtha (Allen, 2008; Kavanagh et al., 2011). Rapid expansion in the AOSR has resulted in large stores of FFT, with more than 9.8×10^8 m^3 in tailings impoundments by 2013 (Government of Alberta, 2015).

In 2015, the Government of Alberta developed the Tailings Management Framework (TMF) for improved tailings management and reclamation practices to reduce FFT volumes and limit the associated environmental risks (Government of Alberta, 2015). The TMF encouraged innovation focused on the treatment and reclamation of FFT (Government of Alberta, 2015). Numerous strategies are being actively pursued by industry and are slowly being integrated into operational practices. Many of these strategies aim to improve the FFT geotechnical properties for placement in conventional terrestrial reclamation landscapes, including flocculent and coagulant addition, large-scale centrifugation, thin-lift drying, and mechanical FFT filtration (COSIA, 2012*a*).

An alternative strategy is to place FFT in a mined out pit below a water cover in an End Pit Lake (EPL). This reclamation method does not require FFT treatment prior to placement so the initial costs are relatively low (CEMA, 2012). In addition to providing storage for FFT, EPLs are expected to regulate downstream flow, develop a sustainable ecosystem, generate water of acceptable quality for release to natural waterways, and support other functions like recreational use (CEMA, 2012). The first EPL, Base Mine Lake (BML), was commissioned at a surface mining project north of Fort McMurray in 2012. Approximately thirty more EPLs have been proposed in the AOSR (Prakash et al., 2011),

1.1 Study Rationale

In the future, EPLs are expected to be an integral part of the closure landscape. The ability for an EPL to achieve a water quality allowing for outflow to natural systems depends on the long-term geochemical and thermal regimes within the lake water. The influence of the underlying FFT on these regimes is not well understood. Thus, an evaluation of the water, heat, and mass transfers between the FFT and overlying water cover is required to assess the conditions of BML during its development and to predict its long-term performance.

1.2 Background Information

A preliminary understanding of end pit lakes, the geotechnical and geochemical characteristics of FFT, and the BML site were necessary for developing the main study objectives. This section highlights the current literature on and understanding of these topics, and reviews the applicable mass and heat transport theory.

1.2.1 End Pit Lakes

Land disturbed by surface oil sands mining must be returned to an ‘equivalent capability’, as required by the Alberta Energy Regulator (BGC Engineering Inc., 2010; Province of Alberta, 2014). End pit lakes are one reclamation strategy proposed for reclaiming disturbed land. These features will be a central part of the closure landscape as they are expected to function as retention ponds, providing flow management and treating mine-affected water so an acceptable quantity and quality is released to natural water systems (CEMA, 2012). Many EPLs are also expected to provide storage for by-products created by the oil sands mining process.

An oil sands EPL is similar to a conventional mine pit lake in that it involves the creation of a water body in a depleted mine pit (Gammons et al., 2009). The characteristics of conventional mine pit lakes vary substantially depending on mining operations and the surrounding geology and hydrogeology. The pit lake shape often depends on the ore body structure. For example, diamond mines, and their associated pit lakes, are typically deep and conical as they follow the shape of the kimberlite ore body in which diamonds are found (Gammons et al., 2009). Pit lakes at precious or base metal mines and high-sulfur coal mines are often highly acidic due to the presence of sulfide minerals in the ore, and have elevated concentrations of dissolved metals (Balistrieri et al., 2006; Peinerud, 2003; Castro and Moore, 2000). Conversely, other types of open pit coal mines are associated with alkaline pit lakes when the surrounding groundwater and formation is calcium-rich and acts as a natural buffer (Denimal et al., 2005; Peinerud, 2003).

The current understanding of oil sands EPLs, particularly their ability to sustain a productive aquatic ecosystem, is fairly limited as the first oil sands EPL was established in 2012. Canada's Oil Sands Innovation Alliance Inc. (COSIA) is currently planning a Demonstration Pit Lakes Project to address many of the existing knowledge gaps (COSIA, 2012*b*). In general, conditions within an EPL are expected to depend on site-specific attributes (COSIA, 2012*b*), as observed for conventional pit lakes. Features influencing EPLs may include: (1) the lake surface area and depth; (2) ore characteristics; (3) the presence, volume and properties of tailings stored at the bottom of the pit; and (4) dominant water and mass sources to the water cover (Castendyk and Webster-Brown, 2007; Castro and Moore, 2000; Mian and Yanful, 2007; Peacey et al., 2002; Peinerud, 2003; Samad and Yanful, 2005).

1.2.2 Site Description

Syncrude Canada Ltd. has surface-mined oil sands ore since 1978. Their original mine, Base Mine, was decommissioned in 1994 and the leftover pit was divided and used to store tailings. Overburden, the material overlying the oil sands ore, and lean oil sands, ore with a bitumen content below 7 % (w/w), were left at the bottom of the pit. The overburden consists of marine shales and siltstones of the Clearwater Formation with a mean vertical hydraulic conductivity of approximately 8 $x10^{-10}$ m/s (Dallas Heisler, Syncrude Canada Ltd.). Lean oil sands are part of the McMurray Formation and have vertical hydraulic conductivity values ranging from 1 $x10^{-13}$ to 1 $x10^{-7}$ m/s (Dallas Heisler, Syncrude Canada Ltd.).

Fluid fine tailing were placed in the west portion of the Base Mine pit, called West In-Pit, beginning in 1994 (Figure 1-1). The FFT was dredged and pumped from another tailings impoundment, Mildred Lake Settling Basin (MLSB), into the northeast corner of West In-Pit (Geoff Halferdahl, Syncrude Canada Ltd.). The tailings would have filled the east side of West In-Pit until they overflowed a central mine haul road running north-south down the pit centre (Figure 1-1). The FFT temperature during placement was 11 to 19 °C. A 3 to 5 m OSPW water cap was present throughout the filling process, as West In-Pit provided water storage for the mine operations recycle water circuit. Tailings placement continued until 2012, when BML was commissioned as the first oil sands EPL. At this time, the maximum FFT depth was 45 m, corresponding to a total FFT volume of approximately 1.9 $x10^8$ m^3 (Geoff Halferdahl, Syncrude Canada Ltd.).

After BML was commissioned, fresh water was pumped from Beaver Creek Reservoir into the water cover to bring the surface elevation to 308.7 ± 0.5 metres above sea level (masl). This increased the water cover to an average depth of 8.5 m in 2013. Fresh water pumping from Beaver Creek Reservoir has continued during the ice-free months of 2013, 2014, and 2015 with yearly volumes ranging from 6 $x10^6$ to 7 $x10^6$ m^3 (Janna Lutz, O'Kane Consultants). Water was also removed from BML during these years for use in the bitumen extraction process and to maintain a consistent lake surface elevation. The average yearly volume of water pumped from BML was 6.5 $x10^6$ m^3. The lake covers an area of approximately 8 km^2 (Geoff Halferdahl, Syncrude Canada Ltd.).

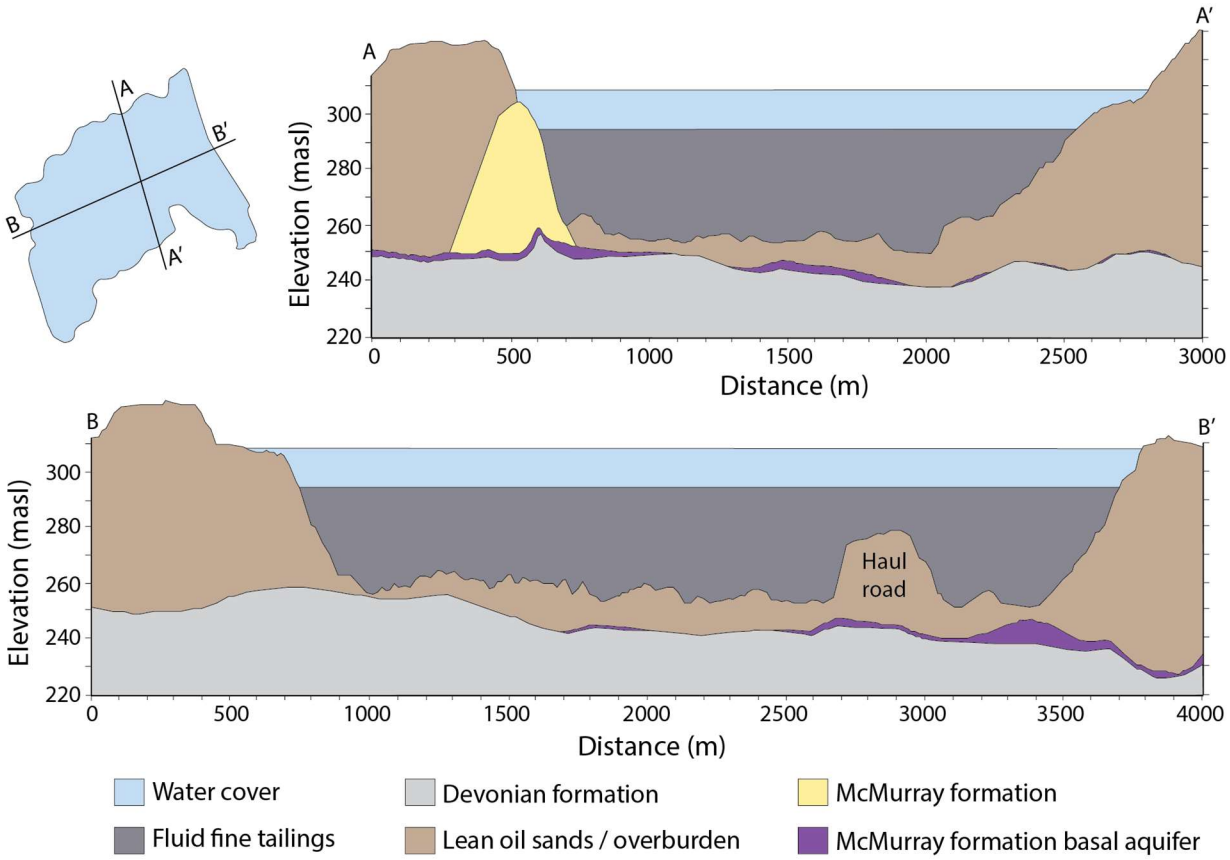

Figure 1-1. Cross sections of the West In-Pit geology – now the BML geology – including the approximate elevations of the FFT and water cover (based on information provided by Geoff Halferdahl, Syncrude Canada Ltd.).

1.2.3 Geotechnical Properties of FFT

When FFT is first generated, it is a dense, warm fluid suspension comprised of dispersed mineral particles and OSPW. The initial solids content of FFT is generally 25 % to 35 % (w/w) with a bulk density of approximately 1200 kg/m^3. As with other soft tailings, FFT has very low bearing capacities and shear strengths due to its high water content (Dimitrova and Yanful, 2012; Sarsby, 2000). Thus, conventional terrestrial reclamation is not suitable for FFT unless the tailings undergo preliminary strengthening. These properties also indicate that FFT stored under a water cover may be susceptible to erosion and resuspension, for example, by wind-induced waves or lake turnover (Adu-Wusu et al., 2001; Catalan and Yanful, 2002; Kachhwal et al., 2011). Thus, fluid movement within the water cap could cause rapid loading of sediment and/or dissolved constituents into the overlying water cap.

The FFT solids composition varies with the properties of the original oil sands ore (Osacky et al., 2013*a*); however, the solids are generally composed of quartz and clay minerals (Kasperski and Mikula, 2011). Tailings samples from multiple oil sands operations exhibited a large range in the relative quantities of these minerals, with clay contributing between 20 % and 80 % (w/w) of the FFT solids (Mikula et al., 2009). Previous studies have found that the clay minerals are predominantly kaolinite and illite with small portions of chlorite and smectite (Kasperski and Mikula, 2011).

Fluid fine tailings dewater gradually over time (Kasperski and Mikula, 2011), with the greatest settlement rates occurring within the first 3 to 4 years after deposition in a tailings impoundment (Siddique et al., 2011). Settlement occurs through self-weight consolidation. This form of consolidation occurs due to the internal weight of a soil (Been and Sills, 1981). Pore pressures with depth in an FFT deposit are initially equal to the total weight of the overlying fluid and solid suspension (Abu-Hejleh and Znidarčić, 1995) and consequently are greater than a hydrostatic pressure profile. The difference between the pore pressure through the FFT and the hydrostatic pressure profile is referred to as excess pore water pressure. The excess pore water pressure increases with depth in the FFT as the weight of the overlying solids suspension increases (Morgenstern and Nixon, 1971). Dewatering of the FFT is due to the dissipation of this excess pore pressure with a concomitant increase in effective stress (Abu-Hejleh and Znidarčić, 1995). Thus, dewatering predominantly occurs near the deposit bottom in early times. Consequently, the pore water flow generated by FFT dewatering was assumed to be relatively constant within the top portion of FFT as this region does not undergo significant settlement immediately following deposition.

The FFT constitutive properties change over time as dewatering occurs. In particular, hydraulic conductivity and compressibility may change nonlinearly with time as void ratio decreases (Gibson et al., 1981; Schiffman, 1982). The FFT properties also vary with depth due to the differential settlement occurring as a result of the increased internal load experienced by the FFT with depth (Sridharan and Prakash, 2003).

The hydraulic conductivity of the FFT is expected to range from 1 $x10^{-7}$ to 5 $x10^{-5}$ m/s based on the typical FFT water contents (or void ratios) in BML and previous laboratory results (Suthaker and Scott, 1996; Wong et al., 2008). Water expressed from the FFT generally moves upward through the tailings column, as the hydraulic conductivity of the

underlying formation is relatively low compared to the FFT. Pore water pressures measured in the field confirm that there is minor drainage from the pit bottom. The pore water movement generated through the FFT column is expected to obey Darcy's law as the water fluxes associated with tailings settlement produce Reynolds numbers substantially less than 1 ($<4 \times 10^{-7}$). This finding is consistent with finite strain consolidation theory, which assumes that the associated pore water flow follows Darcy's law (Schiffman and Pane, 1985). Thus, groundwater flow was assumed to be driven by FFT consolidation.

A preliminary numerical model was developed to simulate FFT dewatering in BML (Carrier et al., 2007). According to this model, FFT settlement would decrease exponentially from 1 m/a to approximately 0.1 m/a, over 30 years. The modelled results match the general trends observed during long-term FFT settlement analysis in the laboratory (Jeeravipoolvarn et al., 2009).

1.2.4 Geochemical Properties of FFT

A preliminary study of the FFT geochemical properties was completed prior to the three manuscripts comprising this thesis (Dompierre et al., 2016). This study provided background information on the FFT mineralogy and pore water characteristics that were fundamental to assessing mass and heat transfer in BML.

Fluid fine tailings pore water samples from BML were comparable to OSPW collected from other tailings impoundments (Allen, 2008; Stasik and Wendt-Potthoff, 2014). Electrical conductivity (EC) values within the FFT ranged from 3100 to 5400 μS/cm. The major dissolved constituents contributing to these values were determined to be sodium (Na), chloride (Cl), calcium (Ca), magnesium (Mg), potassium (K), and ammonia (NH_3). The pH was near-neutral and redox potential (Eh) indicated anoxic conditions throughout the FFT. The measured parameters exhibited variability with depth and by sampling location but provided insight on the potential biogeochemical reactions occurring in BML.

Pore water pH was observed to decrease below the FFT-water interface, which was assumed to be due to the production of methane (CH_4) and carbon dioxide (CO_2) by methanogenesis (Siddique et al., 2006, 2007, 2011). Hydrocarbon degradation via methanogenesis was expected given the residual bitumen and naphtha present in FFT (Fedorak et al., 2003; Siddique et al., 2006, 2007, 2011; Stasik et al., 2014; Stasik and Wendt-Potthoff, 2014). A reduction in pH likely promoted carbonate mineral dissolution as lower pH

values corresponded to increased concentrations of Ca and Mg. Dissolved Ca and Mg could be involved in exchange reactions with Na at the clay mineral surfaces. According to Siddique et al. (2014*a*) these exchanges would stimulate FFT settlement as Ca and Mg cause the electrical double layer associated with clay particles to decrease.

Conditions within the FFT pore water also suggested that microbial iron (Fe) and sulfate (SO_4) reduction were present near the FFT-water interface (Dompierre et al., 2016; Ramos-Padrón et al., 2011; Stasik et al., 2014; Stasik and Wendt-Potthoff, 2014). The subsequent formation of Fe^{2+} sulfides has been observed in FFT (Chen et al., 2013; Siddique et al., 2014*b*; Stasik et al., 2014), which Siddique et al. (2014*b*) suggested could mask the surface charge at clay mineral surfaces enhancing FFT settlement. Therefore, multiple biogeochemical reactions occurring within BML may contribute to FFT settlement and pore water release, affecting the movement of mass and heat.

1.2.5 Mass Transport Through the FFT

The governing equation for saturated, one-dimensional mass transport (after Bear, 1972) is:

$$\frac{\partial(C \cdot n)}{\partial t} = -\frac{\partial J_z}{\partial z} \tag{1.1}$$

where C represents mass concentration of the solute (mass per unit volume), n is the medium porosity (volume of pores per total volume of the medium), J_z is the vertical mass flux (mass per unit area per unit time), and *t* and *z* represent time and depth, respectively. For conservative mass transport where the species does not react with other dissolved constituents or the solid matrix, the mass flux term includes advection, mechanical dispersion, and molecular diffusion.

Advection is the movement of mass via fluid flow as described in following equation:

$$J_{adv} = C \cdot q_z \tag{1.2}$$

where J_{adv} is the vertical mass flux due to advection (mass per unit area per unit time), and q_z represents the vertical volumetric pore water flux (volume of pore water movement per unit area per unit time). In BML, FFT dewatering through self-weight consolidation generates vertical fluid flow. In addition to the pore water flux created by FFT dewatering, unstable

density profiles may also generate fluid movement that could contribute to advective mass transport.

Molecular diffusion occurs when a concentration gradient is present, with mass moving from areas of high concentration to low concentration. As observed in BML (Dompierre et al., 2016), the concentration of many different species is greater in the FFT pore water than the overlying water cap, creating diffusive gradients towards the FFT-water interface. Fick's First Law governs the diffusive mass flux, J_{diff}, according to:

$$J_{diff} = -D^* \cdot n \cdot \frac{\partial C}{\partial z} \tag{1.3}$$

where D^* is the coefficient of molecular diffusion for a solute of interest within the saturated porous medium (Domenico and Schwartz, 1998; Fetter, 1999; Incropera and DeWitt, 2002).

Mechanical dispersion represents mass spreading due to tortuous travel pathways and velocity distributions in the pores (Fetter, 1999). Mechanical dispersion acts in a similar manner to diffusion as it causes mass to spread during transport in proportion to concentration gradients. The coefficient of mechanical dispersion is assumed to be proportional to the pore velocity so it only occurs when flow is present; whereas diffusion is independent of flow.

Mechanical dispersion and molecular diffusion are often combined to create a term called the coefficient of hydrodynamic dispersion (Domenico and Schwartz, 1998). Hydrodynamic dispersion, D_h, in the direction of flow is defined as follows:

$$D_h = \alpha_L \cdot v_z + D^* \tag{1.4}$$

where α_L represents the longitudinal dispersivity (length) and v_z is the vertical pore velocity calculated by dividing the volumetric pore water flux (q_z) by the porosity (n). The first term in equation (1.4) represents mechanical dispersion. Hydrodynamic dispersion is substituted for D^* in equation (1.3) when there is water flow through the medium.

The total mass flux by advection, mechanical dispersion and molecular diffusion is:

$$J_z = [C] \cdot q_z - D_h \cdot n \cdot \frac{\partial C}{\partial z} \tag{1.5}$$

which can be substituted into equation (1.1) to produce the following governing equation for the transport of a conservative solute in a saturated porous medium:

$$\frac{\partial C \cdot n}{\partial t} = \frac{\partial}{\partial z}\left[D_h \cdot n \cdot \frac{\partial C}{\partial z}\right] - \frac{\partial C \cdot q_z}{\partial z} \tag{1.6}$$

The medium properties (e.g. porosity, hydrodynamic dispersion) are depth and time dependent because of FFT self-weight consolidation. Although both advection-dispersion and diffusion processes are included in equation 1.6, it is important to note that these processes do not generally act simultaneously; typically, mass flow is controlled by either advection and mechanical dispersion, or diffusion.

Methanogenesis within the FFT is known to generate CH_4 and CO_2 (Penner and Foght, 2010; Siddique et al., 2006, 2007, 2011). As these dissolved gases are transported upwards, they experience a decrease in surrounding fluid pressure. Ebullition, the formation of gas bubbles, occurs when the surrounding fluid pressure decreases sufficiently (Fendinger et al., 1992). The bubbles then migrate through the sediment column until they are released to the overlying water (Scandella et al., 2011). The movement of these gases over the FFT-water interface represents an additional form of mass transport present in BML; however, this study did not attempt to quantify gas production and release as a transport mechanism.

Various conservative tracers have been used to track mass movement through groundwater systems. Chloride has been used for many years to trace groundwater movement and seepage to lakes (Cox et al., 2007; Davis et al., 1980; Jacquet, 1976; Lee et al., 1980), and in mass transport studies, like the CFB Borden investigations on mechanical dispersion and the influence of scale (Sudicky and Illman, 2011). More recent studies have employed stable isotopes of water as a tracer for groundwater movement (Coplen et al., 2000) or mass transport (Barbour et al., 2012; McKay et al., 1993). A recent study conducted by Baer et al. (2016) catalogued the stable isotope of water signatures associated with natural and process water found in the AOSR.

1.2.6 Energy Transfer Through FFT

The general equation for one-dimensional heat transport is very similar to the one-dimensional equation for mass transport (Incropera and DeWitt, 2002):

$$\frac{\partial(T \cdot C_v)}{\partial t} = -\frac{\partial \emptyset_z}{\partial z} \tag{1.7}$$

where T represents temperature, and C_v is the volumetric heat capacity of the medium, which is the energy stored or released per unit volume for a one degree temperature change. The vertical heat flux, $\emptyset_z$, is energy transferred upwards or downwards, per unit time, per unit area. Heat transfer through the FFT in BML can occur as either conduction or convective heat transport.

Conduction is the transmission of heat from more energetic molecules to surrounding molecules with less energy (Rathore and Kapuno, 2011). Heat flux associated with one-dimensional (vertical) conduction, $\emptyset_{cond}$, follows Fourier's Law and can be determined by:

$$\emptyset_{cond} = -\lambda \cdot \frac{\partial T}{\partial z} \tag{1.8}$$

where λ is the thermal conductivity of the medium (energy per unit time, per unit length, per degree change in temperature; Domenico and Schwartz, 1998; Incropera and DeWitt, 2002).

Convection is heat movement via fluid flow. Free convection is fluid movement due to temperature gradients. Free convection occurs in systems where the density difference arising from temperature differences are sufficient to cause fluid flow. Forced convection is heat movement as a result of flow produced by hydraulic (mechanical) gradients (Pop and Ingham, 2001; Anderson, 2005). Forced convection may be present in BML due to FFT consolidation.

The general equation for heat flux associated with convective heat transport in groundwater systems, $\emptyset_{conv}$, is:

$$\emptyset_{conv} = T \cdot C_f \cdot q_z \tag{1.9}$$

where q_z is the vertical volumetric water flux associated with forced and free convection, and C_f is the volumetric heat capacity of the pore fluid.

Given these two forms of heat flux, the one-dimensional equation for simultaneous heat and fluid flow through a saturated porous medium is:

$$\frac{\partial[T \cdot C_v]}{\partial t} = \frac{\partial}{\partial z}\left[\lambda \cdot \frac{\partial T}{\partial z}\right] - C_f \cdot \frac{\partial[T \cdot q_z]}{\partial z} \tag{1.10}$$

Many of the variables in the one-dimensional heat transport equation will vary with depth and time in the BML context. The volumetric heat capacity and thermal conductivity will vary with depth and time due to changing FFT water contents with depth and time (Bristow, 1998; Cosenza et al., 2003; De Vries, 1963). The pore water flux is dependent on depth and time given the ongoing FFT self-weight consolidation, and may be affected by free convection if temperatures through the FFT cause significant density gradients. Temperature variation through the FFT is also expected, as a result of seasonal fluctuations in the temperature of the water cap.

Mechanisms controlling mass and heat transport are comparable, as evident by the similarities between their one-dimensional governing equations. Advective mass transport and convective heat transfer both occur due to fluid flow. Consequently, heat has been used to trace groundwater movement (Anderson, 2005; Bredehoeft and Papadopulos, 1965; Saar, 2011; Stallman, 1965). Conduction and hydrodynamic dispersion both occur due to variations in the characteristics of the solute (temperature or concentration). However, conductive heat transfer cannot be used as an indicator for diffusive mass transport as it is generally more effective in moving heat than diffusion is in moving mass.

In addition to temperature-related density differences, density gradients may form within the FFT due to variation in pore water chemistry or suspended solids contents. For example, FFT pore water generally has greater total dissolved solids than the water cap resulting in density gradients at the FFT-water interface. Multiple forms of density gradients may cause pore water movement in the FFT, subsequently influencing heat and mass transport. Thus, the movement of heat and mass are inherently linked and must be considered together.

There are several potential mechanisms contributing to heat and mass transport within the FFT of an EPL. These mechanisms are listed below.

(1) Advective mass transport (and dispersion) or convective heat transport
   - Pore water release from FFT self-weight consolidation with potential for enhanced settlement via biogeochemical reactions.
   - Density-derived fluid flow (free convection) as a result of unstable density profiles within the FFT, where density may be affected by temperature and solids content.

(2) Diffusive mass transport
   - Mass gradient at the FFT-water interface.

(3) Conductive heat transport
   - Temperature gradients through the FFT due to seasonal variation of lake temperatures.

(4) FFT disturbance or resuspension
   - Erosion of the FFT-water interface due to fluid movement within the water cap.

1.3 Research Objectives

The overall objective of this thesis was to characterize mass and energy movement from stored FFT to the overlying water cover during the first few years of EPL operation. Given the current understanding of BML, FFT, pit lakes, and mass and heat transport, the following specific objectives were defined:

(1) Determine the thermal properties of FFT using standard laboratory methods and a unique field-testing system developed for deployment at BML in order to consider the influence of water content, bitumen content, mineralogy, and gas bubbles on FFT thermal conductivity and volumetric heat capacity;

(2) Examine the dominant thermal regime in BML by measuring FFT temperatures over multiple seasons and developing heat transport numerical models to evaluate the mechanisms contributing to energy movement through the FFT, including forced and free convection, and conduction;

(3) Assess the rates and characteristics of FFT settlement to compare to predicted settlement rates and evaluate whether settlement is evenly distributed over the FFT surface, by measuring the movement of conservative tracers in the FFT pore water;

(4) Evaluate the relative importance of other mass transport mechanisms, including molecular diffusion and FFT mixing due to unstable density profiles or disturbances caused by fluid movement within the water cover, given the movement of conservative tracers through the FFT pore water; and

(5) Examine the overall mass loading from the FFT to the BML water cover using mass balance methods and numerical models for conservative mass transport.

These study objectives were addressed within three manuscripts, which have been combined to create the body of this thesis, according to guidelines provided by the College of Graduate Studies for a 'dissertation by manuscript' style thesis.

1.4 Thesis Structure

The three manuscripts are each presented as a single chapter following this introductory chapter. Each manuscript is presented in full as it was published, or in the case of the last manuscript, as it was submitted for publication, with minor modifications for editorial purposes only. The first manuscript, "Thermal properties of oil sands fluid fine tailings: Laboratory and field investigation", was accepted for publication in the *Canadian Geotechnical Journal* (Dompierre and Barbour, 2016*b*). The study explores the influence of bitumen and water content, FFT mineralogy, and gas bubbles on the thermal properties of FFT. The thermal properties were measured both in the laboratory and an in-situ assessment of the FFT, which used a specially-designed field testing system.

The second manuscript is entitled "Characterization of physical mass transport through oil sands fluid fine tailings in an end pit lake: A multi-tracer study" and has been published in the *Journal of Contaminant Hydrology* (Dompierre and Barbour, 2016*a*). This study investigated the movement of pore water, mass, and energy through the FFT in BML using stable isotopes of water and heat as tracers. Both field testing and numerical simulations contributed to the understanding reached in the study.

The final manuscript, "Chemical mass transport between fluid fine tailings and the overlying water cover of an oil sands end pit lake", has yet to be submitted for publication. This study evaluated the mass loading from the FFT using Cl as a conservative tracer to assess the mass balance of the water cover and to generate numerical models for simulating mass transport over the FFT-water interface.

Chapter 5 summarizes the overall conclusions of the complete body of research, and success of addressing each of the established research objectives. This chapter also includes recommendations for future research at BML and general implications to EPL design.

The appendices include supplemental informal on the numerical model design (Appendix A) and the pit capacity curve used for the mass balance calculations (Appendix B). Appendix C includes corrections or clarifications related to the published manuscripts, noted at the time of defence.

CHAPTER 2 – THERMAL PROPERTIES OF OIL SANDS FLUID FINE TAILINGS: LABORATORY AND FIELD INVESTIGATION (DOMPIERRE AND BARBOUR, 2016*b*)

An understanding of the FFT thermal conductivity and volumetric heat capacity were required to assess energy movement through FFT and to use heat as a tracer for pore water flow. The importance of bitumen and water content were considered by evaluating the FFT thermal properties in the laboratory using a dual heat pulse probe. Previously established equations for the thermal properties of saturated soils were modified to include a bitumen term and were compared to the laboratory results. Finally, an in-situ testing system was developed to assess FFT thermal properties in the field and evaluate the effect of gas bubbles.

I, Kathryn Dompierre, directed the field sampling program, measured the thermal properties of FFT in the laboratory, designed and installed the in-situ testing system, executed the field experiment, developed the numerical models (described in Appendix A), and completed data synthesis and analysis. I am the primary author of this manuscript. Matthew Lindsay and Jake Nesbitt (University of Saskatchewan) conducted the XRD mineralogy investigation including the phase identification. Preliminary advice on the University of Saskatchewan laboratory testing program was provided by Min Li and Bing Si (University of Saskatchewan). Geoff Halferdahl (Syncrude Canada Ltd.) coordinated the laboratory testing at the Syncrude Research Facility in Edmonton, which was completed by Jennifer McMillan and Amber Horan (Syncrude Canada Ltd.). I, Kathryn Dompierre (85%), carried out the majority of the contributions to the preparation of the manuscript with Lee Barbour (15%) assisting with the conceptualization of the in-situ test system, development of the numerical models, and providing comments during the review process.

This article was accepted for publication in the *Canadian Geotechnical Journal*: Dompierre, K.A., and Barbour, S.L. 2016*b.* Thermal properties of oil sands fluid fine tailings: Laboratory and in-situ testing methods. *Canadian Geotechnical Journal*, In Press, DOI: 10.1139/cgj-2016-0235.

2.1 Introduction

The bitumen extraction process associated with oil sands mining produces large volumes of fluid fine tailings (FFT). Fluid fine tailings are composed of dispersed, suspended mineral solids within a fluid matrix of oil sands process affected water and residual bitumen (Gosselin et al., 2010; Siddique et al., 2007). Oil sands operators are pursuing a range of strategies to incorporate FFT into reclaimed landscapes. One of these strategies is the creation of end pit lakes (EPLs), formed by placing FFT in depleted mine pits below a fresh water cap. There are currently thirty EPLs proposed for the Athabasca oil sands region, half of which will incorporate FFT (Prakash et al., 2011). Syncrude Canada Ltd. (Syncrude) has developed the first and only EPL to date, called Base Mine Lake (BML).

The hydrology of an EPL, particularly related to the thermal and chemical regimes within the water cap, is currently being studied. An important consideration is the energy movement from the FFT to the overlying water cap. The FFT in BML exhibits warmer temperatures than the average annual air and groundwater temperatures in the region; this temperature gradient causes conductive heat transfer from the FFT to both the overlying lake and underlying geologic formations. Therefore, the FFT will act as a heat source to the surrounding systems. The energy released from the FFT may influence the hydrological performance of the lake, for example the annual evaporation rates and the period of ice cover, as well as the conditions for the development of biotic activity.

In order to evaluate the thermal regime within the EPL, the thermal properties of FFT in BML must be quantified. Dompierre et al. (2014) and Li et al. (2015) conducted preliminary investigations on the thermal properties of FFT in the laboratory. These studies evaluated the relationship between water content and the thermal properties of tailings samples but did not consider other characteristics that may influence the thermal properties of FFT, such as the presence of organic matter (Abu-Hamdeh and Reeder, 2000).

The laboratory portion of this study is a continuation of the work presented in Dompierre and Barbour (2015), and thoroughly examines the thermal properties of FFT by evaluating the characteristics of the individual tailings components (mineral solids and organic content or bitumen). In addition to the laboratory work, a unique field-testing method was developed to investigate the large-scale thermal properties of undisturbed FFT in BML. Results from the laboratory and field tests provide a comprehensive understanding of the

thermal conductivity and volumetric heat capacity of FFT in BML, and can be used in future studies on heat migration and storage in EPLs.

2.2 Background Information

2.2.1 Site Description

Surficial mining of oil sands ore began in 1978 at Syncrude's Mildred Lake Mine, approximately 40 km north of Fort McMurray, Alberta. The oil sands ore is from the McMurray Formation, and generally contains an average of 0.25 (m^3/ m^3) bitumen (long chain hydrocarbons), 0.06 to 0.11 (m^3/ m^3) water, and 0.65 to 0.69 (m^3/ m^3) solids, typically comprised of quartz sand and clay (Chalaturnyk et al., 2002). Bitumen is removed from the ore through the addition of hot water to decrease the bitumen viscosity and sodium hydroxide (NaOH), also referred to as 'caustic', to disperse the clay particles (Caughill et al., 1993; Masliyah et al., 2004). The bitumen is then separated for upgrading and the remaining sand-clay slurry is pumped to tailings impoundments (e.g., Mildred Lake Settling Basin; Figure 2-1) for storage.

West In-Pit, a portion of the original mine pit, is one of the tailings impoundments at the Mildred Lake Mine site. Syncrude began filling West In-Pit in 1994 with FFT dredged from the Mildred Lake Settling Basin. The FFT was pumped into the northeast corner of the pit from 1994 to 2012. The FFT temperature during placement ranged from 11 °C to 19 °C. A water cap, comprised primarily of oil sands process water, was present throughout the entire filling period and ranged from 3 to 5 m in depth. The maximum FFT depth at the end of filling was approximately 45 m.

West In-Pit was commissioned as an EPL, referred to as BML (Figure 2-1), at the end of 2012. Since that time, freshwater has been pumped in from an adjacent freshwater reservoir (Beaver Creek Reservoir) to bring the lake up to a water surface elevation of approximately 308.5 metres above sea level (masl). The average lake water depth is approximately 8.5 m. Base Mine Lake covers an approximate area of 8 km^2 with monitoring stations (labels starting with 'S' in Figure 2-1) spread over this whole area. There are also three large floating platforms on BML (Figure 2-1), which are used for research and monitoring purposes.

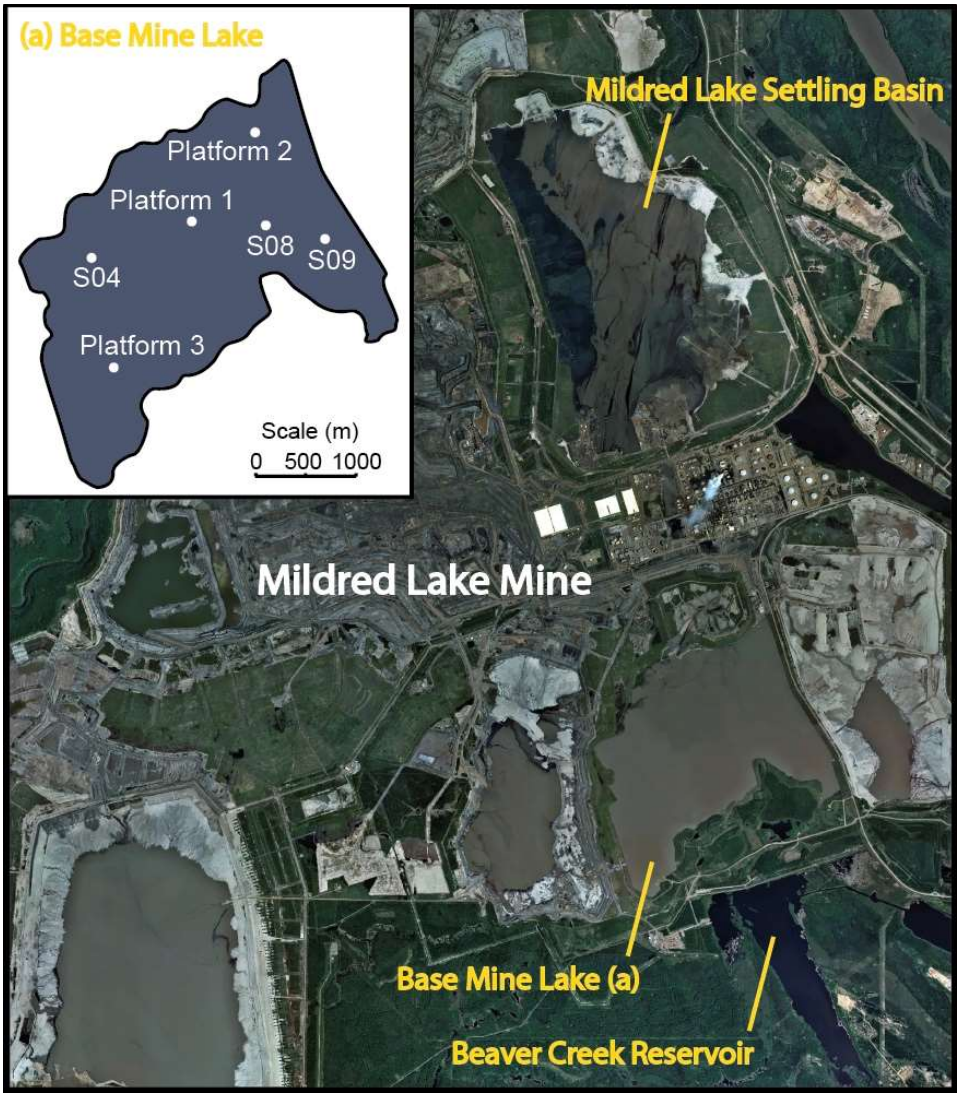

Figure 2-1. Aerial photo of the Mildred Lake Mine; inset (a) shows the BML monitoring stations.

The FFT in BML was initially placed with a solids content of approximately 0.35 (mass of solids divided by the mass of FFT), which corresponds to a solids volume fraction of approximately 0.2 (m^3/m^3). The FFT undergoes rapid dewatering during the first few years after discharge (Siddique et al., 2011), reaching a solids content of 0.50 or a volume fraction of 0.3 after several years; however, high water contents persist, taking many years to significantly dewater and eventually consolidate (Kasperski and Mikula, 2011). The slow settlement rates are attributed to the addition of dispersants (NaOH) during bitumen extraction, and naturally occurring surfactants (asphaltic acids) present in the ore that are

released during heating (Chalaturnyk et al., 2002; Jeeravipoolvarn, 2009). The FFT solids content in BML generally increases with depth due to self-weight consolidation and the extended FFT deposition period.

The FFT pore water has elevated concentrations of total dissolved solids representative of process-affected water (Allen, 2008) with electrical conductivity (EC) values of approximately 4000 μS/cm. The average FFT temperature in BML was determined to be 12.9 °C (Dompierre et al., 2016), with seasonal temperature variations in the water cap affecting the top 5 m of FFT (Dompierre and Barbour, 2016*a*). The average FFT temperature is greater than the average annual air temperature in the region (1 °C; Environment Canada, 2015) and the average shallow groundwater temperatures of 3 to 4 °C (personal communications, Dallas Heisler, Syncrude Canada Ltd.). The FFT also contains residual bitumen remaining in the tailings stream after the bitumen extraction process. Methanogenic bacteria utilize this organic substrate to generate methane gas, which is dissolved in the FFT pore water but may also form gas bubbles (Dompierre et al., 2016). Although the bubble formation process is not well understood, it is believed that ebullition occurs as the dissolved methane is transported upwards within the FFT. Bubbles form when the surrounding fluid pressures decrease sufficiently. The bubbles then migrate through the FFT and are eventually released to the overlying lake water.

2.2.2 Theoretical Relationships

Transient heat transport through a medium is controlled by two properties: (1) thermal conductivity; and (2) volumetric heat capacity. Thermal conductivity is the property controlling conductive heat transport as a result of temperature gradients, based on Fourier's Law. Volumetric heat capacity is the energy stored or released per unit volume of material during a temperature change, and is the product of the specific heat capacity and the density of a material.

The theoretical relationship for thermal conductivity of a saturated soil, established by Cosenza et al. (2003), is:

$$\lambda = \lambda_s^{\,f_s} \cdot \lambda_w^{\,f_w} \tag{2.1}$$

where λ is the thermal conductivity of the soil (W/m/K), λ_s is the thermal conductivity of the solid particles (W/m/K), and λ_w is the thermal conductivity of the pore water (W/m/K). The

thermal conductivity of each component is raised to a power defined by the volume fraction of that particular phase within the soil, where f_s is the solids volume fraction (m^3/m^3), and f_w is the water volume fraction or the volumetric water content (m^3/m^3).

The theoretical relationship for volumetric heat capacity was established by De Vries (1963) as the sum of the volumetric heat capacities of the individual components of a soil:

$$C_v = c_s \cdot \rho_s \cdot f_s + c_w \cdot \rho_w \cdot f_w \quad (2.2)$$

where C_v is the volumetric heat capacity of the soil ($J/m^3/K$), c_s is specific heat capacity of the solid particles (J/kg/K), and c_w is specific heat capacity of the pore water (J/kg/K). The density of the solids is represented by ρ_s (kg/m^3), and ρ_w is the density of the pore water (kg/m^3).

These general relationships for the thermal properties of soil were modified in this study to incorporate a third phase to account for the presence of bitumen, as Abu-Hamdeh and Reeder (2000) suggested that organic content influences the thermal properties of a soil. The modified theoretical relationship for thermal conductivity is:

$$\lambda = \lambda_s^{\,f_s} \cdot \lambda_w^{\,f_w} \cdot \lambda_b^{\,f_b} \quad (2.3)$$

where λ_b is the thermal conductivity of bitumen (W/m/K), and f_b is the volumetric bitumen content. The theoretical relationship for volumetric heat capacity becomes:

$$C_v = c_s \cdot \rho_s \cdot f_s + c_w \cdot \rho_w \cdot f_w + c_b \cdot \rho_b \cdot f_b \quad (2.4)$$

where c_b is the specific heat capacity of bitumen (J/kg/K), and ρ_b is the density of bitumen (kg/m^3).

Abu-Hamdeh and Reeder (2000) also suggest that soil salinity may affect its thermal properties. The effects of salinity could be incorporated into equations (2.3) and (2.4) by altering the pore water thermal conductivity, specific heat capacity, and density to represent water with elevated dissolved solids. However, Caldwell (1974) found that there was a limited difference in the thermal conductivities of freshwater and seawater at 20 °C. In addition, Millero et al. (1973) determined that an EC value of 4000 µS/cm (which corresponds to the average EC of FFT pore water) produced a water density that was 0.2% greater, and a specific heat capacity only 0.3% less than that of distilled water at 20 °C.

Previous laboratory studies on the thermal conductivity and volumetric heat capacity of soils have employed the dual heat pulse method (Bristow et al., 1994; Liu and Si, 2011). This method is based on the analytical solution for an infinite wire or line-source heating element (Kluitenberg et al., 1993). When an infinite heating source is applied to a soil, the change in temperature, ΔT (K), measured at a specified distance from the heating wire, r (m), will change over time, t (s), according to:

$$\Delta T(r,t) = \begin{cases} \frac{-q}{4\cdot\pi\cdot\lambda} \cdot Ei\left[\frac{-r^2\cdot C_v}{4\cdot\lambda\cdot t}\right] & 0 < t \leq t_0 \\ \frac{q}{4\cdot\pi\cdot\lambda} \cdot \left\{Ei\left[\frac{-r^2\cdot C_v}{4\cdot\lambda\cdot(t-t_0)}\right] - Ei\left[\frac{-r^2\cdot C_v}{4\cdot\lambda\cdot t}\right]\right\} & t > t_0 \end{cases} \quad (2.5)$$

where q is the heating rate (W/m), t_0 is the time when heating stops (s), and Ei is the exponential integral. For the dual heat pulse method, the distance, r, in the above equation is the distance between the surface of the line source heating element and the thermistor. This distance is often referred to as the heating radius as heat moves radially from the line source heating element into the soil. Equation (2.5) was the theoretical basis for the initial research on the thermal properties of FFT by Li et al. (2015).

2.3 Methodology

Fluid fine tailings samples were analyzed in the laboratory to determine the general physical characteristics of FFT as well as the thermal conductivity and volumetric heat capacity of FFT and its individual components. Following the laboratory analysis, a field testing method was developed to determine the in-situ thermal properties of FFT in BML. Numerical modelling was also undertaken to interpret the in-situ testing results. These methods are described in the following sections.

2.3.1 General FFT Properties Analysis

Samples were collected vertically, every 1 to 3 m to the pit bottom at 6 locations (Platform 1, Platform 2, Platform 3, S04, S08, and S09; Figure 2-1) in July 2014. The samples were collected with a pneumatic piston sampling system operated by ConeTec Investigations Ltd. A sample chamber with a pneumatic piston was positioned at the desired depth, the cable-actuated ball-valve on the chamber was opened, and the pneumatic piston was slowly retracted to allow FFT to enter the chamber. The ball valve was closed when the chamber was full, the sample system was brought up to the surface, and the collected sample was

transferred to a high-density polyethylene bottle. Samples collected by the described method were considered disturbed, due to the fluid nature of FFT. The EC of each sample was measured with a YSI Pro30 conductivity probe (YSI Incorporated, Yellow Springs, Ohio, USA) immediately after the sample was collected. Each sample was divided into two parts so that samples could be sent to both Syncrude and the University of Saskatchewan for analysis.

Syncrude conducted laboratory testing to determine the physical characteristics of the collected FFT at their research facility in Edmonton. The Dean and Stark extraction method was used to assess the bitumen, water and solids content of each sample (Dean and Stark, 1920). Dry solids obtained from this process (separated from the bitumen and water) were analyzed with a Coulter LS 13 320 laser diffraction particle analyzer (Beckman Coulter Canada LP., Mississauga, ON, Canada) to determine the particle size distribution of each sample (after ASTM, 2015*b*; ASTM, 2014*a*). The dry solids from three FFT samples were also analyzed at the University of Saskatchewan to determine their specific gravity according to ASTM standard D854-14 (ASTM, 2014*b*). The density of the bitumen isolated by the Dean and Stark extraction method (and separated from the associated toluene with a rotary evaporator) was measured using a DMA 4500M density meter (Anton Paar Canada Inc., Montreal, QC, Canada) according to ASTM standards D5002-15 (ASTM, 2015*c*) and D4052-15 (ASTM, 2015*a*).

X-ray diffraction (XRD) was performed at the University of Saskatchewan on the dry solids from seven FFT samples with a Co Kα1 source (1.78901 Angstroms), and a Fe beta filter at 45 mA and 40 kV. A 3-80° 2θ step size and counting time of 50 minutes were used to collect the XRD patterns. Powder diffraction patterns were obtained for randomly-oriented bulk samples, prepared by grinding dry FFT solids (retrieved from the Dean and Stark extraction method) to a fine powder in an agate mortar and pestle, which were then mounted on a glass slide. Phase identification was performed with Match! (v. 2.3.3), using the Crystallography Open Database (Gražulis et al., 2009).

2.3.2 Laboratory Evaluation of the Thermal Properties of FFT

Seven FFT samples were selected to represent a range of bitumen contents while other characteristics (EC, water content and particle size distribution) were relatively consistent (Table 2-1). Syncrude determined the physical characteristics of the selected samples according to the methods described in the previous section. The seven FFT samples had

bitumen volume fractions ranging from 0.017 to 0.086. The volumetric water content of the selected samples ranged from 0.694 to 0.800, with EC values between 850 and 1020 µS/cm (Table 2-1).

Table 2-1. Summary of FFT samples for thermal analysis.

Sample Location	**Bitumen Content** (m^3/m^3)	**Water Content** (m^3/m^3)	**Electrolytic Conductivity** (µS/cm)
Platform 1 - 10.5 m	0.017	0.800	1020
S08 - 10.5 m	0.027	0.791	850
Platform 1 - 40.5 m	0.034	0.733	900
Platform 3 - 34.5 m	0.041	0.694	860
Platform 1 - 9.5 m	0.047	0.784	950
Platform 1 - 12.5 m	0.058	0.732	990
Platform 3 - 28.5 m	0.086	0.707	860

The selected samples were all divided into four sub-samples before the thermal properties were analyzed. Each sub-sample was wetted with deionized water or dried to create a range of water contents. This was done to evaluate the effects of volumetric water content and volumetric bitumen content on the thermal conductivity and volumetric heat capacity of FFT.

The thermal conductivity and volumetric heat capacity of the sub-samples were measured with the KD2 Pro thermal properties probe (Decagon Devices Inc., Pullman, WA, USA) using the dual heat pulse method as employed by Bristow et al. (1994), Kluitenberg et al. (1993), and Liu and Si (2011), in compliance with ASTM standards (ASTM, 2014*c*). The thermal properties of each sub-sample were measured 5 times and the average values were assumed to be representative. The probe calibration was checked every 100 readings with materials of known thermal properties (provided by Decagon Devices Inc.). The EC of each sub-sample was measured with a ThermoScientific Orion Star conductivity meter (Thermo Fisher Scientific, Waltham, MA, USA) to determine if salinity effects should be taken into consideration. The EC meter was cleaned regularly and calibrated with NIST traceable buffer solutions. Once the thermal properties and EC analysis was complete at the University of

Saskatchewan, sub-samples were sent to Syncrude to confirm the bitumen, water and solids contents using the Dean and Stark extraction method, as previously discussed.

The thermal properties of the individual FFT components (solids and bitumen) were also analyzed. Seven dry FFT solids samples were assessed with the KD2 Pro thermal properties probe to determine the thermal conductivity and volumetric heat capacity of the solids alone. Syncrude measured the thermal properties of pure bitumen with the Hot Disk Thermal Constants Analyzer (HOT Disk Inc., Gothenburg, Sweden), using the methods outlined in ISO 22007-2 (ISO, 2015).

2.3.3 In-Situ Thermal Properties Testing

The field test design was similar to the laboratory heat pulse probe in that it produced a line-source heat pulse within the FFT, and was also comparable to the borehole thermal conductivity testing method developed by Raymond et al. (2010) for designing ground-coupled heat pump systems. The heating wire was composed of an insulated copper wire, carrying the electrical current down through the lake water to the FFT, connected to a 3 m non-insulated nickel alloy wire to produce a vertical heat pulse within the tailings (Figure 2-2). Preliminary testing of the non-insulated nickel alloy wire was conducted in the laboratory to assess the potential for current loss in the field. The non-insulated wire was placed in a saltwater bath (with and without a ground), and the wire was connected to a power source. A current loss of 0.5% or less was observed over a 3 m section of the non-insulated nickel alloy wire in the laboratory confirming that the wire would not exhibit a large current loss in the field. Thus, the non-insulated nickel alloy wire was considered a suitable material for in-situ heating of the FFT.

A high-resolution thermistor string (±0.1 °C), purchased from RST Instruments Ltd. (Maple Ridge, BC, Canada), was placed beside the heating wire system in order to measure the temperature change within the FFT during in-situ testing. The distance between each thermistor and the heating wire was measured before the system was deployed; however, these distances were difficult to control, and varied from 0.0005 to 0.0021 m prior to installation. The thermistors were positioned every 0.1 m along the 3 m heating wire.

The heating wire and thermistor string were hung from two small buoys that sat right at the FFT-water interface (Figure 2-2). Two 2.3 kg spherical weights with a diameter of 0.1 m were placed at the bottom of the heating wire and thermistor string to ensure the system

stayed vertical. A rope connected this system to a large buoy at the lake surface. The rope was left slack so that waves at the lake surface would not disturb the positioning of the heating system. The large buoy was designed to support the entire system if the two small buoys at the FFT-water interface were compromised. The insulated wire and thermistor line ran up to Platform 3 (Figure 2-1), where the thermistor string was connected to a flexDAQ data logger (RST Instruments Ltd.) on the platform.

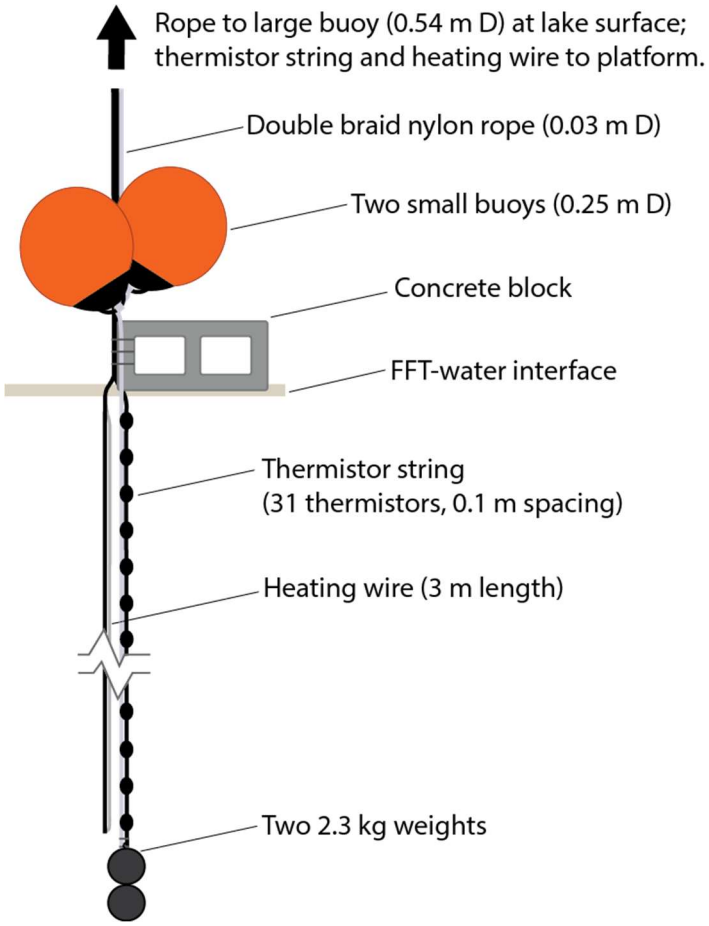

Figure 2-2. In-situ thermal properties testing system.

During the heating test, the ends of the insulated wire were attached to a Circuit-Test Electronics (Burnaby, BC, Canada) Regulated DC Power Supply (0-30 VDC, 0-3 A) set up on Platform 3 to generate the desired energy input. Two ammeters measured the current going into and out of the heating wire to determine the current lost through the system. A voltmeter was also used to measure the voltage over the entire system. A preliminary heating test with a

30-minute heating period was completed to ensure the system was properly set up. The full heating test ran for 2 hours, with temperatures measured by the high-resolution thermistor string at 1-minute intervals during heating, and every 3 minutes afterwards while the FFT cooled. The heating test was repeated to verify the results.

2.3.4 Development of the Numerical Model

In order to evaluate the FFT thermal conductivity and volumetric heat capacity using the in-situ heating test described above, the heating and cooling trends measured in the field were simulated in GeoStudio© TEMP/W, a commercial numerical modelling software package (GEO-SLOPE International Ltd., Calgary, AB, Canada; GEO-SLOPE International Ltd., 2014). A three-dimensional axisymmetric domain with a radius of 0.5 m was created to represent the FFT surrounding the heating wire. The vertical extent of the domain was 5 m centered on the 3 m heating wire with 1 m regions above and below the heating wire to represent the overlying lake water and underlying FFT, respectively. The middle region of the model had continuously changing volumetric water content with depth to represent the observed increase in solids content with depth through the FFT in BML. The thermal conductivity and volumetric heat capacity were set as functions of the water content so they also changed continuously with depth in the model. The initial thermal conductivity and volumetric heat capacity values in the FFT were specified based on findings from the laboratory portion of this study.

A thermal flux (W/m^2) was applied to the portion of the domain that represented the heating wire. The flux was calculated from the current and voltage measurements taken in the field. The heating flux was applied for the same time as the in-situ experiment (2 hours), followed by a cooling period of 4 hours. Simulated temperatures were compared to the in-situ experiment results at each thermistor by calculating the Root Mean Square Error (RMSE). The properties of the FFT beside the heating wire were modified until the minimum average RMSE value was determined for all thermistors.

2.4 Results and Discussion

2.4.1 General FFT Properties

The FFT samples collected throughout the entire FFT profile at the three sample locations had solids volume fractions between 0.117 and 0.631, bitumen volume fractions

between 0.001 and 0.088, and EC values ranging from 30 to 2403 µS/cm. Bitumen content does not exhibit a consistent trend with depth at any of the sample locations; however, the solids content of FFT in BML generally increases with depth (Figure 2-3). The variability in measured solids content between locations is likely due to differences in depositional history (e.g. time of FFT placement). For example, locations closer to the FFT discharge point have had greater time for dewatering to occur.

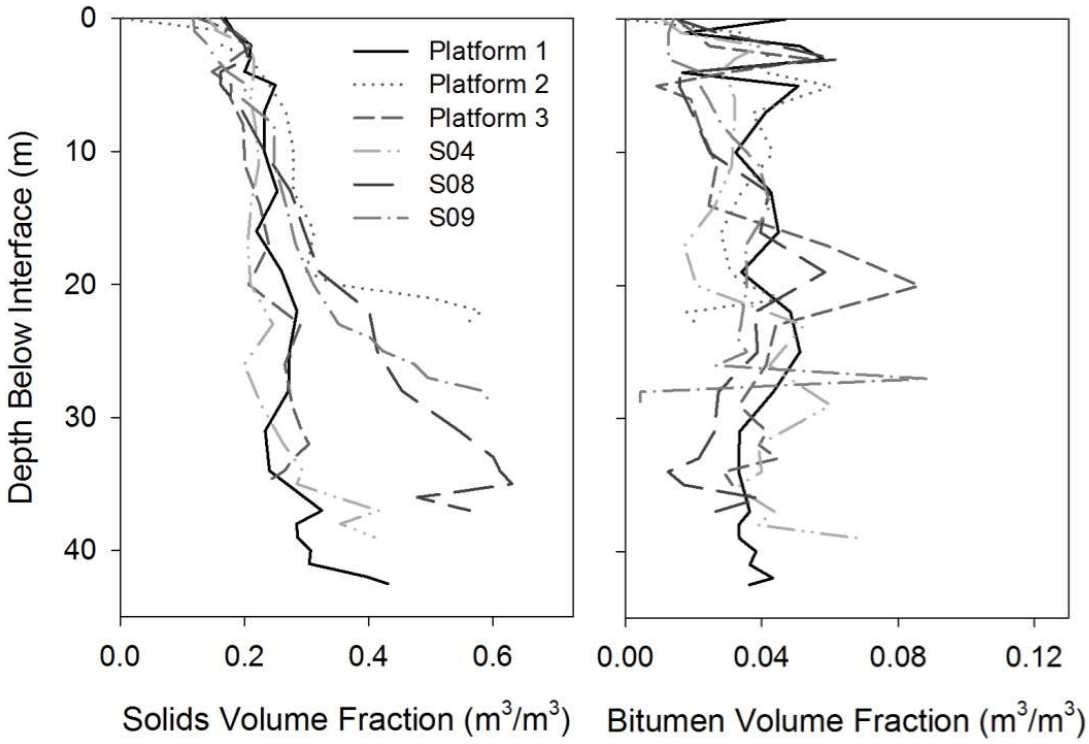

Figure 2-3. Solids and bitumen volume fractions through the FFT with depth.

The specific gravity of the dry FFT solids was determined in the laboratory to be 2.4 (the average value of three samples). This specific gravity is slightly lower than the typical values for non-organic soils (2.65; Li et al., 2015; Ren et al., 2003). The particle size distribution of the FFT solids was quite consistent (Figure 2-4). At least 90% of the FFT solids are typically less than 44 µm in diameter and 30% are less than 2 µm in diameter. There were no consistent trends in the particle size distribution with depth through the FFT.

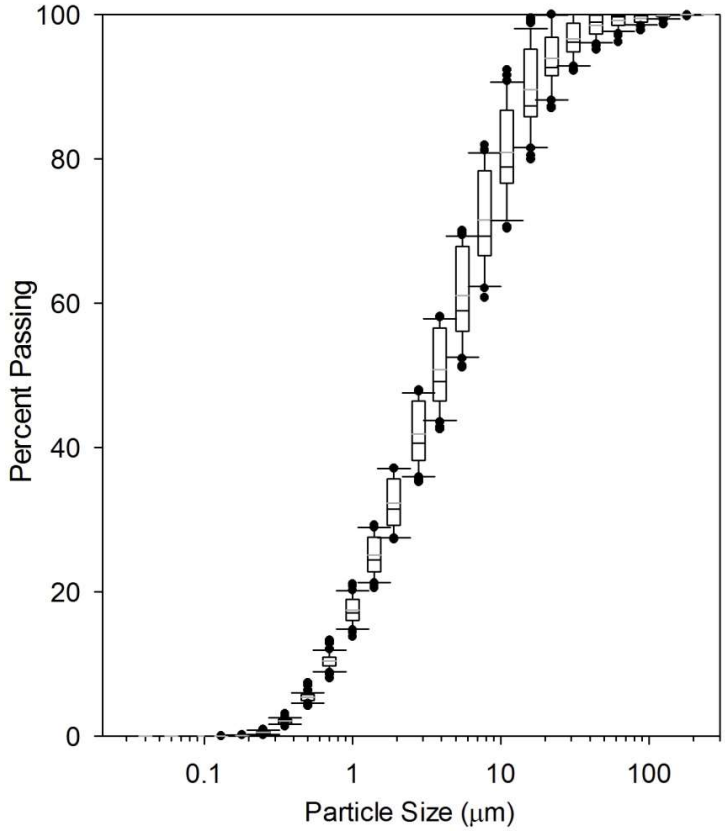

Figure 2-4. Particle size distribution of the 36 FFT sub-samples as box plots illustrating the interquartile range (box), median values (black lines), mean values (grey lines), 10th and 90th percentile values (whisker caps) and outliers (black circles).

Powder XRD analysis showed that the mineralogy was generally similar for all FFT samples (Figure 2-5). Quartz and clay minerals including kaolinite, chlorite and illite were present in the FFT. Two lower-intensity peaks positioned at approximately 35° 2θ and 37° 2θ were attributed to calcite and siderite, respectively. Peaks corresponding to quartz, kaolinite, chlorite, illite, calcite and siderite were observed in all FFT samples; however, the peak intensities were not the same for all samples, suggesting that the relative abundance of each mineral varied slightly. In addition, a minor peak positioned at approximately 38° 2θ was identified as pyrite (as indicated in Figure 2-5) but this peak was not observed for every sample. In general, kaolinite was the dominant mineral phase present in all samples, followed by quartz and illite. Based on the assessed mineralogy, the specific gravity of the FFT solids

was expected to be higher than the value measured in the laboratory and closer to 2.65 (Fredlund and Rahardjo, 1993; Spellman and Whiting, 2014). The XRD results generally agree with previous studies on the mineralogy of oil sands ore and FFT solids (Dompierre et al., 2016; Osacky et al., 2013*a*, 2013*b*).

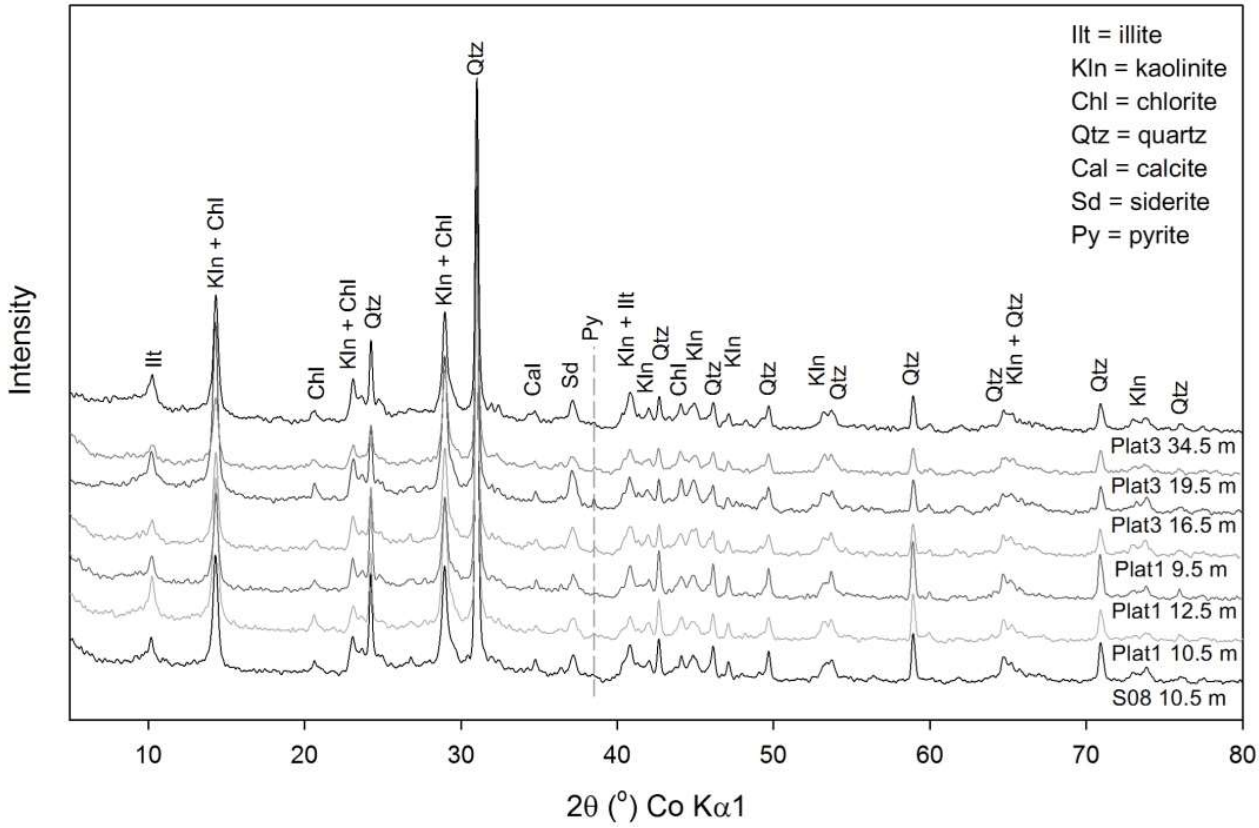

Figure 2-5. Powder XRD analysis results with an offset between the measured intensities of each sample for comparison purposes.

2.4.2 Laboratory Analysis of Thermal Properties

The volumetric water content, bitumen content, and EC varied between sub-samples due to the addition or removal of water during sub-sample preparation (Figure 2-6). The bitumen volume fraction of the sub-samples ranged from 0.010 to 0.077. These values were slightly lower than the original bitumen content range (Table 2-1) as some bitumen may have been lost during sub-sample preparation. For example, bitumen would coat the sides and lids

of the HDPE sample bottles so it was difficult to transfer all of the bitumen to the sub-sample containers.

The EC values of the sub-samples measured at the University of Saskatchewan were also different than those determined by Syncrude for the original seven samples (Table 2-1) likely due to sample preparation. The EC of the sub-samples ranged from 1641 µS/cm to 2919 µS/cm. These values were below 4000 µS/cm so the effect of dissolved solids on pore fluid density, heat capacity, and thermal conductivity was expected to be minimal (Caldwell, 1974; Millero et al., 1973).

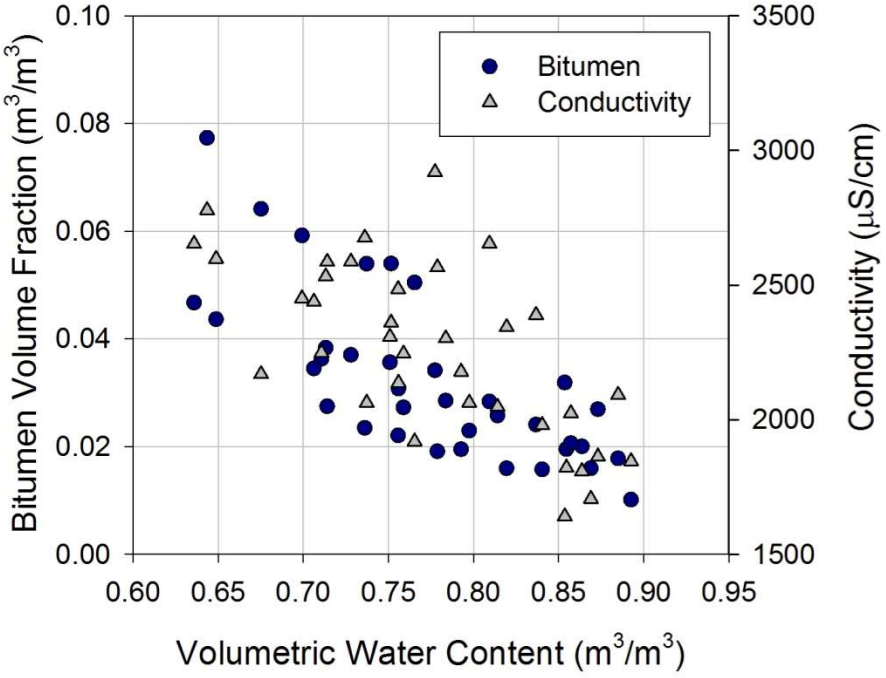

Figure 2-6. Bitumen volume fraction and EC of sub-samples as a function of water content.

The thermal conductivity and volumetric heat capacity of the individual components of FFT (dry solids and bitumen) were generally similar to results from previous studies (Table 2-2). The average thermal conductivity of the dry solids measured in the lab (3.1 W/m/K) had a standard deviation of 0.5 W/m/K and was within the expected thermal conductivity range for dry soil solids (Côté and Konrad, 2005; Farouki, 1981). This value was consistent with the thermal conductivities of the dominant minerals found in the FFT samples (Midttømme et al., 1998). This result also confirmed that soil structure has a negligible influence on the FFT

thermal conductivity, as the ratio between the thermal conductivity of water (0.57 W/m/K) and the thermal conductivity of the dry solids was greater than 1:15 (Côté and Konrad, 2009).

The average specific heat capacity of the dry solids (1087 J/kg/K) had a standard deviation of 68 J/kg/K and was higher than the results presented by Li et al. (2015). One possible reason for this discrepancy could be the observed overestimation of specific heat values using the dual heat pulse probe method (Liu et al., 2012; Ren et al., 2003; Song et al., 1998). The specific heat capacity value was multiplied by the density of the FFT solids (based on the specific gravity) to obtain a volumetric heat capacity of 2.61 $x10^6$ $J/m^3/K$ for the dry solids. When compared to the heat capacities of the dominant minerals present in the FFT (Bertoldi et al., 2007; Gailhanou et al., 2012; Richet et al., 1982; Robie and Hemingway, 1991), this value was slightly above the expected range.

Table 2-2. Thermal conductivity, specific heat capacity and density of the FFT components.

Parameter	Value
λ_s	3.10 W/m/K
λ_w	0.57 W/m/K*
λ_b	0.17 W/m/K
c_s	1087 J/kg/K
c_w	4182 J/kg/K*
c_b	1339 J/kg/K
ρ_s	2400 kg/m^3
ρ_w	998 kg/m^3 *
ρ_b	1030 kg/m^3

*Based on known values for water at 20°C

The thermal conductivity and volumetric heat capacity of the bitumen in the FFT (0.168 ± 0.001 W/m/K and 1.379 ± 0.029 $x10^6$ $J/m^3/K$) were similar to values determined for other long chain hydrocarbons, for example, heavy oils (Cerventes-Espinosa et al., 2012; Elam et al., 1989; Plantier et al., 2008; Wu et al., 2005). According to Gray (2015), the thermal conductivity of oil sands bitumen is 0.16 W/m/K, which corresponds to the laboratory results. The measured bitumen density (1030 kg/m^3) was slightly higher than the values found by Gray (2015) for raw bitumen (1000 kg/m^3) and Plantier et al. (2008) for heavy oils (approximately 1010 kg/m^3). In-situ biogeochemical reactions observed within the Mildred

Lake Settling Basin (Penner and Foght, 2010), where the FFT was originally stored, and BML (Dompierre et al., 2016), typically consume the lighter hydrocarbons present in FFT (Siddique et al., 2006, 2007). Thus, the bitumen remaining in FFT will be denser than the raw bitumen studied by Gray (2015). The bitumen specific heat capacity was calculated from the density and volumetric heat capacity values.

The measured thermal conductivities of the sub-samples ranged from 0.70 to 1.02 W/m/K. The thermal conductivity of each sub-sample was plotted with a symbol size representative of its associated bitumen volume fraction (Figure 2-7). The standard deviation of the five thermal conductivity values measured for each sub-sample ranged from 0.0004 to 0.0066 W/m/K with an average standard deviation of 0.0014 W/m/K. The thermal conductivity values of the individual components of FFT (Table 2-2) were used in equation (2.3) to create theoretical trend lines for the relationships between thermal conductivity and volumetric water content (Figure 2-7).

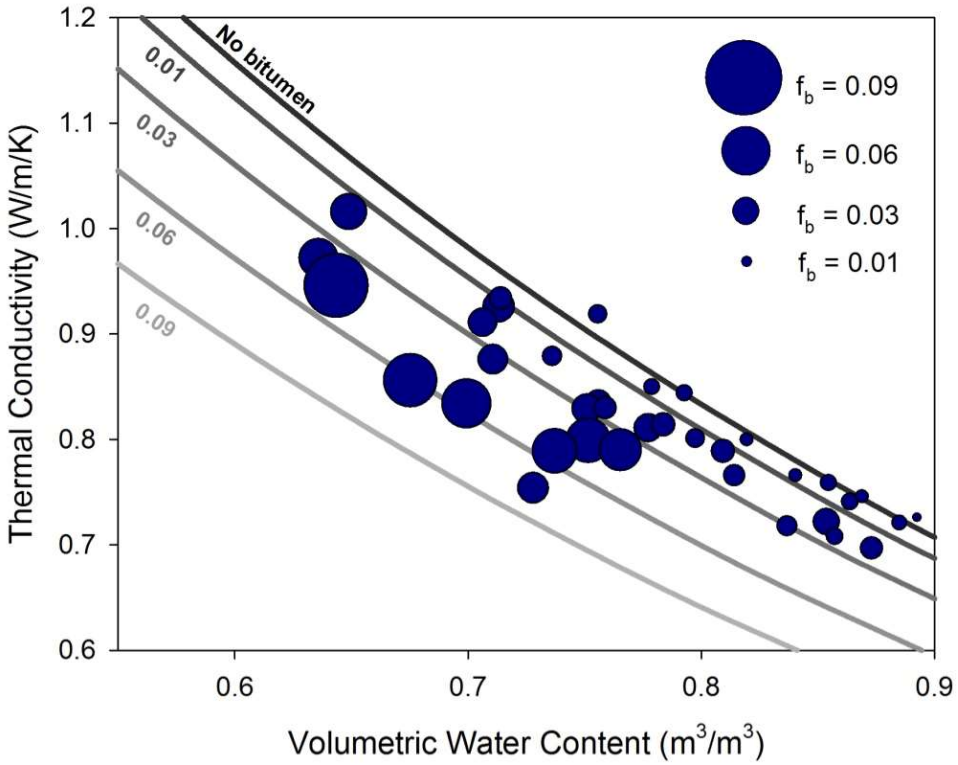

Figure 2-7. Measured thermal conductivities (circular symbols) and theoretical trends (lines) for multiple bitumen volume fractions.

The theoretical curves indicate that thermal conductivity decreases as the bitumen volume fraction increases. The measured bitumen contents generally followed the theoretical trends, as sub-samples with lower bitumen contents fall along the theoretical trend line calculated for no bitumen or a bitumen volume fraction of 0.01, and sub-samples with greater bitumen contents are between the theoretical trend lines for bitumen volume fractions of 0.03 and 0.09. There are a few sub-samples that appear somewhat anomalous; for example, the sample with the greatest bitumen content (0.077) appears to have a thermal conductivity that is too high for the associated water content. The thermal conductivity of this sample could have been abnormally high if a portion of the bitumen had coalesced. During laboratory testing, the measured thermal conductivity would have been greater (reflecting a lower bitumen content) if the portion of the sample with higher bitumen content was not near the probe.

Theoretical thermal conductivity values were calculated for each sub-sample given its physical composition and equation (2.3). The measured thermal conductivities of the sub-samples were plotted against the theoretically derived values (Figure 2-8). The data points follow the 1-1 line, confirming that the theoretical equation provided a reasonable fit for the measured values. The RMSE was calculated to determine the overall deviation of the measured thermal conductivities from the theoretical values. The RMSE associated with this data set was relatively low (0.06 W/m/K) confirming that the developed relationship (equation (2.3)) could be used to estimate the FFT thermal conductivity with known volumetric water and bitumen contents.

The measured volumetric heat capacities of the sub-samples ranged from 3.09 to 3.88 $x10^6$ $J/m^3/K$ (Figure 2-9). The standard deviation of the five volumetric heat capacities measured per sub-sample ranged from 0.08 to 1.19 $x10^4$ $J/m^3/K$, with an average value of 0.30 $x10^4$ $J/m^3/K$. Theoretical trends for volumetric heat capacity were calculated for several bitumen volume fractions using the parameter values provided in Table 2-2 and equation (2.4). Similar to thermal conductivity, volumetric heat capacity decreases as bitumen content increases. However, the spread between the theoretical relationships (at a given water content) is less for volumetric heat capacity suggesting that bitumen has a greater effect on the thermal conductivity of FFT than on volumetric heat capacity.

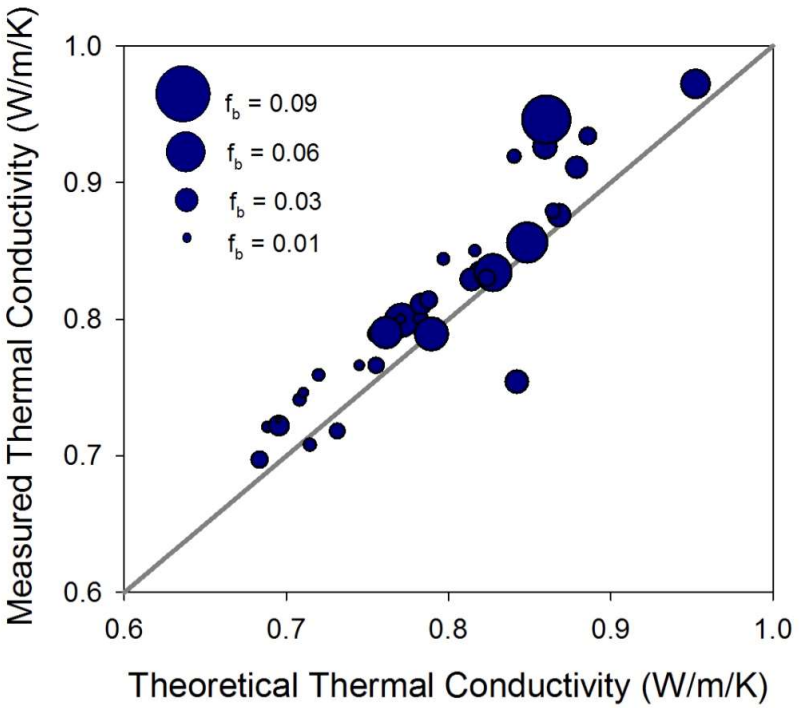

Figure 2-8. Comparison of measured and theoretical thermal conductivity values.

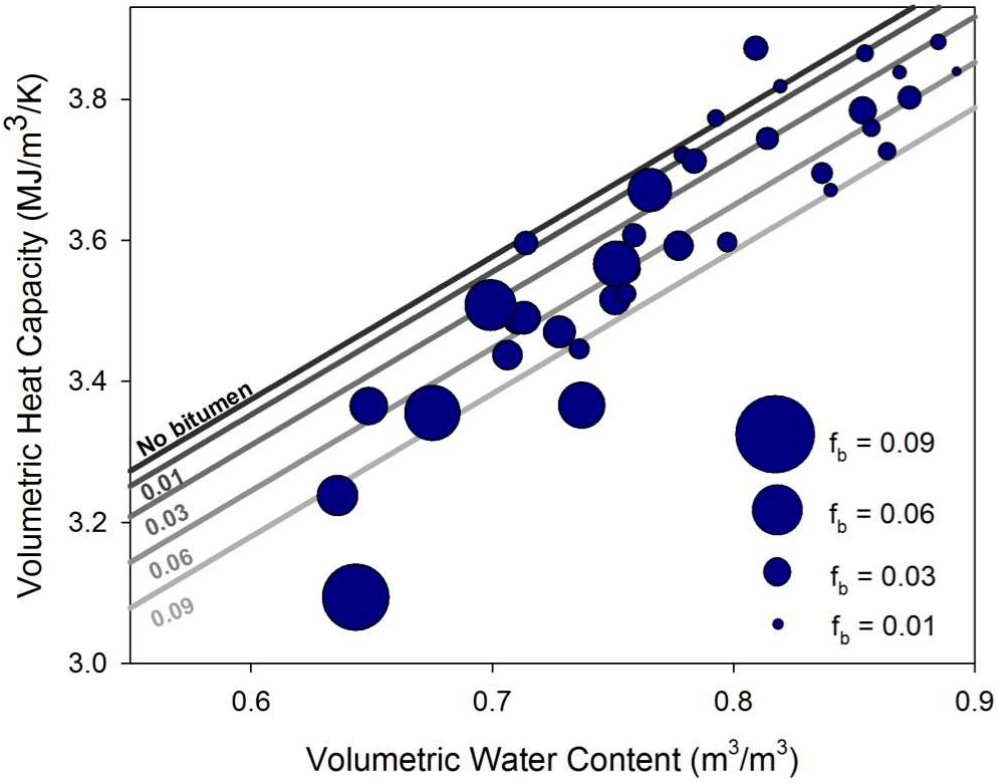

Figure 2-9. Measured volumetric heat capacities (circular symbols) and theoretical trends (lines) for multiple bitumen volume fractions.

The measured bitumen volume fractions generally followed the theoretical trends, as sub-samples with lower bitumen contents fall along the theoretical trend lines calculated for a bitumen volume fraction of 0.01, and sub-samples with greater bitumen contents have volumetric heat capacities below the theoretical trend lines for 0.06 bitumen. As with thermal conductivity, there are a few sub-samples that appear to be anomalous, such as the sample with a bitumen content of approximately 0.03, sitting above the theoretical trend for FFT with no bitumen, and the sample with the highest bitumen content that appears to have a volumetric heat capacity that is too low. These discrepancies could have been due to testing errors caused by sample heterogeneity, as described for the anomalous thermal conductivity values.

The measured volumetric heat capacities were plotted against theoretically derived values (dark symbols; Figure 2-10). The RMSE between the measured and theoretical values for volumetric heat capacity was determined to be 0.16 x10^6 J/m^3/K. The results indicate that the correlation is better at high values of volumetric heat capacity (i.e. high water contents) with greater deviation from the 1:1 line at lower water contents (and higher bitumen and solids contents). The observed offset between the measured and theoretical results could be caused by an underestimation of the laboratory measurements or an overestimation of the theoretical values. Previous studies found that the dual heat pulse probe method overestimates the heat capacity of soil (Liu et al., 2012; Ren et al., 2003; Song et al., 1998), so it is unlikely that the laboratory measurements underestimated the FFT heat capacity.

A sensitivity analysis was conducted by independently varying the density and specific heat capacity of the FFT components (solids and bitumen) within a reasonable range based on previous literature values. These values were then used in the theoretical relationship for volumetric heat capacity (equation (2.4)) in place of the original values (Table 2-2). The RMSE was calculated to compare these new theoretical values for volumetric heat capacity to the measured data set. For example, the solids particle density was increased up to 2650 kg/m^3 to calculate volumetric heat capacity as this value corresponds to the typical densities of the dominant minerals present in FFT (Fredlund and Rahardjo, 1993; Li et al., 2015; Ren et al., 2003; Spellman and Whiting, 2014). The bitumen density was also modified to 1000 kg/m^3, as this was the value provided by Gray (2015) for raw Athabasca bitumen.

The specific heat capacity of the dry FFT solids was decreased to 700 J/kg/K to correspond to measurements presented by Li et al. (2015).

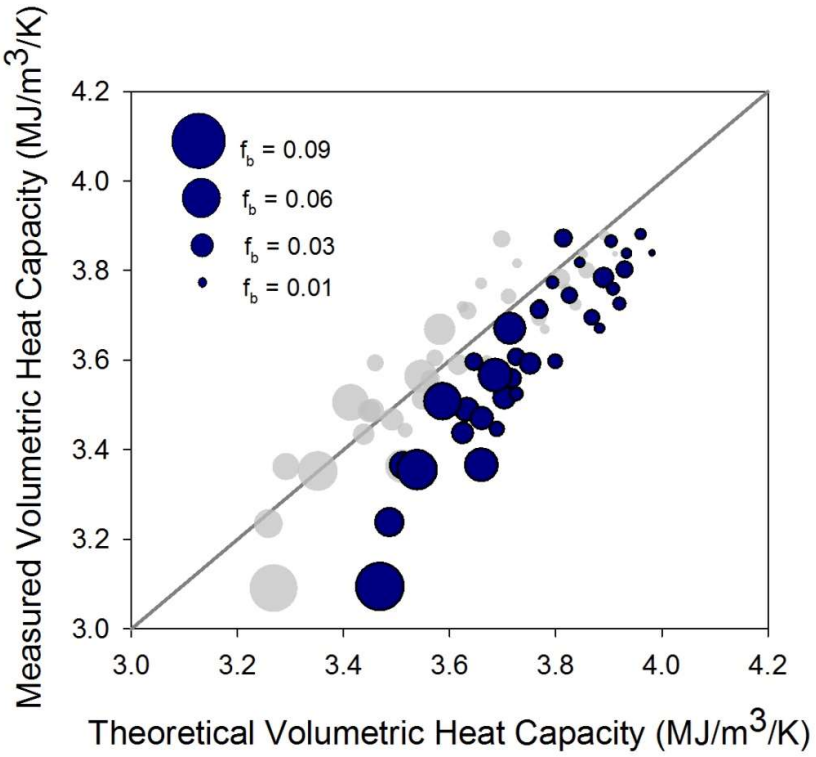

Figure 2-10. Comparison of measured and theoretical volumetric heat capacities with the theoretical values based on the original parameters (dark circles) and values after the sensitivity analysis (light circles).

The parameter with the greatest impact on the calculated volumetric heat capacity was the specific heat capacity of the dry FFT solids. When the value for the solids specific heat capacity was modified from 1087 to 700 J/kg/K, the measured and theoretical values fall along the 1-1 line with a RMSE of 0.07 x10^6 J/m^3/K (light symbols; Figure 2-10). This value corresponds to the FFT specific heat capacity determined by modulated differential scanning calorimetry (Li et al., 2015). This method generally provides more accurate values for the specific heat of soils compared to the dual heat pulse probe method (DeLapp et al., 2004; Liu and Si, 2011).

The laboratory results were used to estimate the approximate shifts in FFT thermal conductivity and volumetric heat capacity given the observed bitumen and water content

ranges (Table 2-3). Overall, water content was found to have a greater impact on the FFT thermal properties; however, the influence of bitumen cannot be disregarded. Bitumen content had a substantial impact on the FFT thermal conductivity and a small effect on the volumetric heat capacity.

Table 2-3. Relative importance of water and bitumen contents on the thermal properties of FFT.

Variable	**Measured Range** (m^3/m^3)	**Effect on Properties** (% change)
Water Content	0.64 – 0.89	λ: - 35% C_v: + 15%
Bitumen Content	0.01 – 0.08	λ: - 22% C_v: - 6%

The solids contents measured with depth through the FFT (Figure 2-3) were used to produce a solids content envelope, representing the minimum and maximum solids volume fractions expected through the FFT in BML (Figure 2-11). The solids content envelope was utilized to predict the range of expected FFT thermal conductivities and volumetric heat capacities with depth. The predicted range in thermal properties was calculated given: (1) a range of bitumen volume fractions (0 to 0.08) representative of the field results; (2) the corresponding volumetric water content; and (3) the theoretical relationships established for thermal conductivity and volumetric heat capacity. The parameter values listed in Table 2-2 were used in the theoretical relationships, except for the heat capacity of the FFT solids, which was altered to 700 J/kg/K. Both the thermal conductivity and volumetric heat capacity ranges (shaded regions; Figure 2-11) exhibited a sharp shift near the FFT-water interface. Below 0.5 m, thermal conductivity and volumetric heat capacity changed gradually with depth.

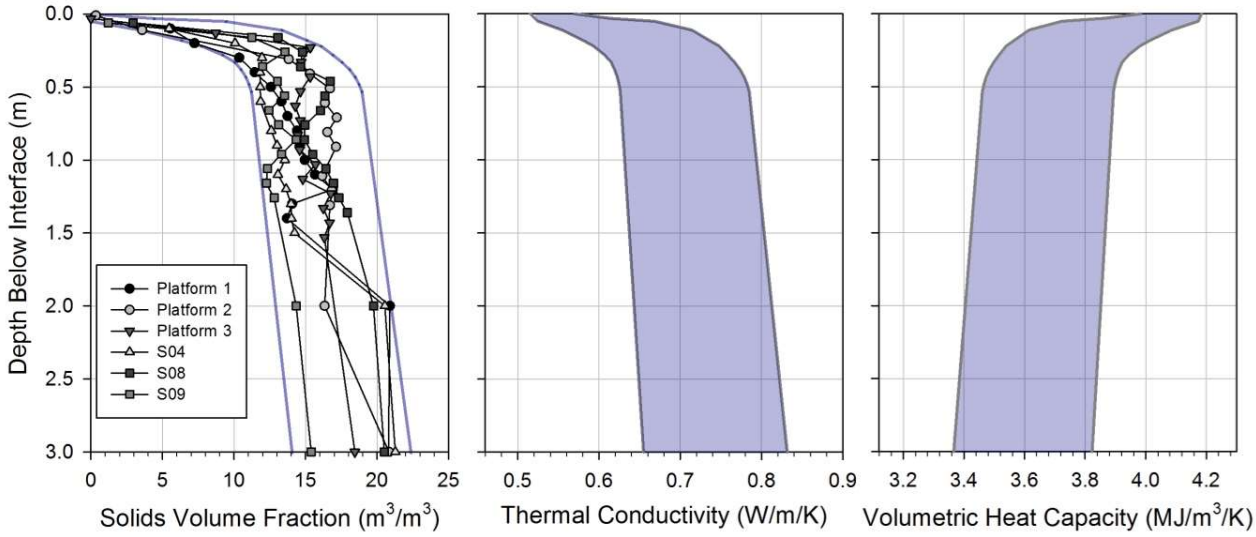

Figure 2-11. Solids content envelope (blue lines) and predicted range of thermal conductivity and volumetric heat capacity values (shaded regions) within the top 3 m of FFT.

2.4.3 In-situ Experiment Results and Numerical Analysis

2.4.3.1 Field Measurements

The current and voltage of the heating system remained fairly consistent throughout the in-situ thermal properties testing, with average values of 2.62 ± 0.02 A and 12.27 ± 0.10 V, respectively. The average current lost over the system during heating was 0.22%, and was assumed to be negligible. The heating rate for both of the in-situ tests was similar and was approximately 9.0 W/m.

The FFT temperature increased when the heating wire was connected to the power supply and decreased when the power was shut off after 2 hours (Figure 2-12). The initial temperature corresponded to the temperature at depth in the FFT, which was generally warmer near the FFT-water interface. Each thermistor measured a distinct heating and cooling trend based on the initial FFT temperature, the thermistor's distance from the heating wire (i.e., the heating radius), and the thermal properties of the FFT at that depth. The shape of the measured heating and cooling curves was consistent with the analytical solution for an infinite wire or line-source heating element (equation (2.5); Kluitenberg et al., 1993).

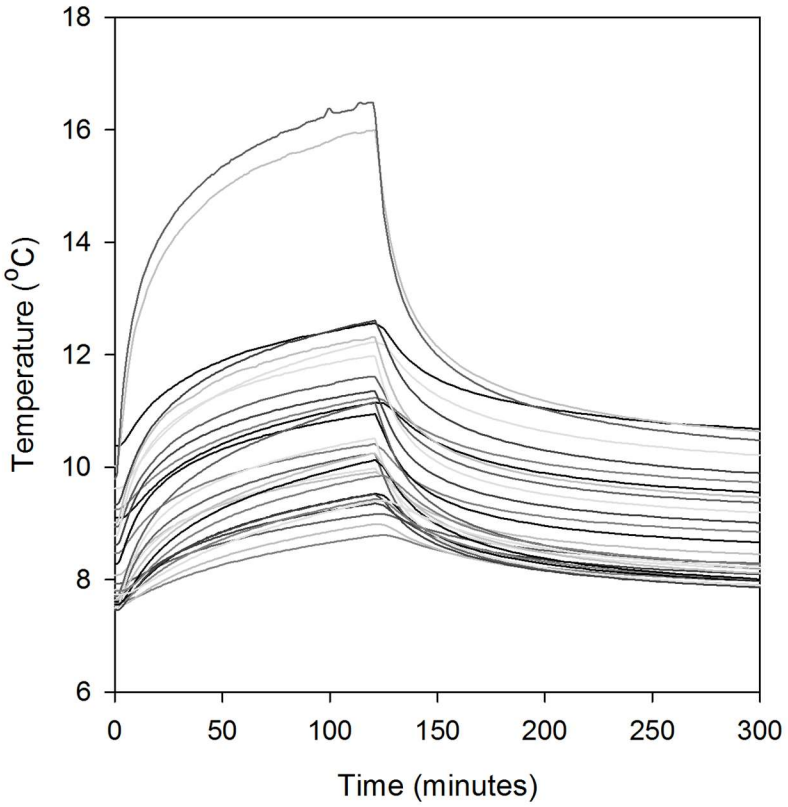

Figure 2-12. Heating and cooling curves measured in the FFT at all thermistors during an in-situ thermal properties test.

Although the heating wire produced temperature curves exhibiting the expected shape, the peak temperature change measured at each thermistor at the end of heating did not correspond to the peak temperature change calculated with equation (2.5). The expected peak temperature change was determined by inputting the measured heating radius at each thermistor and the expected thermal properties values, based on the laboratory results, into equation (2.5). The peak temperature change measured in the FFT at the end of heating was generally lower than the calculated peak temperatures. The presence of small vertical temperature gradients, due to the initial temperature profile and varying thermal properties with depth, could have contributed to the observed discrepancy between the in-situ measurements and the analytical solution, supporting the need for a numerical model to simulate the entire FFT profile.

2.4.3.2 Numerical Modelling

The peak temperatures generated by the numerical model were also compared to the analytical solution for a line-source heating element (equation (2.5); Kluitenberg et al. 1993). A preliminary simulation was run with constant properties (initial temperature, thermal conductivity and volumetric heat capacity) with depth. The peak temperatures produced by this simulation and equation (2.5) were consistent, given the same heating rate, thermal properties, heating radius, and heating period (2 hours). This comparison verified that the numerical model follows the dual heat pulse probe theory (Bristow et al. 1994; Kluitenberg et al. 1993; Li et al. 2015; Liu and Si 2011).

The numerical model was then run with a range of volumetric heat capacities (2.5 to 4.1 MJ/m^3/K), while the other variables remained constant (heating rate, heating radius, heating period, and thermal conductivity). These simulations were repeated for multiple thermal conductivity values, ranging from 0.6 to 1.0 W/m/K (Figure 2-13).

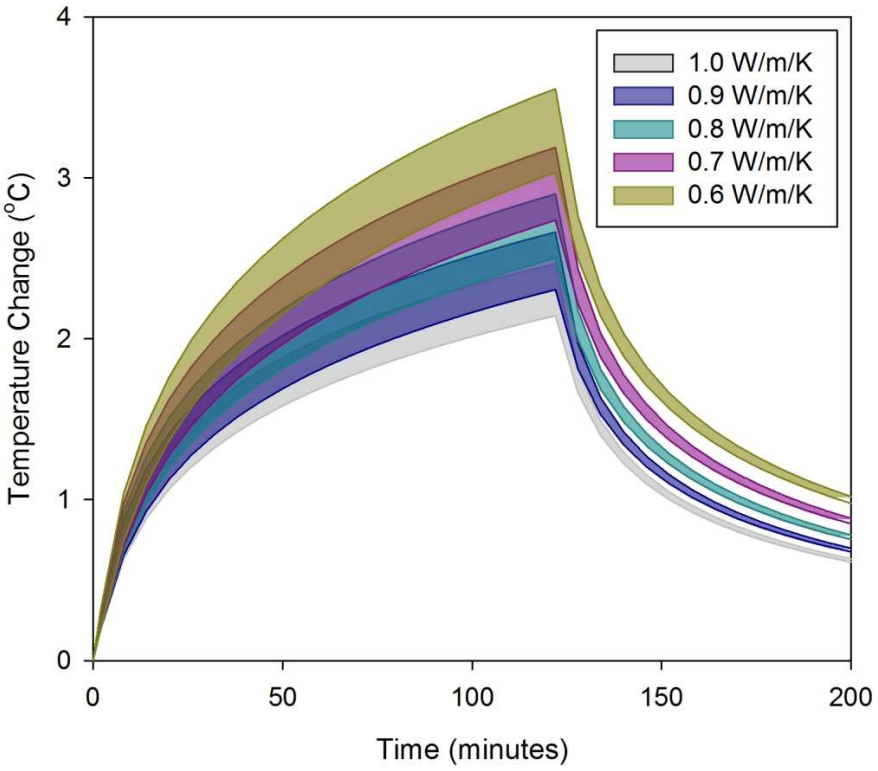

Figure 2-13. Simulated range in temperature change 0.005 m from the heating wire given a range in volumetric heat capacities (2.5 to 4.1 MJ/m^3/K) for each of the specified thermal conductivity values.

During the heating portion of the simulation, the range in temperature change generated by a given thermal conductivity (and range of volumetric heat capacities) overlapped with the results generated by lower and higher thermal conductivities. Therefore, different combinations of thermal conductivity and volumetric heat capacity could produce similar temperature curves during the heating portion of the simulation. Alternatively, there was minimal overlap between the temperature change results, for each thermal conductivity, during the cooling portion of the simulation even though a range of volumetric heat capacities was used. The simulated cooling trends indicated that volumetric heat capacity has a limited effect on the temperature change during this portion of the in-situ experiment.

2.4.3.3 Model Calibration to Field Data

The initial thermal properties used for calibrating the numerical model were based on the results from the laboratory portion of the study. The thermal conductivities and volumetric heat capacities inputted with depth corresponded to the median values of the thermal properties trends illustrated in Figure 2-11. The FFT temperature change was computed at a range of heating radii (0.002 m to 0.020 m), as the distance between the thermistor and heating wire of the in-situ testing system varied with depth (0.0005 to 0.021 m).

The simulation results were compared to the heating and cooling curves measured in the field. As with the analytical solution, the peak temperature change measured in the field was generally lower than the simulated temperature at the end of the 2-hour heating period. However, the simulated temperatures during the cooling portion of the experiment were relatively similar to the in-situ measurements (Figure 2-12). Only the thermistors with a heating radius within the simulated range (0.002 to 0.020 m) were included in this comparison (Figure 2-14).

Heating radius strongly influenced the simulated temperature change immediately after cooling began. Each radius (other than 0.002 and 0.004 m), exhibited a distinct temperature change with depth five minutes after cooling was initiated. As cooling continued, the difference in the temperature change generated by the various radii decreased. Fifty minutes after cooling started, the temperature change simulated at the smallest and largest radii differed by approximately 0.2 °C. The field measurements exhibited a similar trend. Five minutes after cooling began, the in-situ temperature change varied substantially with depth;

however, the measured range decreased as time progressed. Raymond et al. (2011) made the same observation when conducting thermal response tests for measuring borehole thermal properties associated with ground-coupled heat pump systems.

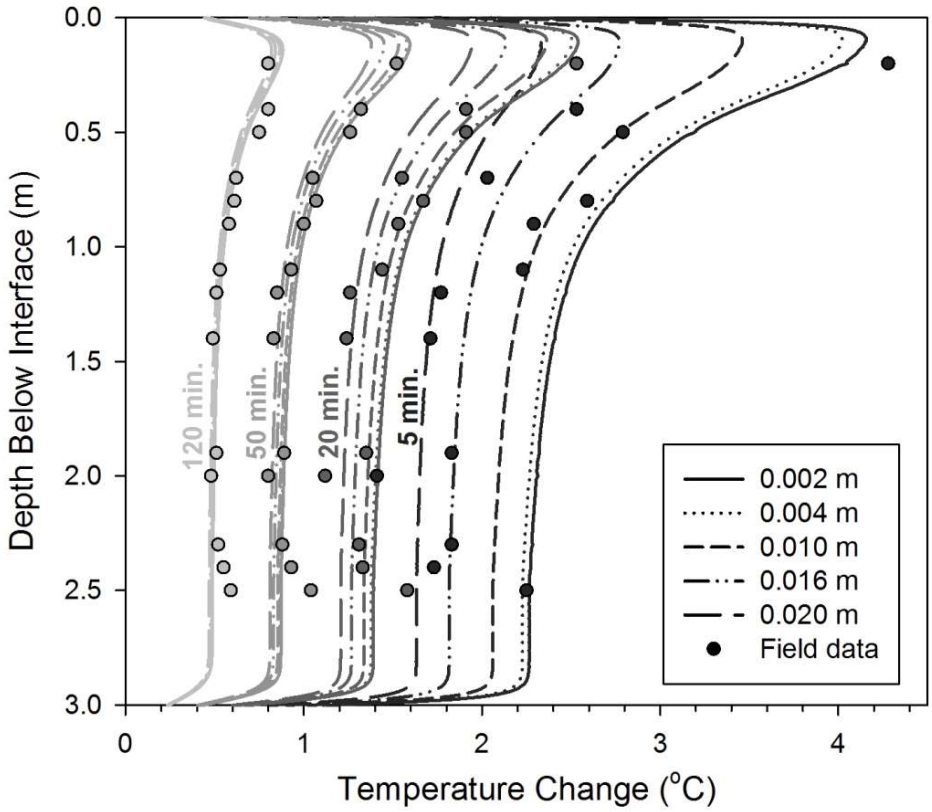

Figure 2-14. Measured temperature change with depth (circles) compared to simulated temperature change at multiple heating radii (lines), both at 5 (darkest), 20, 50, and 120 (lightest) minutes after cooling began.

The numerical model demonstrated that heating radius had minimal impact on the simulated results twenty minutes after cooling began, as long as the radius was within a smaller range (e.g., 0.002 to 0.010 m). Consequently, the model was calibrated to the field measurements from thermistors with a heating radius in this range (0.002 to 0.010 m), 20 minutes after cooling began. The thermal properties specified in the numerical model were incrementally changed, and the RMSE between the measured and simulated temperature change values was calculated to determine the thermal properties producing the optimal fit. The thermal property values were restricted so that they consistently changed with depth, as

predicted in the laboratory portion of this study (Figure 2-11). For example, the thermal conductivity only increased with depth, as opposed to decreasing and increasing to match the results from individual thermistors.

When the volumetric heat capacity was modified with depth, the calculated RMSE remained relatively consistent. Thus, volumetric heat capacity had a limited influence on temperature change during the cooling portion of the in-situ heat experiment, as indicated by the original simulation results (Figure 2-13). The volumetric heat capacity values with depth were left as the median values in the predicted volumetric heat capacity range (Figure 2-11).

Conversely, the simulated temperature change was sensitive to modification of the thermal conductivity values with depth. The thermal conductivity values producing the minimum RMSE (0.05 K) for all thermistors are plotted in Figure 2-15. The thermal conductivity trend with depth generated by calibrating the model to the field results generally followed the predicted trend established during the laboratory portion of this study (Figure 2-15). The thermal conductivity values increased rapidly within the top portion of FFT, and increased slightly or stayed fairly constant below this depth.

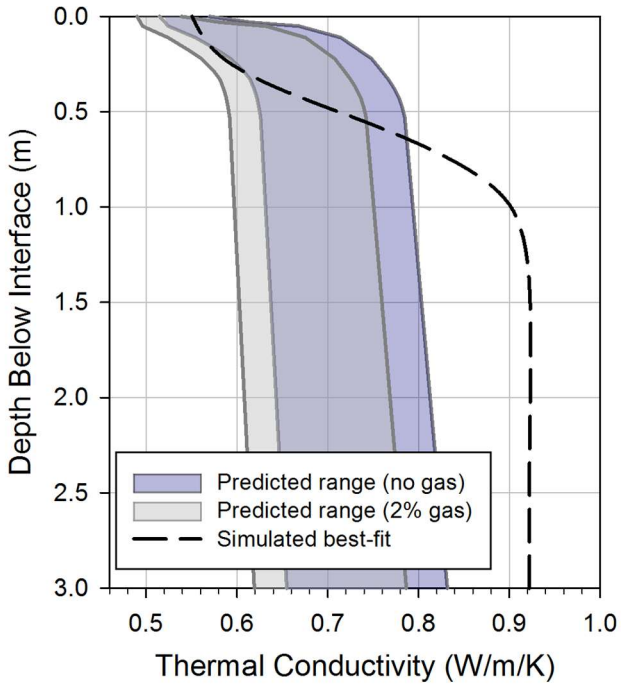

Figure 2-15. Predicted range of thermal conductivity values through the FFT from the laboratory experiment for no gas and with gas bubbles, compared to values determined by the in-situ experiment and corresponding numerical model.

2.4.3.4 Discussion of In-Situ Testing and Numerical Modelling Results

The numerical model was only calibrated for the cooling portion of the in-situ experiment due to discrepancies between the field measurements and the temperature change determined by both the analytical solution and numerical model at the end of heating. A number of possible explanations for the discrepancies were evaluated, including: (1) the influence of the supporting rope running alongside the heating wire and thermistor string on the 'radial' heat transfer from the heating wire; (2) the potential for free convection to have occurred during heating of the FFT; (3) the influence of vertical heat dissipation; (4) the potential for the properties of the heating wire to change as its temperature increased; and (5) shifting of the thermistors or heating wire during installation. The first four explanations were ruled out after thorough consideration, including the development of supplemental numerical models. In the end, the most likely explanation for the discrepancy between the measured and predicted peak temperatures was that the location of the thermistors had shifted during installation.

According to the heat pulse probe methods, the volumetric heat capacity of a soil cannot be determined without a well-defined heating radius (Bristow et al., 1994). However, thermal conductivity can be determined without a defined heating radius when the system reaches a quasi-steady state as described in ASTM D5334-14 (ASTM, 2014*c*). This quasi-steady state can occur during both the heating and cooling portions of the heat pulse experiment. This supports the findings in the previous section, as the FFT thermal conductivity was evaluated given the results from the cooling portion of the in-situ experiment after the quasi-steady state was reached, 20 minutes after cooling began.

The best-fit thermal conductivities exhibited a larger range than the values calculated during the laboratory portion of the study. The numerical model captured the rapid transition in thermal conductivity values within the top portion of FFT; however, the transition zone interpreted from the heating test was larger than the transition zone predicted with the laboratory results and solids content envelope from the field (Figure 2-15). The thermal conductivities determined by the best-fit numerical model were reasonable within the top 0.7 m of FFT. For example, the thermal conductivity simulated at the very top of the FFT profile corresponds to the thermal conductivity of water, or FFT with relatively high water

and bitumen contents. Below a depth of 0.7 m, the modelled thermal conductivities were higher than those estimated from the laboratory predictions (Figure 2-15). The laboratory analysis suggested that a thermal conductivity of 0.9 W/m/K is associated with a volumetric water content of less than 0.75. The characteristics of FFT measured in the field (Figure 2-3) suggest that the top 3 m of FFT in BML would likely have a higher volumetric water content.

The in-situ experiment was also developed to evaluate the influence of gas bubbles on the FFT thermal properties in Base Mine Lake. Thus, the effect of in-situ gas bubbles on the FFT thermal conductivity was considered by modifying the theoretical relationship in equation (2.3) to:

$$\lambda = \lambda_s^{[f_s]} \cdot \lambda_w^{[f_w]} \cdot \lambda_b^{[f_b]} \cdot \lambda_g^{[f_g]} \quad (2.6)$$

where λ_g represents the thermal conductivity of the gas bubbles (W/m/K), and f_g is the volumetric gas content (m^3/m^3). The relationship for the thermal conductivity of saturated soils (Cosenza et al., 2003) still applies, as these gas bubbles would not be continuous. The gas bubbles would act as inclusions within the FFT of a different thermal conductivity (similar to the presence of bitumen). The gas present in the FFT is most likely methane, so the thermal conductivity of the bubbles was assumed to be 0.035 W/m/K (Assael et al., 1990).

A gas volume fraction of 0.02 caused the predicted FFT thermal conductivity to decrease by approximately 5% (Figure 2-15). The modified thermal conductivity trend with depth matches the simulated thermal conductivity values within the top 0.3 m of FFT; however, the presence of gas does not provide an explanation for the high thermal conductivity values determined from the in-situ test below a depth of 0.7 m.

A final hypothesis for the unexpected thermal conductivities determined by the in-situ experiment was that the system installation disturbed the FFT. The yield stress within the top 0.5 m of FFT in BML is expected to increase rapidly with depth, by approximately 2 to 3 orders of magnitude (Dompierre and Barbour, 2016*a*). Below this depth, the yield stress is expected to continue to increase but more gradually. The rope adjacent to the heating wire could have provided a preferential pathway for water to escape the FFT. The increasing yield stress of the FFT with depth and the presence of a preferential pathway could have resulted in the densification of the FFT near the heating wire, particularly at greater depths. Densification

would cause elevated solids contents along the heating wire, increasing the thermal conductivity of the surrounding FFT.

The in-situ test results provide preliminary insight on the FFT thermal conductivity in BML; however, the testing system requires further development. Future designs must consider the potential for FFT disturbance via densification and movement of the thermistor string or heating wire during installation. For example, the rope should be replaced with a material that will not promote wicking and a small spacer with known thermal properties could be used to ensure the heating radius remains constant.

2.5 Conclusions

Laboratory testing demonstrated that the FFT thermal conductivity varied from 0.7 to 1.2 W/m/K when the volumetric water and bitumen contents ranged from 0.64 to 0.89 and 0.01 to 0.08, respectively. Given the same range in FFT composition, the measured volumetric heat capacities varied from 3.1 to 3.9 $x10^6$ $J/m^3/K$. Water content had a greater influence on the FFT thermal properties; however, bitumen content was also significant, particularly for thermal conductivity.

Laboratory testing also provided a well-defined relationship between the FFT composition and its thermal properties. The measured volumetric heat capacities matched those calculated by equation (2.4) when the specific heat capacity of the dry FFT solids was decreased to 700 J/kg/K to correspond to the results presented by Li et al. (2015). Equations (2.3) and (2.4) were used to determine the expected thermal conductivity and volumetric heat capacity ranges within the top region of FFT. Thermal conductivity was expected to vary between 0.52 and 0.83 W/m/K, and volumetric heat capacity was predicted to range from 3.36 to 4.18 $MJ/m^3/K$ within 3 m of the FFT-water interface. These relationships can also be employed to examine the effect of gas bubbles on the FFT thermal properties, as demonstrated in equation (2.6).

The in-situ experiment and associated numerical model produced initial estimates of thermal conductivity with depth through the FFT, and demonstrated that in-situ testing of thermal properties is possible in soft sediments or tailings. The thermal conductivities estimated from the in-situ test ranged from 0.56 to 0.92 W/m/K. These values increased with depth, as was expected based on the laboratory results. However, the thermal conductivities at greater depths were higher than the predicted values, possibly due to densification of the FFT.

Future field methods will need to minimize the FFT disturbance during installation of the testing system.

In-situ estimates of volumetric heat capacity were not possible in this study due to the inability to control the heating radii with depth during installation. In future testing, a spacer with known thermal properties should be installed between the heating wire and thermistor to insure the heating radii are constant with depth and over time. This spacer would also allow the thermistors to be placed at a greater distance from the heating wire (e.g., 0.05 m). Given this known heating radius, future in-situ tests could examine the effect of sample disturbance on the thermal properties of FFT and provide a better indication of the presence of bubbles.

The laboratory and in-situ test results provide useful information on the thermal properties of FFT. Bitumen was observed to have a substantial effect on both the thermal conductivity and volumetric heat capacity; however, water content remained the most significant factor influencing the FFT thermal properties. These findings are applicable to future studies assessing the movement of energy through FFT, and supply important information for determining the energy balance in the water cap of BML and other EPLs.

CHAPTER 3 – CHARACTERIZATION OF PHYISCAL MASS TRANSPORT THROUGH OIL SANDS FINE TAILINGS IN AN END PIT LAKE: A MULTI-TRACER STUDY (DOMPIERRE AND BARBOUR, 2016*a*)

This chapter summarizes the use of heat and stable isotopes of water to assess mass transport through the FFT in BML. A combination of methods was employed, including long term in-situ FFT temperature measurement, FFT field sampling, and laboratory analysis to determine the FFT pore water isotope signatures. Numerical models for heat transport through the FFT were established based on the long term temperature measurements and the thermal properties of the FFT. Numerical models for mass transport were developed with the isotope signatures of the FFT pore water. In addition to assessing the main mechanisms contributing to mass transport through the FFT, this study also provided insight on pore water flux rates associated with FFT settlement, energy movement through the FFT, and the potential for free convection and other forms of mixing to occur within the tailings.

I, Kathryn Dompierre, led the design and management of the field sampling program, provided oversight for the installation of the temperature measurement systems, processed and analyzed all isotope samples in the laboratory, developed the numerical models (described in detail in Appendix A), completed all data synthesis and analysis, and served as lead author of the manuscript. Morris Flynn (University of Alberta) led the experimentation program on the dynamic viscosity and yield stress of FFT from BML, Chris Surma (undergraduate summer student, University of Alberta) conducted the associated laboratory work and Barry Bara (Syncrude Canada Ltd.) assisted with data interpretation of the laboratory results. Geoff Halferdahl (Syncrude Canada Ltd.) coordinated laboratory testing on the other physical properties of the FFT at the Syncrude Canada Ltd. Edmonton Research Facility. I, Kathryn Dompierre (85%), carried out the majority of the contributions to the preparation of the manuscript with Lee Barbour (15%) assisting with the development of the numerical models and providing comments during the review process.

Permission to reprint this manuscript was granted by Elsevier under license number: 3943110164176. The full reference for the paper reproduced in this chapter is:
Dompierre, K.A., and Barbour, S.L. 2016. Characterization of physical mass transport through oil sands fluid fine tailings in an end pit lake: a multi-tracer study. *Journal of Contaminant Hydrology*, 189: 12 -26. DOI: 10.1016/j.jconhyd.2016.03.006.

3.1 Introduction

Soft tailings are a fluid-like by-product of the milling or extraction processes associated with mining. Conventional terrestrial reclamation of this mine waste requires stabilization of the soft tailings to increase their bearing capacity and shear strength before a soil cover is placed over the tailings. One alternative approach developed for the disposal of this material is to place the soft tailings within depleted mine pits and cover them with a water cap. Oil sands operators plan to employ this strategy as a means of reducing their inventory of soft tailings produced by the extraction of bitumen from oil sands ore, referred to as fluid fine tailings (FFT). Oil sands operators have proposed the development of thirty EPLs, half of which will incorporate unprocessed FFT below the lake water (Prakash et al., 2011).

The development of EPLs would allow oil sands operators to decrease the volumes of FFT stored in tailings impoundments; however, the feasibility of isolating FFT from the overlying water and establishing a sustainable biological community in the lake have yet to be fully evaluated. The FFT pore water generally contains high concentrations of dissolved constituents, naphthenic acids, petroleum hydrocarbons, and unrecovered bitumen (Allen, 2008; Dompierre et al., 2016; Kavanagh et al., 2011). These constituents may move from the FFT into the lake water via two key processes: (1) advective-diffusive mass transport with upward pore water flow caused by dewatering of the soft tailings; and (2) mixing created by wind events or unstable density profiles through the lake water and upper portion of the FFT. The long-term biogeochemical evolution of the FFT is being studied but is currently unknown; however, the mechanisms controlling the transport of heat and aqueous constituents will remain key foundational processes in the development of this understanding.

This study presents a preliminary assessment of the movement of the stable isotopes of water (deuterium, ^{2}H; oxygen-18, ^{18}O) from the FFT to the water cap of the first EPL developed in the Athabasca oil sands region. These isotopes serve as conservative tracers for potential

chemical transport since they are components of the water molecule. The concentrations of these isotopes are generally represented in terms of differences in the isotopic ratios (i.e. $^{2}H/^{1}H$ or $^{18}O/^{16}O$) from known standards, according to the 'del' notation (δ). The isotopic composition of a water sample can be used to identify its source (Coplen et al., 2000). This method has been applied in many different fields, including: (1) hydrology, to measure evaporation and precipitation trends (Gammons et al., 2006; Gibson et al., 1996), and to determine the water balance of catchments and lakes (Gibson et al., 2005; Gibson and Edwards, 2002); (2) hydrogeology, to track the movement of water through aquitards (Hendry and Wassenaar, 2011), and assess groundwater recharge rates and residence times (Buttle, 1998; McGuire, et al., 2005; Taylor and Howard, 1996); and (3) contaminant transport to determine advection and diffusion of conservative species (Barbour et al., 2012; McKay et al., 1993). Stable isotopes of water have more recently been employed in the oil sands to characterize the isotopic signatures of various natural and mine affected waters (Baer, 2014), to trace the movement of process-affected waters (Gibson et al., 2011), and to evaluate recent recharge into overburden deposits (Huang et al., 2015). Therefore, stable isotopes of water are an appropriate tracer to assess mass transport through the FFT in BML.

Heat was also used as a tracer for evaluating the mechanisms controlling the movement of conservative aqueous constituents in the FFT. Heat has been employed to trace the movement of groundwater (Anderson, 2005; Bredehoeft and Papadopulos, 1965; Saar, 2011; Stallman, 1965), and can be used to evaluate interactions between surface and groundwater systems (Blasch et al., 2007; Constantz, 2008; Stonestrom and Constantz, 2003; Suzuki, 1960). Heat transfer via convection is mainly driven by fluid flow; therefore, convective heat transfer can be used as a tracer for advective mass transport through the FFT. Convection may be either: (1) forced convection, in which the movement of heat is due to hydraulically driven water flow; or (2) free convection, in which fluid flow occurs as a result of temperature-derived density differences (Anderson, 2005; Pop and Ingham, 2001). In an EPL, forced convection would result from the upward movement of water associated with FFT densification. Free convection could occur within the FFT if substantial temperature-induced density differences form.

Heat transfer between the water cap and underlying FFT in an EPL may also occur as a result of conduction. Conduction is the transmission of heat from more energetic molecules to those with less energy (Rathore and Kapuno, 2011). The lake temperature changes seasonally

with air temperature, causing conduction to occur over the FFT-water interface. Conduction is generally more effective in moving heat than diffusion is in moving mass, so heat cannot be used as a direct tracer for diffusive mass transport. However, if convection is shown to be an important mechanism for heat transport through the FFT, then advection will be integral to mass transport.

Movement of the lake water itself may also play an important role in heat and mass transport through the FFT. Wind-induced waves or lake turnover may erode the FFT-water interface, as Adu-Wusu et al. (2001), Catalan and Yanful (2002), and Kachhwal et al. (2011) observed the erosion and resuspension of soft tailings stored under water caps. Thus, fluid movement in the lake could cause mixing within the tailings, which would create an additional form of fluid movement or advective mass transport. This mixing may only occur seasonally, for example, in the fall when the lake undergoes turnover, and would disturb the dominant form of mass transport occurring throughout the remainder of the year.

This study will provide valuable insight on the performance of EPLs as an oil sands reclamation strategy by characterizing the dominant mechanisms for heat and mass transport across the FFT-water interface. An understanding of these processes during the early stages of EPL development is essential for assessing the geochemical evolution of FFT, and the potential containment and isolation of FFT through the use of EPLs. When combined with biogeochemical analysis of the FFT pore water characteristics (e.g. Dompierre et al., 2016), findings from this study will assist in the development of monitoring and management plans for future EPLs.

3.2 Site Description

The first EPL was established at the Mildred Lake Mine approximately 35 km north of Fort McMurray, Alberta, Canada (Figure 3-1). The mine site is located in a sub-humid continental climate region with short summers and long cold winters (Carey, 2008). Minimum and maximum mean daily temperatures of -39.8 °C (January 18, 1996) and 26.3 °C (August 1, 2003), respectively, have been measured at the Mildred Lake weather station adjacent to the mine (Environment Canada, 2015). The mean annual temperature is 1.0 °C (Environment Canada, 2015).

Operations at the Mildred Lake Mine began in 1978 when Syncrude Canada Ltd. commenced surface mining of oil sands ore. The oil sands ore is from the McMurray Formation, and generally contains an average of 12 % (w/w) bitumen (long chain hydrocarbons), 3 to 6 %

(w/w) water, and 84 to 86 % (w/w) solids, comprised of quartz sand with a small clay fraction (Chalaturnyk et al., 2002). Bitumen is extracted from the ore by adding hot water to decrease the bitumen viscosity and caustic (NaOH) to disperse the clay particles (Caughill et al., 1993; Masliyah et al., 2004). The resulting bitumen froth is separated for upgrading and the remaining sand-clay slurry is pumped to tailings impoundments, for example the Mildred Lake Settling Basin, for storage. The current mine site and tailings impoundment locations are shown in Figure 3-2.

Figure 3-1. Location of the Mildred Lake Mine (star) and known oil sands deposits (in grey).

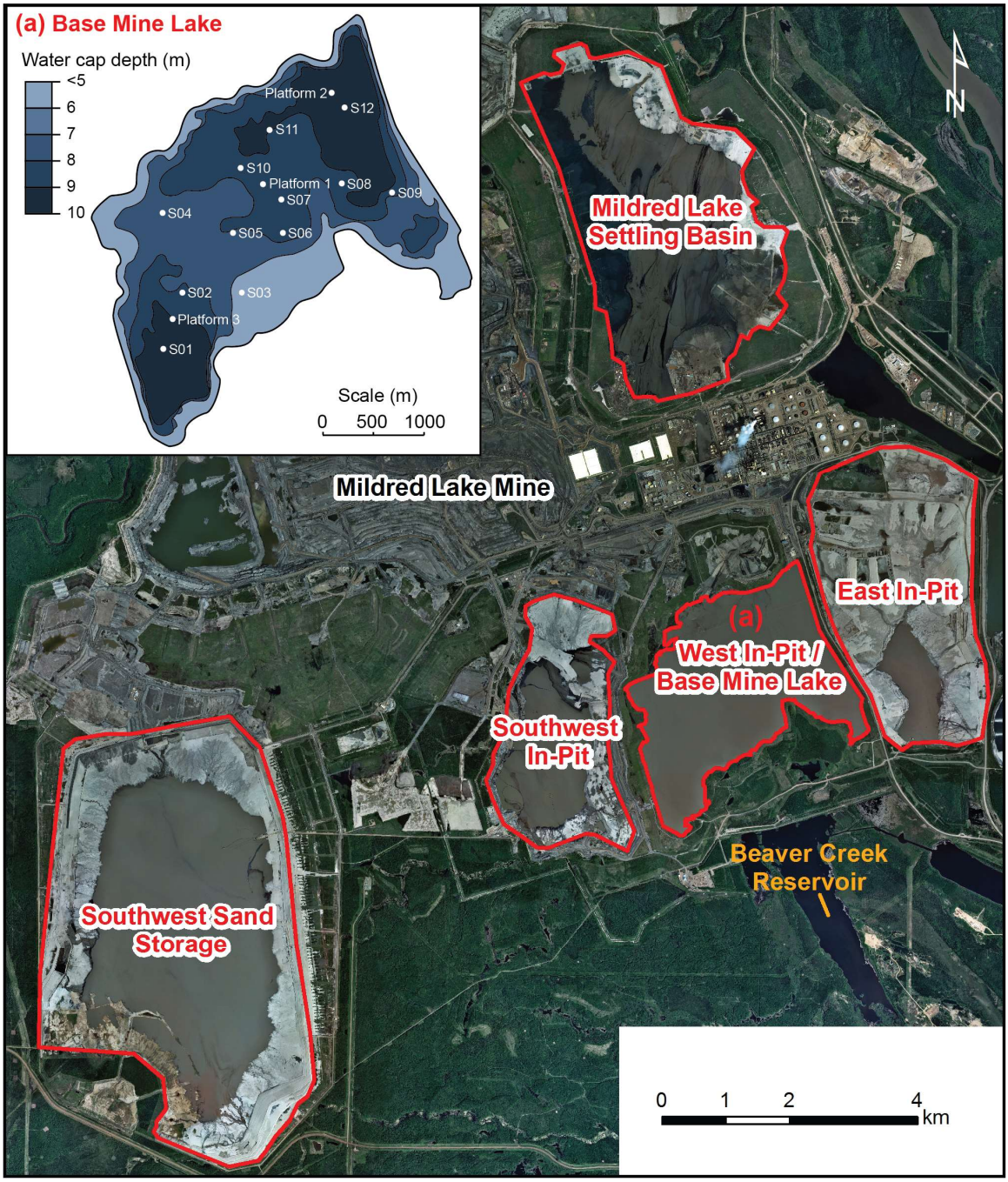

Figure 3-2. Satellite image of the Mildred Lake Mine with the tailings impoundments outlined in red; inset (a) shows a detailed image of the BML monitoring stations and water cap depth.

West In-Pit, a portion of the original mine pit, is one of the tailings impoundments at the Mildred Lake Mine site. The foundation of West In-Pit is generally composed of marine shales and siltstones of the Clearwater Formation. This formation is considered overburden material as

it overlies the oil sands ore. The mean vertical hydraulic conductivity for the Clearwater Formation is approximately 8 $x10^{-10}$ m/s (according to personal communications with Dallas Heisler, Syncrude Canada Ltd.). The base of West In-Pit also includes areas with lean oil sands material, which is oil sands ore with a bitumen content below 7 % (w/w). This material is a part of the McMurray Formation, which exhibits vertical hydraulic conductivities ranging from 1 $x10^{-13}$ to 1 $x10^{-7}$ m/s (Dallas Heisler, Syncrude Canada Ltd.). The Devonian Waterways Formation (the main Upper Devonian unit present at the mine site) lies below the overburden and lean oil sands forming the bottom of West In-Pit. This formation is composed of limestone and siltstones with a mean vertical hydraulic conductivity of 6 $x10^{-9}$ m/s (Dallas Heisler, Syncrude Canada Ltd.).

Syncrude Canada Ltd. began filling West In-Pit in 1994 with FFT dredged from the Mildred Lake Settling Basin. The FFT was pumped into the northeast corner of the pit from 1994 to 2012. The temperature of FFT during placement ranged from 11 °C to 19 °C. When filling was complete in 2012, the system was commissioned as an EPL called BML (shown in Figure 3-2). At this time, the maximum depth of FFT in BML was 45 m, corresponding to a total FFT volume of approximately 186 M m^3. The water cap depth during FFT placement was between 3 and 5 m. Since this time, fresh water has been pumped from Beaver Creek Reservoir into the lake with yearly volumes ranging from 6 to 7 M m^3. Water is removed from BML (for use in the bitumen extraction plant) to maintain a lake surface elevation of 308.7 ± 0.5 metres above sea level (masl). The average yearly volume of water pumped from BML is 6.5 M m^3. The corresponding average water cap depth is 8.5 m. The lake covers an area of approximately 8 km^2 and the estimated volume of the water cap is 65 M m^3. Freshwater input since BML was commissioned has resulted in the displacement of approximately 20 % of the standing lake volume to date.

The BML water cap responds to seasonal temperature cycles in a similar manner as natural temperate, northern lakes (e.g. Oswald and Rouse, 2004; personal communications with Edmund Tedford, University of British Columbia). During the summer months, the lake is strongly stratified from the end of May to the beginning of September. The water temperature of the upper portion of the lake increases during the month of June to 20 °C and stays at this temperature until September, while the lower portion of the lake gradually warms over this entire period (June to September) to 15 °C. In the fall, the lake exhibits turnover from the beginning of September until the ice forms in November. During this time the lake cools to 2 °C. Over the winter season, the

lake water is weakly stratified below the ice cover. Temperatures remain relatively constant throughout this period with water near the ice at 0 °C and a temperature of approximately 4 °C near the FFT-water interface. The ice generally melts by the end of April, which is followed by a weaker and more irregular spring turnover, as compared to the fall turnover.

The FFT below the water cap in BML is a dense, warm fluid suspension comprised of dispersed mineral particles and oil sands process-affected water. The bulk density of FFT in BML ranges from 1010 kg/m^3 near the surface of the deposit, to 1600 kg/m^3 near the base of the deposit with an average bulk density of 1360 kg/m^3 through the main body of the tailings. The FFT pore water (oil sands process-affected water) generally contains high concentrations of dissolved constituents (e.g. sodium, chloride, bicarbonate), naphthenic acids, petroleum hydrocarbons, and unrecovered bitumen (Allen, 2008; Dompierre et al., 2016; Kavanagh et al., 2011). The bitumen content of FFT in BML is typically between 1 and 6 % (w/w). The initial solids content of FFT is generally 25 to 35 % (w/w), and is predominantly made up of quartz and clay minerals including kaolinite, illite, chlorite, and illite-smectite (Dompierre et al., 2016; Osacky et al., 2013*b*). The hydraulic conductivity of the FFT is expected to range from 1 x10^{-7} to 5 x10^{-5} m/s based on the typical water content values (or void ratios) of FFT in BML and the laboratory results presented by Suthaker and Scott (1996). Seasonal temperature fluctuations may also affect the hydraulic conductivity of FFT; however, based on the typical water content values of FFT in BML, changes in void ratio with depth likely have a greater impact on the variability of hydraulic conductivity through the FFT (Chapuis, 2012).

Biogeochemical reactions observed in the FFT include fermentation, methanogenesis and sulfate reduction (Dompierre et al., 2016). These processes are typically exothermic and may generate heat within the FFT; however, acetoclastic methanogenesis is an endothermic reaction (Von Stockar et al., 2000) that may be occurring in the FFT in BML. Thus, the net impact of these microbial processes on the energy present within the FFT remains unknown. Conversely, FFT contained a substantial amount of energy at the time of deposition in BML as it was deposited at elevated temperatures. These temperatures were a result of the bitumen extraction process and the high specific heat capacity of the tailings (Dompierre et al., 2014). Therefore, the energy produced by microbial reactions is assumed to be negligible compared to the energy stored in the FFT at the time of deposition.

The FFT in BML exhibits slow rates of settlement due to the addition of dispersants (NaOH) during bitumen extraction, and naturally occurring surfactants (asphaltic acids) that are present in the ore and released during heating (Chalaturnyk et al., 2002; Jeeravipoolvarn, 2009). Primary dewatering of the FFT occurred during the first few years after deposition; however, high water contents are expected to persist for an extended time period (Kasperski and Mikula, 2011). The FFT in BML is currently undergoing hindered settlement or self-weight consolidation.

Self-weight consolidation occurs when the solid matrix does not support itself. This is typical of FFT at high water contents. Pore pressures developed during the deposition of FFT are equal to the total weight of the overlying fluid and solid suspension, and are consequently much higher than a hydrostatic pressure profile. This excess pressure results in an upward flow of water with the most rapid dissipation of pore pressure (and concomitant increase in effective stress) occurring at the base of the FFT. Thus, self-weight consolidation causes the bottom portion of the deposit to dewater first with the expressed water moving upward through the FFT column. Consequently, the pore water flow within the top portion of the FFT can be assumed to be constant with elevation as this region does not undergo significant dewatering during the early years of an EPL.

Pore water movement through the FFT is expected to obey Darcy's law as the water fluxes associated with tailings settlement produce Reynolds numbers substantially less than 1 ($<4 \times 10^{-7}$). A small portion of the expressed pore water may move downwards and into the formation underlying BML; however, leakage from the pit bottom is expected to be minor based on the relatively low hydraulic conductivity of the underlying formation. Pore water pressures measured in the field by Syncrude Canada Ltd. indicate that this downward flow is relatively small.

Carrier et al. (2007) developed a preliminary model for Syncrude Canada Ltd. to simulate the dewatering of FFT in BML. According to this model, FFT in BML would exhibit settlement rates of approximately 1 m/year after deposition, and these rates would decrease exponentially over 30 years. After a 30-year period, the predicted pore water release levelled out to approximately 0.1 m/year (Carrier et al., 2007).

3.3 Methodology

Base Mine Lake is the focus of a comprehensive research program to evaluate the controls on the long-term physical, hydrologic and biological evolution of the lake. A field investigation was conducted at BML in 2013 and 2014 to measure the in-situ temperatures through the FFT, as well as the isotopic signatures with depth across the FFT-water interface. Numerical models were developed to represent various forms of heat transport (conduction, free convection and forced convection), and physical mass transfer (diffusion, advection and dispersion). Model results were compared to field data to assess the mechanisms driving physical mass transport of conservative species through the FFT in BML at multiple locations. The findings were compared to an independent assessment of FFT settlement conducted by Syncrude Canada Ltd. at BML to verify the results.

3.3.1 Preliminary Investigation of FFT Properties

ConeTec Investigations Ltd. collected FFT samples at 6 locations (Platform 1, Platform 2, Platform 3, S04, S08 and S09; see Figure 3-2 for sample locations) using a pneumatic piston sampling system during the 2014 FFT monitoring program. A sample chamber with a pneumatic piston was positioned at the desired depth, the cable-actuated ball-valve on the chamber was opened, and the pneumatic piston was slowly retracted to allow FFT to enter the chamber. The ball valve was closed when the chamber was full, the sample system was brought up to the surface, and the collected sample was transferred to a high-density polyethylene bottle (HDPE). The samples were collected throughout the entire depth of FFT in BML, at 1 m to 3 m intervals.

ConeTec Investigations Ltd. also conducted Fixed Interval Fluid Sampling^{TM} to passively obtain closely spaced fluid samples over the FFT-water interface at the same 6 locations (Platform 1, Platform 2, Platform 3, S04, S08 and S09). This method involved a sample frame with 10 or 20 sample cylinders fixed at 0.1 m intervals. The sample cylinders each had an internal piston and were attached to a compressed gas source. The compressed gas was used to hold the piston at the opening of the sample chamber while the sample frame was slowly lowered to the desired depth range. Once the sampler reached this depth, the gas pressure was released. The piston was then pushed backward by the hydrostatic pressure of the fluid surrounding the sample cylinder, allowing FFT to enter the chamber. The sampler was brought up to the surface, and HDPE bottles were attached to each sample cylinder. The FFT was extruded into the bottles by re-applying the gas pressure and moving the piston back to its original position.

Both sets of samples were sent to the Syncrude Canada Ltd. research facility in Edmonton for laboratory analysis. The solids and water contents of each sample were determined using the Dean and Stark extraction method (Dean and Stark, 1920). The particle size distribution of the dry FFT solids from each sample was determined with a Coulter LS 13 320 laser diffraction particle analyzer (after ASTM, 2015*b*; ASTM, 2014*a*). Additional laboratory testing on select FFT samples was conducted to determine the dynamic viscosity and Bingham yield stress of low solids content FFT (Flynn et al., 2015) using a R/S Plus Brookfield Rheometer, and methods outlined by Steffe (1996).

3.3.2 Isotope Sampling

Sampling of BML water and surrounding water sources was conducted by Golder Associates between May 2013 and October 2014 to catalogue the stable isotopes of water. These samples were collected in 500 mL HDPE bottles at the lake inflow and outflow, and at several stations around the lake (Platform 1, Platform 2, Platform 3, S06, S07, S08, S09 and S10). Isotope sampling over the FFT-water interface was also conducted in July 2014. Samples of FFT and lake water were collected with the Fixed Interval Fluid Sampling™ method (ConeTec Investigations, Ltd.) at three of the monitoring locations (Platform 1, Platform 3, and S04). The sample frame was used to collect samples within the top 1.5 m of FFT and bottom 1.5 m of lake water. These samples were collected in 250 mL HDPE bottles, and were transported in coolers to minimize temperature fluctuations.

3.3.3 In-situ Temperature Measurements

A permanent temperature-measurement station was installed at BML in September 2013 at Platform 3 (location provided in Figure 3-2). The station consisted of 30 thermistors (±0.1°C) attached to a Kevlar cable at 1 to 2 m intervals, as illustrated in Figure 3-3. The Kevlar cable was fixed to the bottom of the FFT with a naval anchor, and the top was attached to a buoy to create tension in the cable. A data logger was placed on the platform and connected to the thermistors through a PVC conduit to minimize ice impact. Temperatures were measured once a day, from September 2013 to March 2014, to observe seasonal temperature variations (rather than diurnal fluctuations) through the FFT and lake water. Crews checked on the data logger twice during the winter months to ensure that the system was functioning.

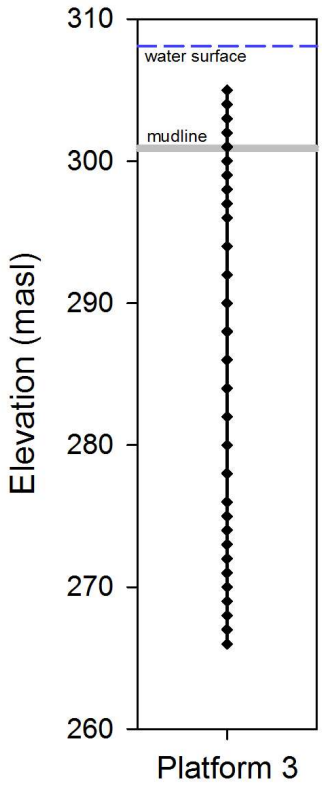

Figure 3-3. Thermistor positions with depth.

Another thermistor string was installed at Platform 3 in September and October 2014. This high-resolution thermistor string measured temperatures every 0.1 m through the top 2 m of FFT in BML. These temperatures were used to calculate the Rayleigh number for saturated porous media (Bear, 1972; Bennacer and Lakhal, 2005; Nield, 1968) at multiple intervals through the FFT, to assess the ability for free convection (density-derived fluid flow) to occur in the FFT pore water. In addition, a revised Rayleigh number (after Diersch and Kolditz, 2002) was used to assess free convection potential of the entire tailings matrix (solids and water), as the FFT in BML exhibits fluid-like characteristics. The revised Raleigh number used the dynamic viscosity of FFT (measured in the laboratory), and the density difference between vertical intervals to dictate mixing potential. The density of the FFT at a specific depth was based on: (1) the solids content measured during the preliminary FFT properties investigation; and (2) the density of the pore water, calculated with the temperatures recorded by the high-resolution thermistor string according to the methods described by McCutcheon et al. (1993). Thus, the density term

incorporated both solids content and temperature of the FFT at depth. The density term in the revised Rayleigh number equation would yield a negative value if density increased with depth.

3.3.4 Laboratory Analysis

All samples from the Fixed Interval Fluid Sampling^{TM} that contained FFT were centrifuged immediately upon arrival at the laboratory. Extracted pore waters were stored in 15 mL HDPE bottles with zero headspace until isotopic analysis was performed. The samples collected above the FFT-water interface (lake water) were not processed before isotopic analysis was conducted.

Isotopic analysis involved placing 10 mL of each water sample (either the extracted FFT pore water or unprocessed lake water) in a double-sealed Ziploc© freezer bag, filling the bag with dry air, and allowing the sample and the air to reach equilibrium (approximately 1 hour as recommended by Wassenaar et al., 2008). Water vapour from the sample bag was then inserted into a Picarro L-2120-i Cavity Ring Down Spectrometer to determine its stable isotopes of water signatures (for deuterium, δ^2H, and oxygen-18, $\delta^{18}O$). The vapour equilibration technique used by Wassenaar et al. (2008) was employed to obtain the corresponding δ^2H and $\delta^{18}O$ signatures of the liquid water. Duplicate samples were run for 20% of the lake and pore water samples to check the accuracy of this method.

3.3.5 Isotope Transport Model Development

One-dimensional mass transport models for advective-dispersive and diffusive transport were developed using commercial finite element simulation software for ground water flow and transport (CTRAN/W, GEO-SLOPE International Ltd., 2012; SEEP/W, GEO-SLOPE International Ltd., 2013). The model domain was a 5 m column of FFT, divided into 5 discrete layers (of 1 m depth). The model domain was limited to the top portion of the FFT, as this is the region where the isotopic composition of the FFT was observed to transition from typical FFT signatures (determined by Baer, 2014) to lake water conditions.

The volumetric water content of each layer was selected based on the solids content measured at Platform 3 during the preliminary investigation of FFT properties in BML. Volumetric water content, which is equivalent to porosity under saturated conditions, was used to calculate the changing void ratio of FFT with depth. Existing relationships between hydraulic conductivity and void ratio (Suthaker and Scott, 1996) were then used to estimate changes in hydraulic conductivity with depth. The coefficient of molecular diffusion within each layer was

specified based on the relationships between porosity and the coefficient of molecular diffusion established by Boudreau (1996), and measured diffusion values for water molecules containing δ^2H and $\delta^{18}O$ (Easteal et al., 1984; Mills, 1973). The diffusion coefficient values for each layer are provided in Table 3-1.

The initial concentration applied to the FFT pore water was the average stable isotopes of water signature measured through the FFT by the Fixed Interval Sampler (–12.4 ‰ for $\delta^{18}O$; –112.2 ‰ for δ^2H). This value was also used as the lower boundary condition as FFT pore water below the modelled domain was assumed to have a similar isotopic signature. The upper boundary condition was established using an 8.5 m column of water to represent the lake. An isotopic signature was applied to the top of the water column based on the isotopic signatures of water collected from BML (–13.8 ‰ for $\delta^{18}O$; –118.0 ‰ for δ^2H). The diffusion coefficient of the water column was altered to create two different upper boundary conditions on the FFT profile: (1) a fully mixed water column generated by assigning a large diffusion coefficient to the lake; or (2) a water column with no mixing other than by diffusion. This was to represent the full range of possible conditions occurring in the lake water as BML has been observed to be stratified for portions of the year and fully-mixed during other times.

Table 3-1. Properties of each model layer.

Layer	Water Content (% vol.)	Diffusion Coefficient (m^2/s)	Thermal Conductivity (W/m/K)	Volumetric Heat Capacity ($MJ/m^3/K$)
1	86%	8.6×10^{-10}	0.75	3.74
2	85%	8.2×10^{-10}	0.77	3.70
3	84%	7.9×10^{-10}	0.78	3.67
4	83%	7.7×10^{-10}	0.79	3.65
5	82%	7.4×10^{-10}	0.80	3.63

Diffusion-only mass transport was simulated for a one-year period. Advection was then added to the model by applying a specified upward water flux at the base of the model. Dewatering rates of FFT in BML were determined in 2013 and 2014 by tracking the elevation of

the FFT-water interface over time (completed by ConeTec Investigations Ltd.), and are associated with an approximate pore water flux of 0.003 $m^3/d/m^2$. Thus, the upward water fluxes applied to the advection models were chosen to range from 0.002 to 0.01 $m^3/d/m^2$.

Longitudinal dispersivity was included in the models and was assumed to be $1/100^{th}$ of the plume length (Van Der Kamp et al., 1994; Gelhar et al., 1992). The plume length in this study was selected based on the observed depth over which the isotope signatures in the FFT transitioned from typical FFT pore water values to lake water signatures (0.4 m). The linear pore water velocities, calculated by dividing the water flux applied to each model by the volumetric water content of the top FFT layer (porosity), were found to range from 0 to 1.4 $x10^{-7}$ m/s. The assumed dispersivity value and the calculated pore water velocities produced a range in values for the coefficient of mechanical dispersion, from 0 to 4.6 $x10^{-10}$ m^2/s.

An event was added to the model to simulate full mixing of the top portion of the FFT with lake water, as erosion and resuspension of soft tailings has been observed in other water-capped storage facilities (Adu-Wusu et al., 2001; Catalan and Yanful, 2002; Kachhwal et al., 2011). Two mixing depths, 0.5 m and 1 m, were imposed on the FFT column by changing the isotope signature of the FFT pore water in the mixed zone to the signature of the lake at the time of the mixing event. The date of the mixing event was set to October 15, 2013, as evidence of mixing in the top 1 m of FFT was observed during water quality monitoring in mid-October at BML. A Seabird 19plus sensor descended through the water column 1 m more than it had the day before, suggesting that the FFT-water interface at the same location changed over a very short period. This observation correlated with an increase in turbidity in the lake water.

3.3.6 Heat Transport Model Development

A commercial finite element code for heat transport (TEMP/W, GEO-SLOPE International Ltd., 2014) was used to simulate conduction and forced convection through the FFT. The model involved a simplified vertical profile to represent the top 5 m of FFT in BML. The same model domain as described for isotope transport, was used for heat transfer. A distinct water content, thermal conductivity, and volumetric heat capacity were assigned to the 5 discrete layers of the domain. The volumetric water contents assigned to each layer were the same as in the isotope transport model. The thermal conductivity and volumetric heat capacity of each layer were assigned based on relationships developed by Dompierre et al. (2014) for the thermal properties and volumetric water content. The assigned values are provided in Table 3-1.

Temperatures measured at the FFT-water interface from September 2013 to March 2014 at Platform 3 were applied as the upper thermal boundary condition for the top of the heat transport models. The average FFT profile temperature (10 °C) was used as the constant boundary condition at the bottom of the model domain. The temperature profile measured at Platform 3 on the first day of in-situ temperature readings (September 15, 2013) was used for the initial FFT temperatures in the model.

Once the profile and boundary conditions were established, a conduction-only thermal regime was modelled for 170 days, corresponding to the time period that field measurements were collected. Forced convection was then added to the model. The upward water fluxes applied to the forced convection models were similar to those used in the advective mass transport models, ranging from 0.002 to 0.01 $m^3/d/m^2$. Finally, 0.5 m and 1 m mixing events were added to the heat transport models to determine the effects of FFT mixing on the temperature profiles. The mixing events were incorporated into the models by changing the FFT temperature in the mixed zone to the temperature of the lake on October 15, 2013.

3.4 Results

3.4.1 Preliminary FFT Properties Investigation

The solids content of FFT in BML generally increases with depth (Figure 3-4). Pore water pressure in the FFT increases with depth due to the self-weight of the tailings. With restricted deep drainage, the FFT dewaters and densifies from the bottom first, pushing pore water upward through the FFT profile, and creating higher solids contents near the bottom of the profile, as observed in BML (Figure 3-4). The variability in measured solids content between locations is likely due to the different deposition times of FFT in each location as those closer to the FFT discharge point have had greater time for dewatering to occur and would exhibit higher solids contents with depth.

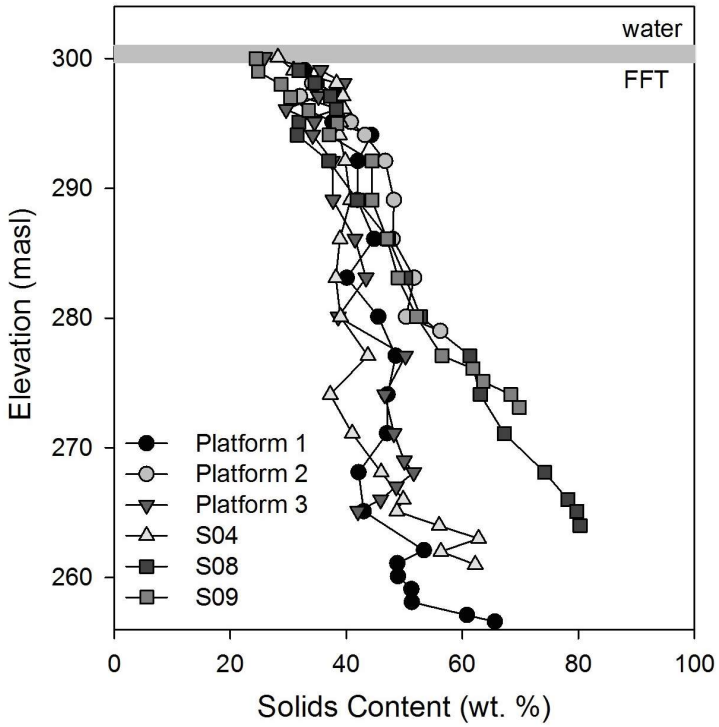

Figure 3-4. 2014 Solids content with depth.

The particle size distributions of the FFT at all of the sample locations and depths were relatively similar (Figure 3-5). At least 95 % (w/w) of the FFT solids are less than 75 µm in diameter (silt-sized particles) and 30 % (w/w) are less than 2 µm in diameter (clay-sized). Thus, the FFT solids are generally made up of 65 % (w/w) silts, 30 % (w/w) clays and less than 5 % (w/w) are fine sands. There were no consistent trends in the particle size distribution with depth through the FFT. Thus, the void ratio or water content with depth likely has a greater effect on the hydraulic properties of FFT in BML (Suthaker and Scott, 1996).

High-resolution solids content measurements near the FFT-water interface are provided in Figure 3-6, with a solids content envelope representing the minimum and maximum solids contents observed with depth. An estimated range for dynamic viscosities of the FFT near the FFT-water interface is also shown in Figure 3-6. These estimates are based on: (1) the solids content envelope; (2) the empirical relationship between water content and dynamic viscosity developed by Locat and Demers (1988) for sensitive clays; and (3) laboratory measurements of the dynamic viscosities of FFT at low solids contents (Flynn et al., 2015). The predicted range for

the dynamic viscosity of FFT near the FFT-water interface is relatively low, with values between 1 to 18 times the viscosity of water.

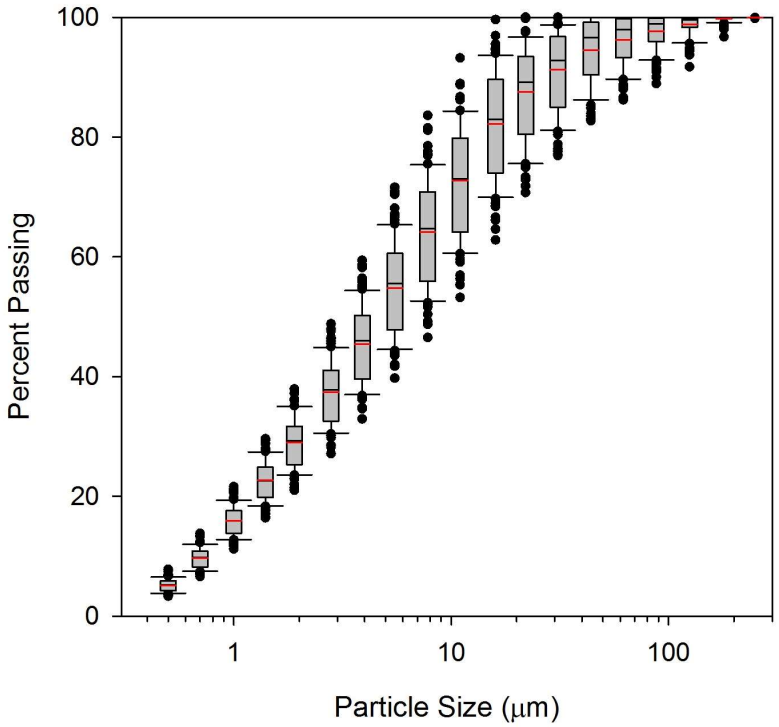

Figure 3-5. Particle size distribution of 85 FFT samples from BML as box plots of the interquartile range (25 to 75 percentile), median values (black lines), mean values (red lines), 10 and 90 percentile values (whisker caps) and outliers (circles).

The measured values for Bingham yield stress (Flynn et al., 2015), and a predicted range of yield stresses based on the solids content envelope, and work by McAnally et al. (2007) on fluid muds, are displayed in Figure 3-6. Fluid muds are fine-grained sediments found at the bottom of lakes or estuaries, with densities similar to FFT near the FFT-water interface (less than 1200 kg/m^3), and a similar mean particle size and clay fraction (McAnally et al., 2007). Within the top 0.2 m of FFT in BML, the yield stress is likely quite low as the measured yield stress values were less than 1 Pa. The low viscosities and yield stresses within the top portion of FFT provide little resistance to shear forces at the FFT-water interface, which might develop as a result of lateral water movement.

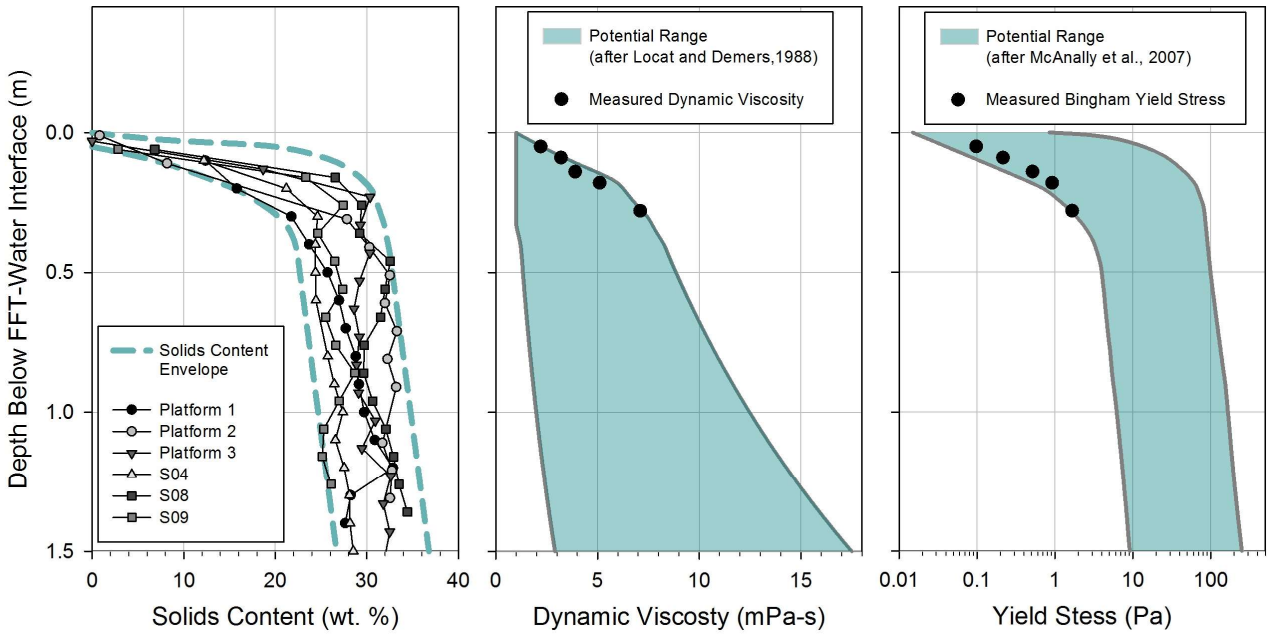

Figure 3-6. Measured and assumed solids content, dynamic viscosity and yield stress values near the FFT-water interface.

3.4.2 Stable Isotopes of Water Profiles

The stable isotopes of water profiles obtained by the Fixed Interval Fluid Sampling™ are illustrated in Figure 3-7 and Figure 3-8. The three locations had relatively similar isotopic signatures through the FFT pore water. The average value of δ^2H within the FFT at all locations was –112.84 ‰, with a standard deviation of 1.24 ‰. The average $\delta^{18}O$ value in the FFT was –12.66 ‰, with a standard deviation of 0.29 ‰. The FFT pore water signatures were more enriched than the lake water signatures, corresponding to findings summarized by Baer (2014) suggesting that FFT pore water has enriched signatures due to the bitumen extraction process and evaporation from tailings ponds.

Isotopic signatures in the lake water exhibited greater variability and shifted depending on the sample location. Platform 3 and S04 had slightly lower δ^2H and $\delta^{18}O$ values than Platform 1, likely due to a greater influence of fresh water at these locations. Fresh water is pumped into BML from the southwest corner, and runoff also enters the lake around the perimeter. Platform 3 is nearest to the pump-in location, and S04 is closest to the edge of the lake (as shown in Figure 3-2). A summary of the average lake water signatures at each sample location is provided in

Table 3-2. The average error calculated with the duplicate samples was 1.8 ‰ for δ^2H and 0.3 ‰ for $\delta^{18}O$.

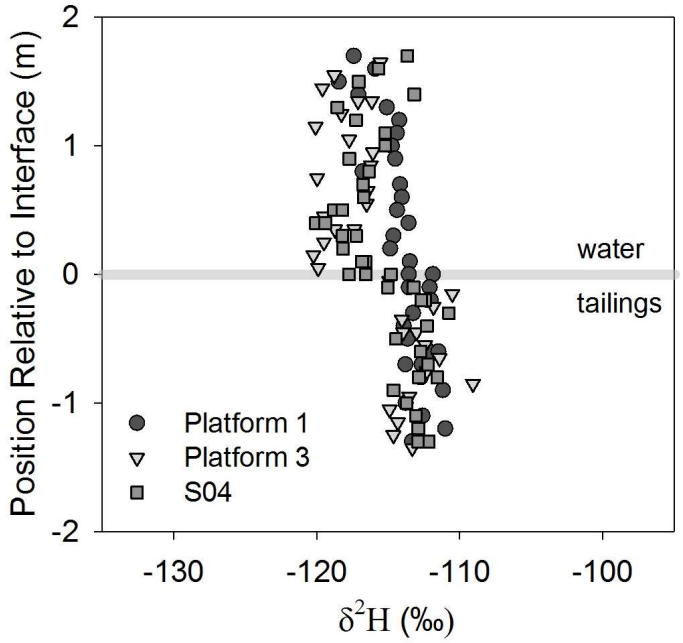

Figure 3-7. δ^2H measured over the FFT-water interface.

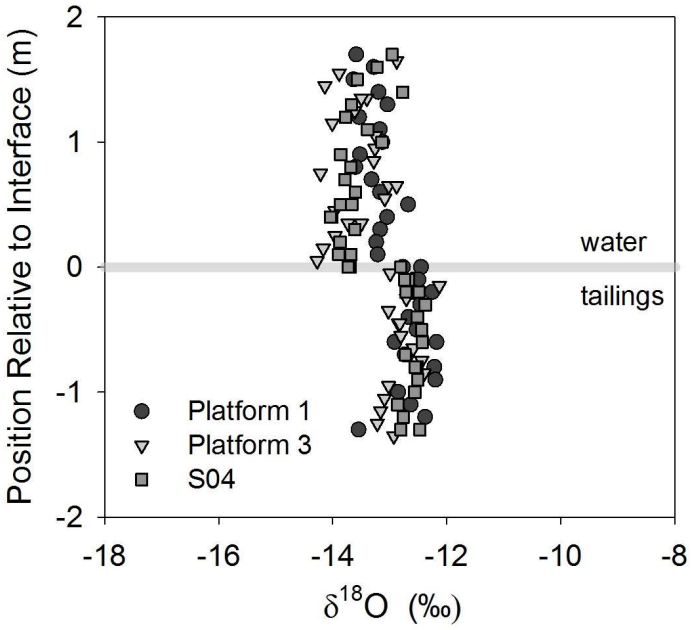

Figure 3-8. $\delta^{18}O$ measured over the FFT-water interface.

Table 3-2. Summary of lake water isotope signatures.

Location	δ^2H (‰)		$\delta^{18}O$ (‰)	
	Average	Standard Deviation	Average	Standard Deviation
Platform 1	-114.9	1.6	-13.2	0.3
Platform 3	-118.0	1.6	-13.6	0.4
S04	-117.0	1.7	-13.6	0.3

3.4.3 In-situ Temperature Measurements

Temperature readings from September 2013 to March 2014 were compiled to examine trends through the FFT (Figure 3-9). The top 5 m of FFT is affected by seasonal temperature variations in the lake water, which was measured to range from 0 °C to 18 °C. When compared to the average annual air temperature at the mine site (1.0 °C), the lake water appears to be warm; however, the measured temperatures are consistent with the general thermal regime observed in the water cap (as previously described).

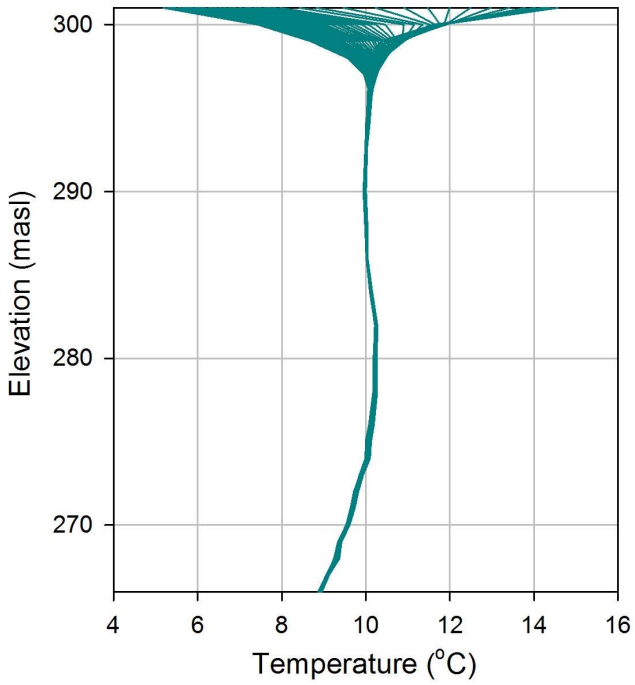

Figure 3-9. Platform 3 in-situ FFT temperatures.

Changing lake water conditions create a cyclic oscillation of the FFT temperatures, referred to as the temperature envelope. Over the observed range in temperatures (5 to 15 °C), the hydraulic conductivity of the FFT could vary by a factor of 1.5 near the FFT-water interface (Chapuis, 2012). Temperatures in the FFT below this zone were consistent throughout the measurement period. The FFT generally has a temperature of 10 °C with a small increase between 275 and 285 masl. Temperatures through the bottom portion of the FFT decline with depth, and suggest heat loss to the underlying formation.

High-resolution temperatures measured within the top 2 m of FFT showed that during the fall months when the lake cools, the FFT 1 m below the FFT-water interface is warmer than the overlying tailings. Temperature profiles exhibiting this trend were used to calculate the Rayleigh number at various depths to determine the potential for free convection of the FFT pore water. The Rayleigh numbers were found to be less than 1, which is substantially less than the critical Rayleigh number (40) determined experimentally by Elder (1967) for a homogeneous, isotropic medium. Thus, free convection of the FFT pore water is not likely.

The revised Rayleigh number was also calculated at various depths using the solids content envelope and dynamic viscosities illustrated in Figure 3-6. The resulting values were all found to be less than zero, as the density of the FFT (based on both temperature and solids content) increased with depth. Therefore, the potential buoyancy of warm FFT 1 m below the FFT-water interface was not significant enough to overcome the increasing solids content with depth, so the soft tailings in BML will not be implicated in free convection.

3.4.4 Isotope Transport Model

The results from the mass transport models for $\delta^{18}O$ are illustrated in Figure 3-10, with the field results from S04. The mass transport models with the fully mixed top boundary condition produced a greater shift in the isotopic signatures of the FFT, as mixing in the lake helped to carry mass away from the FFT-water interface. Diffusive mass transport through the FFT produced the greatest shift, and affected isotope signatures 0.5 m below the interface, while all of the advective mass transport models produced a disturbance of less than 0.1 m in the isotope profile.

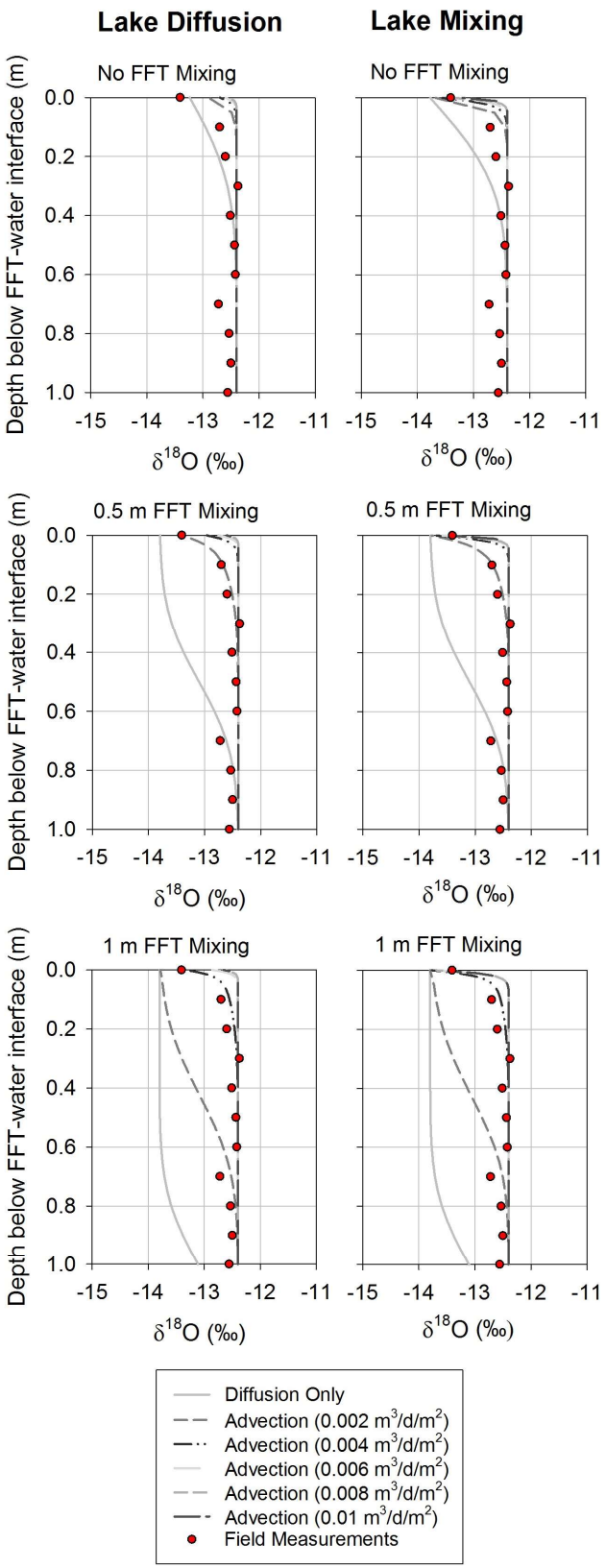

Figure 3-10. Isotope model results for two boundary conditions: lake diffusion and mixing.

The profiles produced by the non-mixing lake model for diffusion-only produced the largest shift in isotope signatures, extending to a depth of 0.4 m below the FFT-water interface. The advective mass transport models with a non-mixing boundary condition produced only a small shift in the $\delta^{18}O$ profile near the FFT-water interface, especially those with an upward water flux greater than 0.004 $m^3/d/m^2$. The isotope profile from the non-mixing lake model for diffusion provided the best fit for the field data based on the root mean square error (RMSE); however, neither the lake mixing nor lake diffusion model generated isotope profiles adequately matching the measured trend in isotope signatures at S04. The calculated RMSE values for each modelled scenario are provided in Table 3-3.

When a 0.5 m mixing event was added to the models, the isotope profile from the diffusive mass transport models (both upper boundary conditions) shifted substantially. A 0.5 m FFT mixing event also caused the isotope profile from the 0.002 $m^3/d/m^2$ advective transport models to shift so that 0.2 m of the FFT pore water exhibited disturbed isotope signatures, as opposed to only 0.1 m from the original models. The advective transport model for 0.002 $m^3/d/m^2$ produced an isotope profile aligning with the measured isotope values, particularly for the model with the lake diffusion upper boundary condition (RMSE of 0.06 ‰).

The simulated isotope profiles for advective mass transport with an upward water flux of 0.004 to 0.01 $m^3/d/m^2$ did not exhibit a substantial change when the 0.5 m FFT mixing event was added to the models. The advective mass transport profiles demonstrate that even a small upward flux (e.g. 0.002 $m^3/d/m^2$) will re-establish the observed isotope profile by the summer months, if a 0.5 m FFT mixing event occurs in the fall.

The isotope profiles created by the mass transport models with a 1 m FFT mixing event appeared to be quite similar, regardless of the upper boundary condition. Therefore, the greater the FFT mixing depth, the less dependent the isotope profile is on the upper boundary condition. The diffusion models both shifted substantially with a 1 m FFT mixing event, as did the 0.002 $m^3/d/m^2$ advective mass transport models. A greater upward flux (e.g 0.004 $m^3/d/m^2$) was required to re-establish the isotope profile by the summer months given 1 m of FFT mixing in the fall.

The best fit for the field data given 1 m of FFT mixing was advective mass transport with 0.004 $m^3/d/m^2$ of upward flux (RMSE of 0.10 ‰). The model was run with slightly lower flow values until the simulated isotope profile matched the field data. The simulation providing the best

fit (RMSE of 0.05 ‰) when a 1 m mixing event occurred in the FFT was advective mass transport with an upward water flux of 0.0036 $m^3/d/m^2$ (Figure 3-11). Therefore, the mass transport models demonstrate that a mixing event in the FFT likely produced the isotope profiles measured in the field. Based on the simulation results, a FFT mixing depth between 0.5 m and 0.1 m corresponds to an advective mass transport regime of 0.002 to 0.0036 $m^3/d/m^2$ in the FFT.

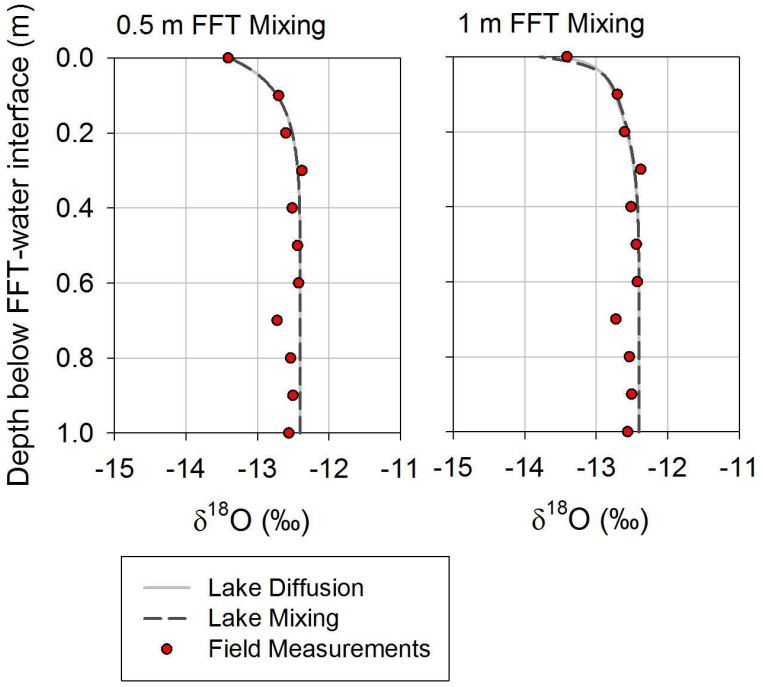

Figure 3-11. Advective mass transport models providing the best fit for 0.5 m FFT mixing event model (0.002 $m^3/d/m^2$) and 1 m FFT mixing event model (0.0036 $m^3/d/m^2$).

The simulated δ^2H profiles and trends were similar to the $\delta^{18}O$ results discussed above. The mass transport models providing the best fit to the measured δ^2H signatures were the same for each modelled scenario. The lowest RMSE values were produced by: (1) diffusive mass transport for the model with no mixing of the FFT (RMSE of 0.49 ‰); (2) advective mass transport with an upward flux of 0.002 $m^3/d/m^2$ for the simulation involving 0.5 m of FFT mixing (RMSE of 0.37 to 0.39 ‰, depending on the top boundary condition); and (3) advective mass transport with an upward flux of 0.004 $m^3/d/m^2$ when 1 m of FFT mixing was incorporated into the model (RMSE of 0.57 to 0.59 ‰). The RMSE values for the δ^2H results were higher than those

produced by the $\delta^{18}O$ results due to the greater variability in the measured $\delta^{2}H$ signatures with depth (Figure 3-7).

Table 3-3. RMSE values for each modelled scenario, for both upper boundary conditions (lake diffusion and lake mixing) compared to field isotope profiles (‰).

Advective	**No FFT Mixing**				**0.5 m FFT Mixing**				**1 m FFT Mixing**			
Flux	Diffusion		Mixing		Diffusion		Mixing		Diffusion		Mixing	
($m^3/d/m^2$)	$\delta^{18}O$	$\delta^{2}H$	$\delta^{18}O$	$\delta^{2}H$	$\delta^{18}O$	$\delta^{2}H$	$\delta^{18}O$	$\delta^{2}H$	$\delta^{18}O$	$\delta^{2}H$	$\delta^{18}O$	$\delta^{2}H$
0	**0.14**	**0.49**	0.31	1.11	0.72	3.10	0.72	3.10	1.15	4.50	1.15	4.50
0.002	0.15	0.80	**0.14**	**0.76**	**0.06**	**0.39**	**0.06**	**0.37**	0.79	2.68	0.77	2.62
0.004	0.16	0.83	0.15	0.82	0.15	0.82	0.15	0.82	**0.10**	**0.57**	**0.10**	**0.59**
0.006	0.16	0.83	0.16	0.83	0.16	0.83	0.16	0.83	0.16	0.83	0.16	0.83
0.008	0.16	0.83	0.16	0.83	0.16	0.83	0.16	0.83	0.16	0.83	0.16	0.83
0.010	0.16	0.83	0.16	0.83	0.16	0.83	0.16	0.83	0.16	0.83	0.16	0.83

3.4.5 Heat Transport Model Results

The minimum and maximum temperatures simulated by the conduction and forced convection heat transport models are illustrated in Figure 3-12. The conduction model produced the broadest temperature envelope with a larger depth of FFT undergoing seasonal cycles in response to temperature changes in the lake water. The temperature envelope narrows as the upward water flux increases. When greater pore water fluxes were applied to the modelled domain (>0.01 $m^3/d/m^2$), the temperature envelope was significantly narrower than those illustrated in Figure 3-12. The simulation results illustrate that even small upward pore water flux rates can alter the vertical extent of the temperature envelope. The temperature envelope illustrated in Figure 3-12 is slightly asymmetric due to the time period simulated in the heat transport model (September to March). If the timeline was extended to an entire year, the results are expected to be more symmetric.

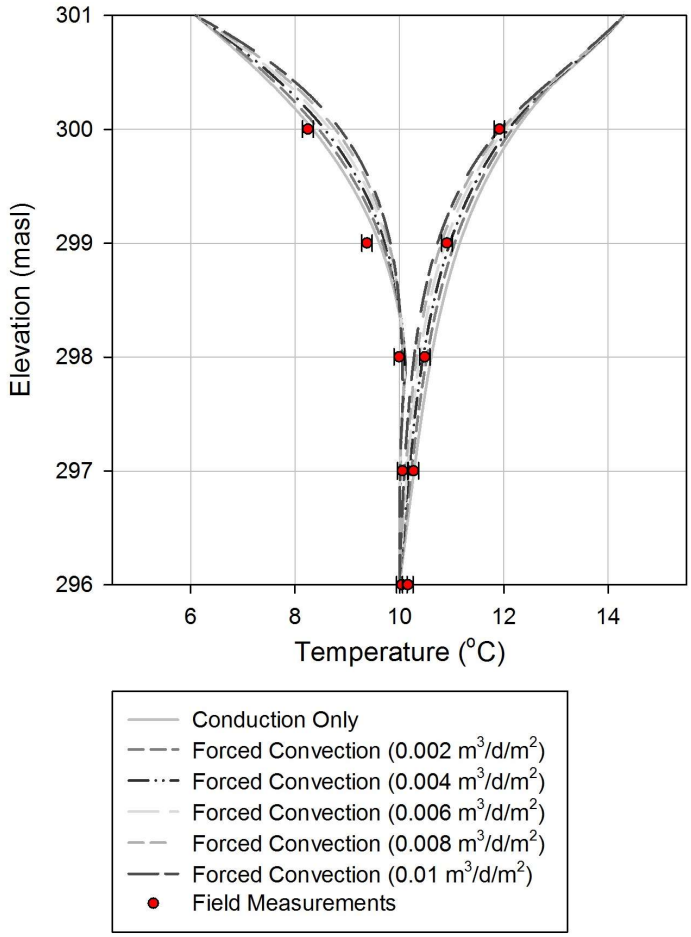

Figure 3-12. Temperature envelopes for field data (with error bars) and modelled scenarios.

Results from the numerical simulations were compared with the observed temperature profiles to determine if a particular set of heat transport parameters provided a match for the observed field conditions (based on the RMSE determined for the maximum and/or minimum temperature profiles, Table 3-4). Maximum and minimum temperatures over the entire study period as measured in the field were plotted with depth (Figure 3-12). Maximum temperatures measured in the field fall along the temperature profile produced by the forced convection simulation with an upward pore water flux of 0.006 $m^3/d/m^2$ (RMSE of 0.10 °C).

The measured minimum temperatures are lower than the simulated values produced by the heat transport models. The heat transport model that generated a temperature profile closest to the minimum values measured in the field was the conduction-only model (RMSE of 0.12 °C). Consequently, the maximum and minimum in-situ temperatures appear to indicate two different thermal regimes in the FFT when compared to the heat transport models; the maximum in-situ

temperatures suggest a forced convective heat transport regime while the minimum temperatures are closer to a conduction-only heat transport regime.

The minimum temperature envelopes produced by the models with a fall mixing event through the top 0.5 m or 1 m of FFT are provided in Figure 3-13. These simulations provided a better fit for minimum temperatures measured in the field. When a 0.5 m mixing event was added to the models, the minimum field temperatures follow a conduction-dominant thermal regime (RMSE of 0.05 °C). When a 1 m mixing event was incorporated, the forced convection models with an upward flux of 0.006 $m^3/d/m^2$ provided the best fit for the field data (RMSE of 0.08 °C).

The maximum temperature envelopes for the FFT mixing models were similar to the original non-mixing models, as mixing was assumed to occur after the warm season. Thus, the maximum temperature profile continued to indicate that the heat transport regime was forced convection with an upward water flux of 0.006 $m^3/d/m^2$. A 1 m mixing event in the FFT was required for the minimum temperature profile to match the forced convective thermal regime indicated by the maximum temperature profiles.

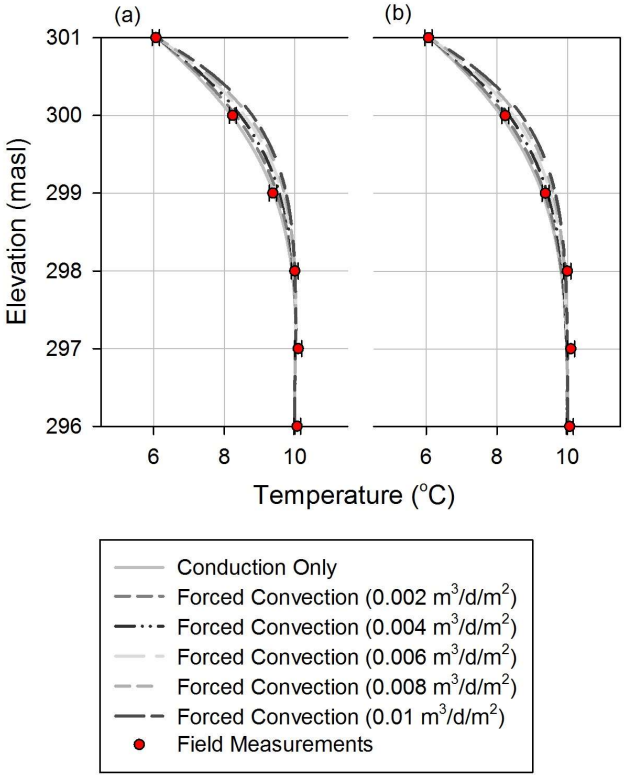

Figure 3-13. Minimum temperature envelopes for field data (with error bars) and models with mixing events of: (a) 0.5 m; and (b) 1 m.

Table 3-4. RMSE of heat transfer models compared to minimum and/or maximum field temperatures (°C).

Advective Flux	No FFT Mixing			0.5 m FFT Mixing			1 m FFT Mixing		
($m^3/d/m^2$)	Min.	Max.	Both	Min.	Max.	Both	Min.	Max.	Both
0	**0.12**	0.18	0.16	**0.05**	0.18	0.13	0.23	0.18	0.21
0.002	0.16	0.14	**0.15**	0.07	0.14	**0.11**	0.17	0.14	0.16
0.004	0.20	0.11	0.16	0.12	0.11	0.12	0.12	0.11	0.12
0.006	0.24	**0.10**	0.18	0.17	**0.10**	0.14	**0.08**	**0.10**	**0.09**
0.008	0.27	0.12	0.21	0.23	0.12	0.18	0.08	0.12	0.10
0.010	0.31	0.15	0.25	0.28	0.15	0.22	0.10	0.15	0.13

3.5 Discussion

Both the heat and isotope transport models indicate that the dominant mass transport regime through the FFT in BML is advection. Both of the tracers also suggest that seasonal mixing of an upper portion of the FFT and lake water does occur in BML. Laboratory measurements of the Bingham yield stress for low solids content FFT produced relatively low yield stress values, and suggested that the top 1.5 m of FFT in BML would exhibit yield stresses below 10 Pa. Thus, the soft tailings near the FFT-water interface in BML would provide minimal resistance to any shear stresses imposed at the interface, confirming that mixing in the FFT is possible.

The isotope transport models provide insight on the potential range of FFT mixing depths. Example mixing depths and corresponding advective flux that produce an isotope profile similar to the field observations are listed in Table 3-5. Thus, the isotope transport model provides an approximate FFT mixing depth associated with each advective mass transport regime.

The heat transport models suggest that advection (with approximately 0.006 $m^3/d/m^2$ of upward pore water flux) was an important mechanism for heat transport within the FFT, coupled with a FFT mixing event of 1 m. The isotope transport models suggested that a mixing depth of 1.1 m (closest to 1 m) was associated with an advective transport regime with an upward flux of 0.004 $m^3/d/m^2$. When this mixing depth and advective flux were used in the heat transport model,

both the minimum and maximum simulated temperature profiles matched those measured in the field (Figure 3-14; RMSE of 0.08 °C).

Table 3-5. Mixing depths and advective flux required to simulate the measured isotope profiles.

Advective Flux ($m^3/d/m^2$)	FFT Mixing Depth (m)
0.001	0.2
0.002	0.5
0.003	0.7
0.004	1.1
0.005	1.4
0.006	1.7

Based on the observed isotope signatures and temperature profiles, the dominant mass transport regime through the FFT in BML was assessed to be 0.004 $m^3/d/m^2$ of advective transport. This value is similar to the FFT dewatering rates estimated independently by Syncrude Canada Ltd. based on field monitoring of the FFT surface at BML (approximately 0.003 $m^3/d/m^2$, based on the measured change in the elevation of the FFT-water interface by ConeTec Investigations Ltd.). The heat and isotope transport models also provided a preliminary estimate of the depth of mixing occurring in the FFT (1.1 m). As previously mentioned, a Seabird 19plus sensor was observed to drop 1 m below the elevation of the FFT-water interface measured on the previous day, during a field investigation in mid-October, 2013. Therefore, the estimated mixing depth is similar to this observed change in the FFT-water interface.

The heat and isotope models only include one mixing event; however, it is possible that the FFT may undergo multiple mixing events during periods of instability in the lake (generally the fall). Further work is necessary to establish the number of potential mixing events occurring in BML. This number of mixing events can be incorporated into the developed heat and mass transport models to confirm the dominant mass transport regime and FFT mixing depth in BML.

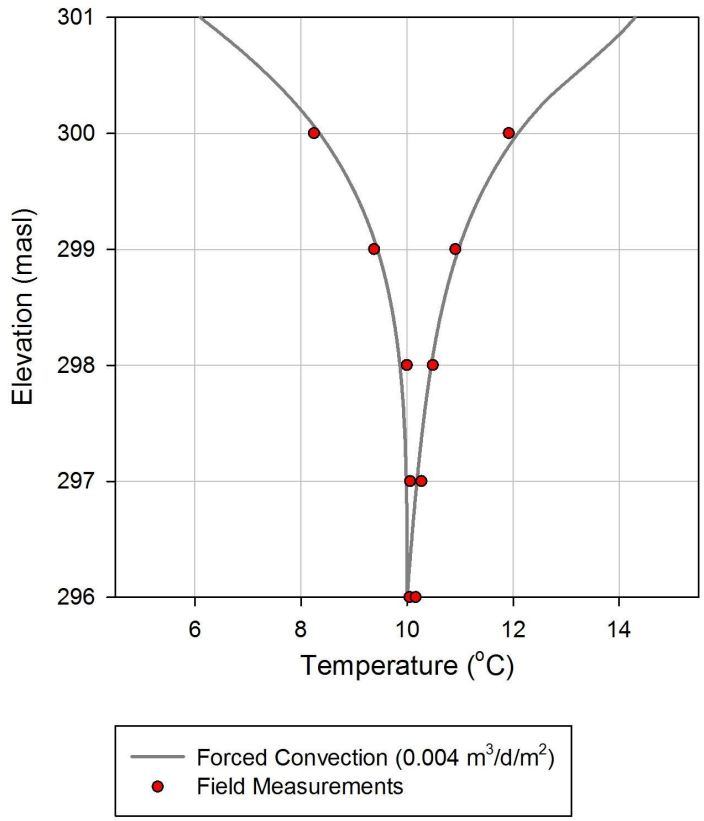

Figure 3-14. Simulated profiles with an upward flux of 0.004 $m^3/d/m^2$ and a 1.1 m FFT mixing event.

3.6 Conclusions

The multi-faceted approach employed in this study allowed for a preliminary evaluation of the mechanisms controlling mass transport of a conservative species through FFT in the first oil sands EPL. These findings provide a starting point for future work on: (1) evaluating reactive mass transport through the FFT in BML; (2) determining a mass balance for BML's water cap (and other EPLs) during the early stages of development; (3) assessing the ideal water cap depth in future EPLs to limit FFT disturbance; (4) estimating the long term mass loading mechanisms from FFT to the water cap in an EPL; and (5) conducting a risk assessment on the water quality and extended impacts of EPLs and their development.

The use of multiple tracers provided a clear picture of the mechanisms controlling mass transport in BML. The combination of heat and stable isotopes of water allowed for the determination of both a flux associated with FFT dewatering (0.004 $m^3/d/m^2$) and an approximate

mixing depth (1.1 m) due to lake turnover events. Based on tailings settlement models for BML (Carrier et al., 2007), pore water release due to dewatering of the FFT declines gradually. Therefore, the results from this study suggest that mass loading from the FFT will decrease over time, with mass transport from the FFT to the water cap becoming increasingly dominated by diffusion. The results of this study also suggest that a greater water cap may be required in future EPLs to prevent mixing of the FFT and to ensure that these soft tailings are isolated from the overlying lake water. Not only do these mixing events produce a rapid mass loading to the water cap, the disturbance of FFT causes high turbidity in the lake water, which could be detrimental to the development and health of lake ecosystems.

Other types of soft tailings possess similar characteristics as FFT, for example, high void ratios and low shear strength. Thus, the dominant mass transport mechanisms in these materials will likely be comparable to the findings from BML, with an advection dominant regime in early years due to tailings settlement and diffusion becoming more important in later years. In addition, the issues observed in this study (e.g. disturbance of the soft tailings) will likely be relevant for the reclamation of unprocessed soft tailings from other types of mining activities.

CHAPTER 4 – CHEMICAL MASS TRANSPORT BETWEEN FLUID FINE TAILINGS AND THE OVERLYING WATER COVER OF AN OIL SANDS END PIT LAKE

This paper summarizes efforts to estimate the mass loading of a conservative tracer (Cl) from the FFT into the BML water cover. The mass balance within the water cover was assessed given the monitored inflow, outflow, and water cover volumes, and Cl concentrations over time. Field sampling determined the FFT pore water Cl concentrations, which were used to develop numerical models similar to the previous multi-tracer study for Cl transport through the FFT. The mass balance and numerical results were compared to corroborate results from the multi-tracer study and to evaluate the mass released to the water cover from in the FFT over the study period.

I, Kathryn Dompierre, assisted in conceptualizing the study, carried out data synthesis and analysis, developed the numerical transport models, completed the mass balance of the water cover, and authored the manuscript. Matthew Lindsay (University of Saskatchewan) led the field program for analyzing the geochemistry of the FFT pore water. Sean Carey, Gordon Drewitt, and Michael Treberg (McMaster University) measured the water outputs and inputs to BML over multiple years and evaluated the water balance of the BML water cover. Rebecca North (University of Saskatchewan) synthesized the water volume and chemistry data for determining the mass balance of the water cover. Contributions to the manuscript are as follows: Kathryn Dompierre (70%), was the main contributor to the manuscript, with Lee Barbour (10%), Rebecca North (5%), Sean Carey (5%) and Matthew Lindsay (10%) providing comments during the review process.

4.1 Introduction

The Canadian oil sands are the third largest known oil reservoir in the world, estimated to contain 166 billion barrels of oil (Government of Alberta, 2016). Oil sands mining has disturbed more than 800 km^2 of land (Government of Alberta, 2014); however, less than 1 % of this area has received regulator certification as reclaimed (Gosselin et al., 2010). In addition, bitumen extraction from oil sands ore generates large volumes of tailings. More than 9.8 $x10^8$ m^3 of fluid

fine tailings (FFT) were stored in tailings impoundments by the end of 2013 (Government of Alberta, 2015).

Management and reclamation of FFT pose substantial geotechnical and environmental challenges. Associated pore waters exhibit elevated concentrations of dissolved inorganic chemical constituents, and organic compounds such as naphthenic acids, petroleum hydrocarbons, and unrecovered bitumen (Allen, 2008; Dompierre et al., 2016; Kavanagh et al., 2011). Fluid fine tailings also exhibit high water content that persists for decades due to low settlement rates (Kasperski and Mikula, 2011). At these high water contents, FFT behaves as a fluid and exhibits low shear strengths. A number of strategies are used to increase FFT strength, including flocculent and coagulant addition, large-scale centrifugation, thin-lift drying, and mechanical filtration (COSIA, 2012*a*). Treated FFT can be integrated into conventional terrestrial reclamation landscapes. However, these methods are expensive, time-consuming, and cannot accommodate daily FFT production.

End pit lakes (EPLs) offer long-term FFT containment with relatively low initial costs (CEMA, 2012). These mine closure landscapes contain FFT deposits under a water cover within decommissioned mine pits. In the future, EPLs will be incorporated into the larger mine closure landscape, and are expected to achieve sufficient water quality for release to natural systems (CEMA, 2012). Thirty EPLs have been included in mine closure plans for the Athabasca oil sands region (AOSR) of Alberta, Canada. Half of these proposed EPLs will incorporate FFT below a water cover (Prakash et al., 2011).

The release of chemical constituents from the FFT will influence the long-term geochemical and biological evolution of an EPL (Dompierre et al., 2016). Mass transport between the FFT and overlying water cover can occur via two key processes: (1) advection and hydrodynamic dispersion driven by FFT dewatering and elevated solute concentrations in FFT pore water (Dompierre et al., 2016); and (2) FFT disturbance due to fluid movement in the water cover (e.g., internal waves) causing a rapid, but intermittent, mass release to the water cover (Dompierre and Barbour, 2016*a*).

This study investigated water movement and chemical mass transport in the first EPL established in the AOSR. Water and mass fluxes between the FFT and the water cover were assessed using a conservative tracer to evaluate the chemical mass balance of the EPL and to track mass transport within the FFT given field sampling and numerical modelling. Chloride (Cl)

was selected as the conservative tracer as it is typically isolated from geochemical reactions (Feth, 1981). Previous studies have used Cl to investigate groundwater flow and seepage to lakes (Cox et al., 2007; Davis et al., 1980; Jacquet, 1976; Lee et al., 1980), and to assess the mass balance of lakes (Rimmer et al., 2005; Sacks et al., 1998).

This investigation provides valuable insight for assessing the geochemical evolution of the water cover and performance of EPLs as an oil sands reclamation strategy. Results will assist in the development of monitoring and management plans for future EPLs. This study also provides insight on the potential for the mass flux over the FFT-water interface to change over time, as it can be compared to previous work on mass movement through the FFT at the first EPL (Dompierre and Barbour, 2016*a*).

4.2 Materials and methods

4.2.1 Study site

Base Mine Lake (BML), the first full-scale demonstration EPL in the AOSR, was established at the Mildred Lake Mine, which is approximately 40 km north of Fort McMurray, Alberta, Canada (Figure 4-1). This region is located in a sub-humid continental climate zone with long cold winters and short summers (Carey, 2008). The mean annual temperature is 1.0 °C and temperatures are below 0 °C for five to six months of the year (Environment Canada, 2015).

Oil sands surface mining began at the Mildred Lake Mine in 1978. The oil sands ore is mined from the McMurray Formation, which contains on average 12 % (w/w) bitumen (long chain hydrocarbons), 3 to 6 % (w/w) water, and 84 to 86 % (w/w) solids (Chalaturnyk et al., 2002). Bitumen is extracted by adding hot water to reduce viscosity, sodium hydroxide to disperse clay particles, and aeration to promote bitumen flotation (Caughill et al., 1993; Masliyah et al., 2004). The extracted bitumen is further upgraded to synthetic crude oil and the residual sand-clay slurry is hydrotransported to Mildred Lake Settling Basin (MLSB; Figure 4-1). Following deposition in this tailings pond, the sand-sized particles quickly settle from the tailings slurry leaving a dense, warm fluid suspension called fluid fine tailings (FFT).

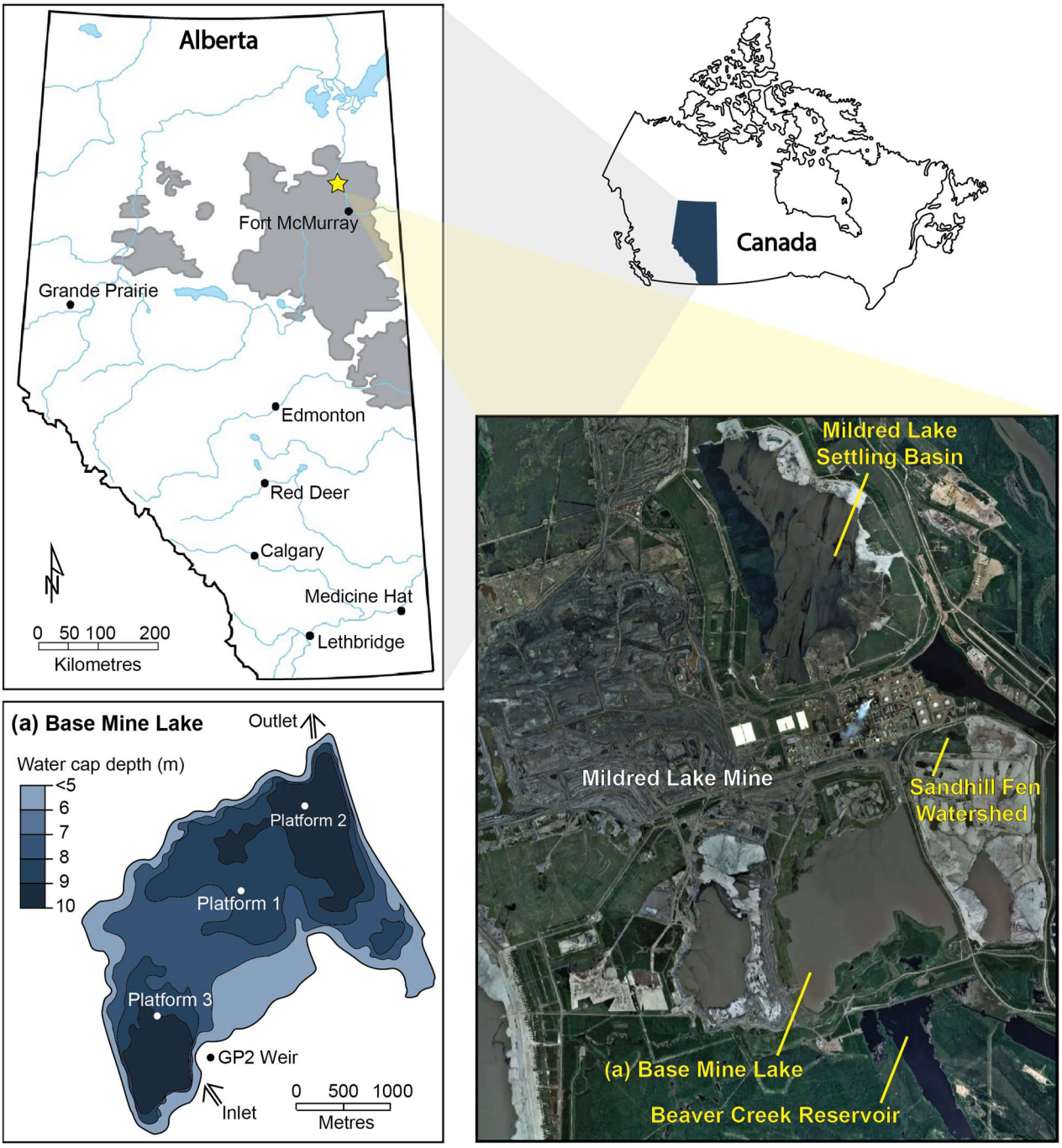

Figure 4-1. Mildred Lake Mine location (starred) relative to known oil sands deposits (grey shaded areas) and aerial photo of the site; inset (a) shows the BML monitoring locations and water cover depth in June 2013.

Fluid fine tailings pore water chemistry is dominated by oil sands process-affected water (OSPW), which contains significant concentrations of dissolved ions (e.g., sodium, chloride,

bicarbonate), naphthenic acids, petroleum hydrocarbons, and unrecovered bitumen (Allen, 2008; Kavanagh et al., 2011). The initial FFT solids content is 25 to 35 % (w/w), and is predominantly comprised of quartz and clay minerals including kaolinite, illite, chlorite, and illite-smectite (Dompierre et al., 2016; Osacky et al., 2013*b*). The residual bitumen content typically ranges from 1 to 6 % (w/w). The FFT hydraulic conductivity is expected to range from 5×10^{-8} to 5×10^{-5} m s^{-1} based on typical FFT water content values and previous laboratory results (Suthaker and Scott, 1996).

Base Mine Lake was constructed within a decommissioned mine pit referred to as West In-Pit. Fluid fine tailings were dredged from MLSB and pumped into the northeast corner of West In-Pit from 1994 to 2012. Throughout this period, BML was part of the recycle water circuit (Han et al., 2009) so a 3 to 5 m water cover was maintained over the FFT to provide OSPW storage for various mine processes. This mine closure landscape was commissioned as an EPL in November of 2012. At this time, the maximum FFT depth in BML was 45 m, corresponding to a total FFT volume of approximately 1.9×10^9 m^3. The average FFT temperature is approximately 13 °C (Dompierre et al., 2016). After commissioning, fresh water was pumped into BML from Beaver Creek Reservoir (BCR; Figure 4-1) during ice-free months. Water was concurrently pumped out of BML – for use in the bitumen extraction process – to maintain a lake surface elevation of 308.5 ± 0.5 metres above sea level (masl). The average water cover depth was 8.5 m at the beginning of 2013. In October 2015, near the end of the study period, the estimated water cover volume was 5.8×10^7 m^3 with a surface area of approximately 7.8 km^2.

The water cover responds to seasonal temperature cycles in a similar manner as natural temperate, northern lakes (e.g., Lawrence et al., 2016; Oswald and Rouse, 2004; Rouse et al., 2003). During the summer months, the water cover is thermally stratified from the end of May to the beginning of September. The epilimnion (upper portion of the water cover) temperature increases throughout June to 20 °C and stays at this temperature until September. Concurrently, the hypolimnion (lower portion of the water cover) gradually warms to 15 °C. In the fall, the water cover is fully mixed from the beginning of September until ice forms in November. Over the winter season, the water column exhibits inverse stratification below the ice cover. Temperatures remain relatively constant throughout this period with water near the ice at 0 °C and a temperature of 4 °C near the FFT-water interface. The ice cover melts by the end of April,

which is followed by a weaker and more irregular spring turnover, as compared to the fall turnover (Lawrence et al., 2016).

The FFT is currently undergoing hindered settlement or self-weight consolidation (COSIA, 2012*c*), which means that the FFT near the pit bottom dewaters first, with the expressed pore water creating a vertical pore water flux through the FFT. Pore water movement is generally expected to be upward due to the relatively low hydraulic conductivity of the underlying formations. Clearwater Formation shales and siltstones form the BML pit and exhibit a mean vertical hydraulic conductivity of 8 x10^{-10} m s^{-1}. Initial FFT settlement would have occurred during the first few years after deposition; however, high water contents are expected to persist for an extended time period (Kasperski and Mikula, 2011). These slow settlement rates are due to the addition of dispersants (sodium hydroxide) during bitumen extraction and naturally occurring surfactants (asphaltic acids) present in the ore that are released during heating (Chalaturnyk et al., 2002; Jeeravipoolvarn, 2009).

A preliminary FFT consolidation model, developed to evaluate the long-term settlement in BML, estimated settlement rates of approximately 1 m a^{-1} after deposition, decreasing exponentially over 30 years to approximately 0.1 m a^{-1}. A field study by Dompierre and Barbour (2016*a*) found that the FFT settlement generated an upward pore water flux of 0.004 m^3 m^{-2} d^{-1} (1.5 m^3 m^{-2} a^{-1}) approximately one year after BML was commissioned.

Two approaches were used to assess chemical mass flux from the FFT to the overlying water cover, both of which used Cl as a conservative tracer. The first evaluated the Cl mass balance within the water cover to determine the conservative mass flux from FFT. The chemical mass balance included an initial assessment of the water balance within the water cover, and a field sampling campaign to characterize the Cl concentrations of BML and all inflow and outflow waters. The second investigated the mechanisms controlling mass transport within the FFT, using pore-water Cl concentrations to develop numerical models for predicting mass movement across the FFT-water interface.

4.2.2 Sample and data collection

A field investigation evaluated the volumes and mass associated with the input and output waters at BML. Water and mass inputs included water pumped in from BCR, precipitation (snow and rain), runoff from the surrounding watershed, and pore water released from the underlying FFT. Outputs included water and mass pumped from the water cover for use in the processing

plant, and water loss due to evaporation. Groundwater interactions with the water cover were assumed negligible due to the relatively low hydraulic conductivity of the formation surrounding the pit.

The water volume pumped into and out of BML each day was monitored with Rosemount magnetic flowmeters (accuracy of ±0.25 %, Emerson Process Management, Shakopee, MN, USA). The water cover surface elevation was measured using GPS, while sonar surveys, completed in October of each year, verified the FFT-water interface elevation.

Rainfall volumes were monitored with three unobstructed CS700 tipping-bucket rainfall gauges (Campbell Scientific, Edmonton, AB, Canada) located at the adjacent Sandhill Fen Watershed (Figure 4-1). Snowfall was estimated using the mean value from three CS725 snow water equivalent sensors (Campbell Scientific, Edmonton, AB, Canada) corroborated with annual snow surveys at Sandhill Fen. These values were compared with snow water equivalent data reported by Environment Canada at the Mildred Lake weather station (Environment Canada, 2015). The Sandhill Fen likely accumulates more snow as water equivalent than BML as it is more sheltered; however, both environments are subject to wind redistribution. Runoff volumes from the contributing watershed were measured at a weir on the south side of BML (GP2 weir; Figure 4-1). The observed runoff volumes were assumed to be representative of the entire terrestrial watershed, which covers a 6.6 km^2 area or approximately 80 % of the water cover surface area.

Evaporation from the water cover was measured using the eddy covariance (EC) technique (Aubinet et al., 2012). The EC system involved a LI-7200 enclosed path infrared gas analyzer (LI-COR, Lincoln, NE, USA) and R3-50 3D sonic anemometer (Gill Instruments Ltd., Lymington, UK), and was installed in the centre of BML at Platform 1 (Figure 4-1). Wind speed and water vapour concentrations were measured at 10 Hz and covariances were computed for 30-minute intervals using EddyPro® LI-COR. During short periods (< 2 hours) when the EC system was not working, evaporation was estimated using linear interpolation. For longer periods, a monthly logistic regression model was developed for evaporation as a function of net radiation, wind speed, and vapour pressure deficit measured at Platform 1 to provide continuous data.

Samples of the BML water cover were frequently collected between May 2013 and October 2015. The samples were collected bi-weekly during the open water season, and once under the ice in the winter. Water samples were collected at several stations around BML (Platforms 1, 2,

and 3; Figure 4-1). Inflow and outflow samples were also obtained during routine sampling when the pumps were in operation. Rainfall samples were collected from five locations around the BML perimeter in the fall of 2015, while snow samples were obtained at 10 locations over the frozen water cover surface in March 2015. Runoff at the GP2 weir was sampled during the spring melt period (March 18 to June 3, 2014; March 27 to April 15, 2015). All water samples were collected into HDPE bottles and sealed with no headspace. The samples were chilled until they were analyzed at a commercial laboratory. The Cl concentrations were quantified by ion chromatography (IC; EPA Method 300.0) on samples passed through 0.45 μm polyethersulfone (PES) membranes.

Tailings samples were obtained at high spatial resolution across the FFT-water interface at Platforms 1, 2, and 3 (Figure 4-1) on August 4 and 5, 2015. These samples were collected using a custom-built fixed interval sampler (FIS) deployed using a boat-mounted overhead winch and pulley system. This sampler was comprised of 20 discrete sampling cylinders positioned at 0.1 m depth intervals. Each cylinder contained a pneumatically-controlled piston with a 250 mL total displacement volume. Compressed nitrogen gas (275 kPa) was used to maintain the pistons in the closed position while the FIS was slowly lowered to the FFT-water interface. Five cylinders were positioned above and fifteen below the FFT-water interface, which was first determined by active sonar (Dompierre et al., 2016). After a 10-minute settlement period, the compressed nitrogen was evacuated and the pistons retracted to the open position using a vacuum pump. After approximately 5 minutes, the FIS was retrieved to surface, one 250 mL HDPE bottle was threaded onto each cylinder, and the samples were extruded using compressed nitrogen to move the pistons back to the closed position. Pore water was extracted from FFT solids by centrifugation at 10,000 rpm for 30 minutes and passed through 0.45 μm polyethersulfone (PES) membranes. The pore water samples were stored in HDPE bottles with zero headspace and refrigerated until the Cl concentrations were quantified by ion chromatography (IC; EPA Method 300.0).

4.2.3 Mass balance calculations

An annual water balance was completed for the entire BML system (FFT and water cover; Figure 4-2) from November 1, 2013 to October 31, 2014 (Period 1) and November 1, 2014 to October 31, 2015 (Period 2). The measured elevation change of the water surface was compared to the calculated net water flux over the water surface, dS (m^3 or mm), determined by:

$$dS = I_W - O_W = V_{p_{in}} + V_{prec} + V_{ro} - V_{evap} - V_{p_{out}} \quad (4.1)$$

where I_W is the total water volume (depth) contributed to BML from the inputs (pump-in water, $V_{p_{in}}$; precipitation, V_{prec}; and runoff, V_{ro}) and O_W is the total volume (depth) removed by the outputs (pump-out water, $V_{p_{out}}$; and evaporation, V_{evap}). Pore-water release from the FFT was not considered to be an input for the above water balance calculation as it does not affect the water surface elevation but instead causes the elevation of the water cover bottom (FFT-water interface) to drop over time. Water movement over the pit walls and base was assumed to be negligible.

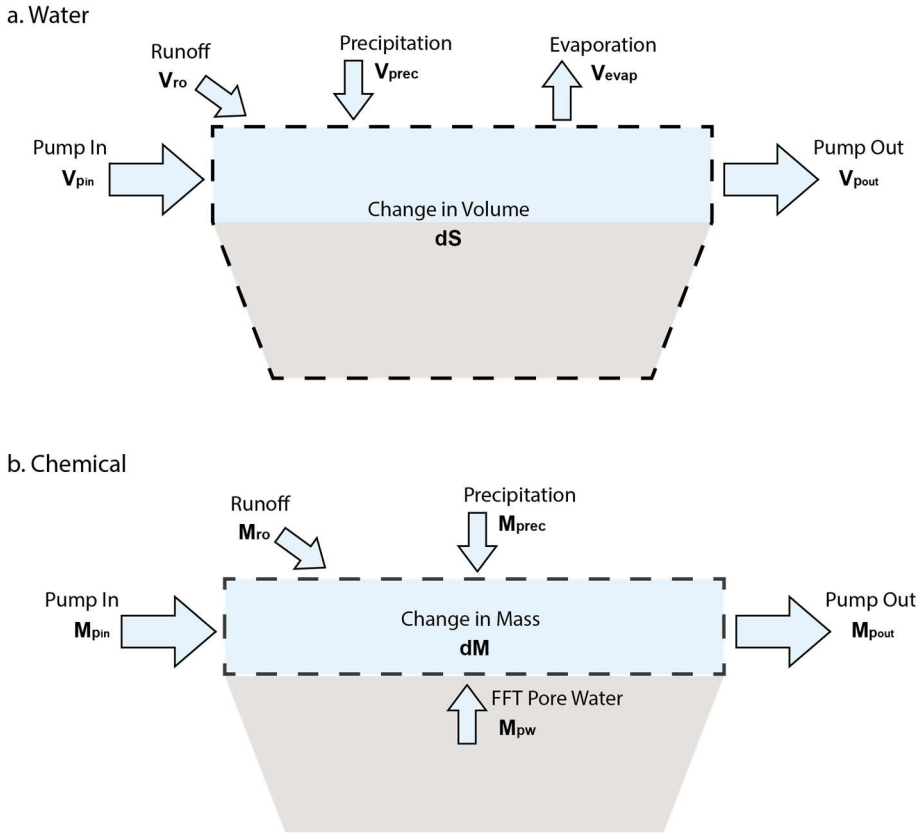

Figure 4-2. Inputs, outputs, and the domain (outlined by the thick dashed line) associated with the (a) water and (b) chemical mass balances.

The change in Cl stored in the water cover was calculated for the same two periods as the annual water balances (November 1, 2013 to October 31, 2014; November 1, 2014 to October 31, 2015) using the following equation:

$$dM = I_M - O_M = M_{p_{in}} + M_{prec} + M_{ro} + M_{pw} - M_{p_{out}} \quad (4.2)$$

where dM represents the change in Cl stored in the lake (g), I_M, is the total mass of Cl associated with the inputs (FFT pore water, M_{pw}; pump-in water, $M_{p_{in}}$; precipitation, M_{prec}; and runoff, M_{ro}). The Cl removed from the lake due to outputs, O_M, was the chemical mass associated with the pump-out water ($M_{p_{out}}$). The product of the volume, V (m^3), and Cl concentration, C (g m^{-3} or mg L^{-1}), of each input or output (except for the FFT pore water) was used to determine its associated chemical mass. Pore water released by the FFT was not directly measured and represents an unknown in the above equation (and in **Error! Reference source not found.**).

The Cl in the lake at the beginning and end of each period was calculated with the average concentration throughout the whole water cover, multiplied by the water cover volume at the specified time. Thus, the change in Cl stored in the lake, dM, was calculated by:

$$dM = V_{L_2} \cdot C_{L_2} - V_{L_1} \cdot C_{L_1} \tag{4.3}$$

where V_L is the lake volume and C_L is the volume weighted average chloride concentration in the lake at the beginning (1) and end (2) of the mass balance period. The water cover volume was determined from the water surface elevation, FFT-water interface elevation data, and pit capacity curves describing the volume below a given elevation (provided in Appendix B).

The mass released by the FFT, M_{pw}, was determined by rearranging Equation (4.2) to:

$$M_{pw} = (V_{L_2} \cdot C_{L_2} - V_{L_1} \cdot C_{L_1}) - V_{p_{in}} \cdot C_{p_{in}} - V_{prec} \cdot C_{prec} - V_{ro} \cdot C_{ro} + V_{p_{out}} \cdot C_{p_{out}} \tag{4.4}$$

and the average Cl mass flux from the FFT (g m^{-2} s^{-1}) was calculated by dividing the Cl released from the FFT (M_{pw}) by the area associated with the FFT-water interface and the total time (1 year). This area is expected to change as FFT settles due to the sloping pit walls in BML.

A sensitivity analysis was conducted to evaluate which assumptions and inputs to the mass balance equation were most likely to influence the calculated FFT mass flux. The sensitivity analysis considered the water cover volume, which was affected by both the water surface and FFT-water interface elevation, the surface area of the FFT contributing to mass release, and the concentrations associated with the water cover, precipitation, runoff, pump-in, and pump-out waters. The baseline used for the sensitivity analysis was the original mass balance calculation. Each input was altered over a range of expected values while all other values remained the same as the baseline case. The range of values used for each input was based on the expected error

associated with its measurement. The maximum and minimum FFT mass fluxes calculated with each range were compared to the baseline FFT mass flux.

4.2.4 Numerical modelling

One-dimensional mass transport models for advection and hydrodynamic dispersion (or advection-dispersion) were developed using a commercial finite element simulation software for ground water flow and mass transport (CTRAN/W, GEO-SLOPE International Ltd., 2012; SEEP/W, GEO-SLOPE International Ltd., 2013). The model domain was a 5 m FFT column with continuously changing volumetric water content with depth, to represent the variation in solids content observed in the field (Dompierre and Barbour, 2016*a*). The model domain depth was sufficient to capture the observed transition of pore water concentrations from typical FFT signatures to that of the overlying water cover (Dompierre and Barbour, 2016*a*). This region is also expected to have a relatively consistent pore water flux rate as pore water flow is primarily generated from the bottom of the FFT deposit during preliminary self-weight consolidation.

The initial and boundary conditions were set as normalized concentrations based on the Cl values measured in the field. The minimum Cl value observed in the water cover corresponded to a normalized concentration of 0.0, and the maximum Cl value, found within the FFT pore water, was associated with a normalized concentration of 1.0. Thus, the initial concentration in the FFT was set to a normalized value of 1.0, as was the lower boundary of the modelled domain. The upper boundary condition changed over time based on the results from the lake water chemistry sampling program. (Detailed information on the models is provided in Appendix A.)

The model was set to begin in May 2013, when freshwater pumping began, and continued until October 2015. In each simulation, a mass transport regime (i.e. diffusion only or advection-dispersion) was maintained throughout the modelled time period. The upward water fluxes applied to the advection models ranged from 0.0005 to 0.01 $m^3\,d^{-1}\,m^{-2}$. These values were based on the 2013 and 2014 FFT dewatering rates determined by the FFT-water interface sonar surveys and previous tracer work at BML (Dompierre and Barbour, 2016*a*).

The coefficient of molecular diffusion was estimated using the volumetric water content of the FFT with depth, and the relationship between porosity and the diffusion coefficient established by Boudreau (1996). The free water diffusion coefficient for Cl was taken from Cussler (1997) and was modified based on the average in-situ FFT temperature (10 °C) after Li

and Gregory (1974). The volumetric water content varied from 86 % to 82 %, and the associated diffusion coefficients ranged from 7.8 x 10^{-10} to 6.6 x 10^{-10} m^2 s^{-1}.

Longitudinal dispersivity was included in the models and was assumed to be 0.01 times the plume length (Kamp et al., 1994; Gelhar et al., 1992). The plume length was observed to be 0.4 m, corresponding to the depth over which the Cl concentrations transitioned from average FFT pore water values to average water cover values. The linear pore water velocities, calculated by dividing the water flux by the volumetric water content of the top FFT layer (porosity), were found to range from 0 to 1.4 x10^{-7} m s^{-1}. The assumed dispersivity value and the calculated pore water velocities produced a range in values for the coefficient of mechanical dispersion from 0 to 4.6 x10^{-10} m^2 s^{-1}.

Additional model scenarios were developed to simulate a disturbance within the top portion of the FFT during the fall turnover. Two disturbance depths, 0.5 m and 1 m, were added to the model by changing the FFT pore water concentration in the disturbed zone to the water cover concentration immediately before the disturbance events (October 15, 2013 and October 15, 2014). These model scenarios were developed to evaluate previous evidence of FFT disturbance provided by stable isotopes of water and temperature profiles measured in BML (Dompierre and Barbour, 2016*a*).

The Cl concentration profiles generated by the numerical models were compared to those measured in the field on August 4 and 5, 2015. The Root Mean Square Error (RMSE) between each modelled scenario and the field results was calculated to provide a preliminary estimate for the model providing the best fit. The numerical models were also used to investigate mass flux rates over the FFT-water interface and cumulative mass released from the FFT given the simulated advection-dispersion transport regimes.

4.3 Results

4.3.1 Water and chemical balance

Pumping from BCR represented the largest water input to BML during both sampling periods (Table 4-1). The pump was operated from May to October and contributed more than 6 x10^6 m^3 of water to BML each year. This volume is approximately 10 % of the total water cover volume and corresponds to a water depth greater than 780 mm when normalized to the BML surface area. Rainfall was the next largest water input, followed by snow and runoff.

Table 4-1. Water volume and mass of Cl associated with each input (+) and output (−)

Input / Output	Period 1[a] Depth (mm)	Period 1[a] Volume ($x10^6$ m^3)	Period 1[a] Cl Mass ($x10^6$ g)	Period 2[b] Depth (mm)	Period 2[b] Volume ($x10^6$ m^3)	Period 2[b] Cl Mass ($x10^6$ g)
Rain	309	2.36	1.9	254	1.53	1.3
Snow	55	0.42	0.1	50	0.39	0.2
Runoff	29	0.23	2.5	21	0.16	1.4
Pump In	852	6.56	22.4	780	6.01	16.4
Pump Out	−955	−7.35	−2895.7	−953	−7.34	−2609.4
Evaporation	−351	−2.70	-	−351	−2.70	-
NET	−60	−0.40		−198	−1.96	

[a]Period 1: Nov. 1, 2013 to Oct. 31, 2014.
[b]Period 2: Nov. 1, 2014 to Oct. 31, 2015.

The largest water withdrawal was associated with pumping, which accounted for a larger water volume than pumping inputs from BCR. Evaporation from the lake surface was very similar over the two measurements periods, even though the monthly evaporation rates differed between Period 1 and Period 2. The evaporation rates measured in 2014 and 2015 were considerably less than calculated open-water potential evaporation (Penman, 1948) and were lower than values determined for natural lakes in the same region (Ferguson et al., 1970; Blanken et al., 2000).

A net water loss was determined for both of the water balance periods (60 mm in Period 1 and 198 mm in Period 2). The water loss generally corresponded to the measured surface elevation changes of 50 mm in Period 1 and 240 mm in Period 2. Temporal trends in calculated storage and measured water cover surface level were generally similar (Figure 4-3). Uncertainty associated with the water balance was due to sampling error (rain, snow, and runoff samples), instrumentation error (pump in and pump out flowmeters, evaporation EC system, and rain gauges), and sample representation (rain, snow, runoff, and evaporation samples). Pumped water represents the largest flow in and out of BML, and was assumed to be the largest contributor to water balance uncertainty. The pumps shut off when the associated flowmeter stopped working so uncertainty of the pumped water was only due to instrumentation error. Uncertainty of these measurements would be approximately ±0.016 $x10^6$ m^3 for the pump in and ±0.018 $x10^6$ m^3 for the pump out volumes, given the flowmeter accuracy (±0.25 %).

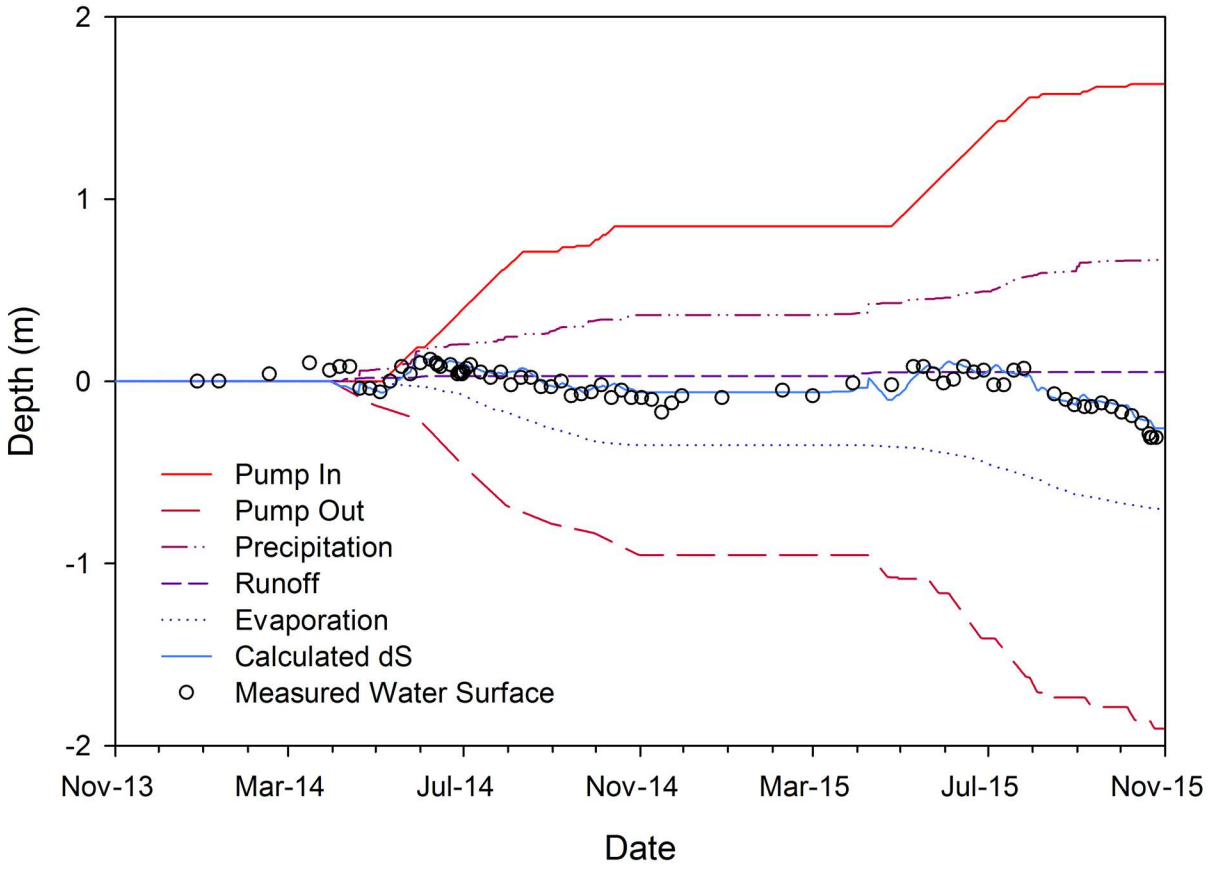

Figure 4-3. Cumulative annual water balance for Period 1 and Period 2 with the measured inputs and outputs (dashed lines), the calculated cumulative change in surface elevation (thick blue line) and measured cumulative change in water surface elevation (circles).

The average runoff Cl concentration was 19.2 mg L^{-1} in Period 1 and 8.8 mg L^{-1} in Period 2; while the average rain and snow Cl concentrations were 0.82 and 2.25 mg L^{-1}, respectively, measured over both periods. Chloride inputs from precipitation and runoff were relatively small compared to the mass contributed from the pumps (Table 4-1), even though this water had relatively low average concentrations of 3.3 mg L^{-1} in Period 1 and 3.1 mg L^{-1} in Period 2. The pump out water had an average concentration of 449.2 mg L^{-1} in Period 1 and 410.4 mg L^{-1} in Period 2. The Cl mass associated with the pump out water was at least an order of magnitude greater than the combined contributions from precipitation, runoff, and the pump in water.

The average Cl concentrations in the water cover decreased over time (Figure 4-4). The initial water cover Cl concentration was 640 mg L^{-1} in May 2013. This value was similar to Cl

concentrations in OSPW measured at the Mildred Lake mine site (Allen, 2008; Dompierre et al., 2016). The initial water cover chemical composition was typical of OSPW because this system was part of the recycle water circuit up until being commissioned as an EPL. The average water cover Cl concentration decreased from greater than 600 mg L^{-1} to approximately 400 mg L^{-1} by the fall of 2015, primarily due to freshwater inputs from BCR. Small fluctuations in the water cover Cl concentration were observed over the monitored period, likely due to transient changes in evaporation rates or pumping, and possibly due to seasonal stratification of the water cover. The yearly mass balance method was chosen, as opposed to a monthly or daily mass balance, to limit the uncertainty associated with this seasonal variability.

The water cover volume varied within Period 1 and 2 due to changes in the water surface elevation and the FFT-water interface. The water cover volume increased from 5.1 $x10^7$ m^3 to 5.6 $x10^7$ m^3 during Period 1 and to 5.9 $x10^7$ m^3 by the end of Period 2. A concomitant decrease in the FFT-water interface elevation also caused the FFT surface area contributing to pore water release to decrease due to a slight narrowing of the pit with depth. The cross-sectional area associated with the FFT-water interface was estimated to be approximately 6.5 $x10^6$ m^2 in November 2013, 6.4 $x10^6$ m^2 in November 2014, and 6.3 $x10^6$ m^2 in November 2013.

Based on the change in mass stored in the water cover and the mass inputs and outputs over the two measurement periods, the calculated mass contribution from the FFT was 1.9 $x10^9$ g in Period 1 and 1.8 $x10^9$ g in Period 2. Given the average FFT-water interface surface area during each period, the mass released from the FFT was 300 g m^{-2} in Period 1 and 280 g m^{-2} in Period 2. These values are associated with estimated mass fluxes of 0.81 g m^{-2} d^{-1} (Period 1) and 0.76 g m^{-2} d^{-1} (Period 2) from the FFT to the overlying water cover. This mass flux represented the largest chemical loading to the water cover each year, as it was approximately 99% of the total mass inputted to BML in both periods.

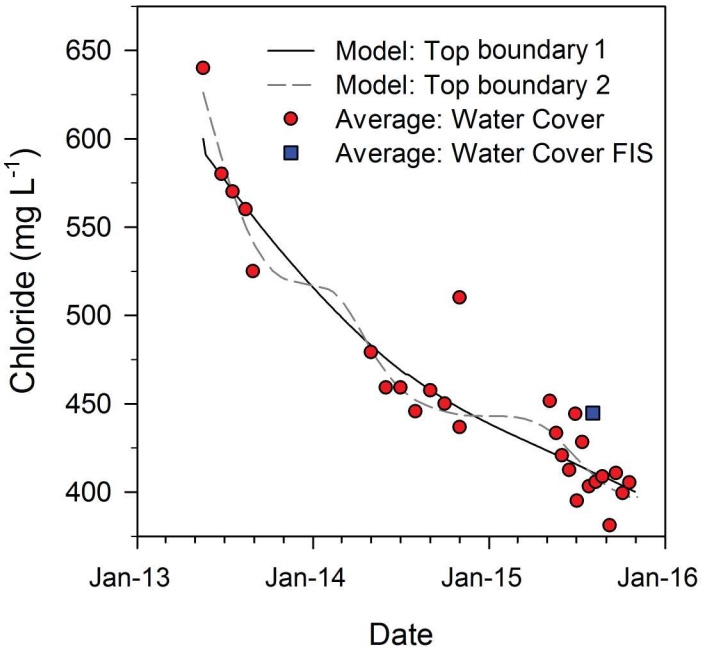

Figure 4-4. Average water cover Cl concentrations from the long-term chemistry sampling program (circles) and measured by the high-resolution fluid sampling (square); water cover concentration trends (solid and dashed lines) used for the upper boundary condition in the numerical models.

The sensitivity analysis illustrated that the calculated mass flux from the FFT was not significantly affected by variability in the input and output water concentrations nor changes to the FFT surface area contributing to the mass loading (Table 4-2). The mass balance calculations were most sensitive to the mass stored in the water cover at the beginning and end of the mass balance periods. The variability associated with the water cover volume and concentration, both used to determine the stored mass, caused the largest shift in the calculated FFT mass input. The sensitivity analysis suggests that the potential mass flux from the FFT could vary from 0.5 to 1.1 g m^{-2} d^{-1} in Period 1 and 0.5 to 1.0 g m^{-2} d^{-1} in Period 2.

Table 4-2. Sensitivity analysis ranges and associated percent change in calculated FFT mass input to the water cover

Input	Sensitivity Analysis Range		Change in Calculated FFT Mass Input[d]	
	Period 1	Period 2	Period 1	Period 2
Water cover volume (m^3)	± 657,000[a]	± 650,000[a]	± 32.9	± 27.9
FFT surface area (m^2)	± 200,000[a]	± 200,000[a]	± 3.1	± 3.1
Lake concentration (mg L^{-1})	± 10[a]	± 10[a]	± 26.5	± 31.6
Input concentrations:				
Rain (mg L^{-1})	0.2 – 6.0[b]	0.2 – 6.0[b]	-0.6 – 0.1	-0.4 – 0.1
Snow (mg L^{-1})	0.1 – 3.0[c]	0.1 – 3.0[c]	± 0.0	± 1.0
Runoff (mg L^{-1})	5.8 – 53.4[a]	5.8 – 53.4[a]	-0.3 – 0.1	-0.4 – 0.0
Pump in (mg L^{-1})	± 1[a]	± 1[a]	± 0.3	± 0.3
Pump out concentration (mg L^{-1})	± 10[a]	± 10[a]	± 3.3	± 3.6

[a]Based on the observed variability or uncertainty associated with the field measurements.
[b]According to field measurements conducted at a nearby reclamation site (personal communications, Jonathan Price, University of Waterloo).
[c]After snowpack Cl concentrations measured by Murray (1981).
[d]Expressed as a percent of the originally calculated FFT mass input.

4.4 Mass transport modelling

High-resolution depth profiles of Cl concentrations across the FFT-water interface were similar among the three sampling locations (Figure 4-5). Concentrations at FFT-water interface were consistent with Cl values in the overlying water cover. However, Cl concentrations transition to a value representative of deeper FFT pore water within 0.5 m from the FFT-water interface. The transition zone depth was similar to that observed for the stable isotopes of water (Dompierre and Barbour, 2016*a*).

The Cl concentrations in the water cover near the FFT-water interface were also consistent among the three sample locations (Platforms 1, 2, and 3; Figure 4-1) with an average value of 440 mg L^{-1} and a standard deviation of 8.2 mg L^{-1}. These values were slightly higher than the average Cl concentration measured by the long-term water cover chemistry sampling program in August 2015 (Figure 4-4). The values obtained were likely higher because the sample was collected from the region just above the FFT-water interface during summer stratification. This region would be affected by FFT pore water release during this stable period, whereas the top layer generally exhibits lower electrical conductivity.

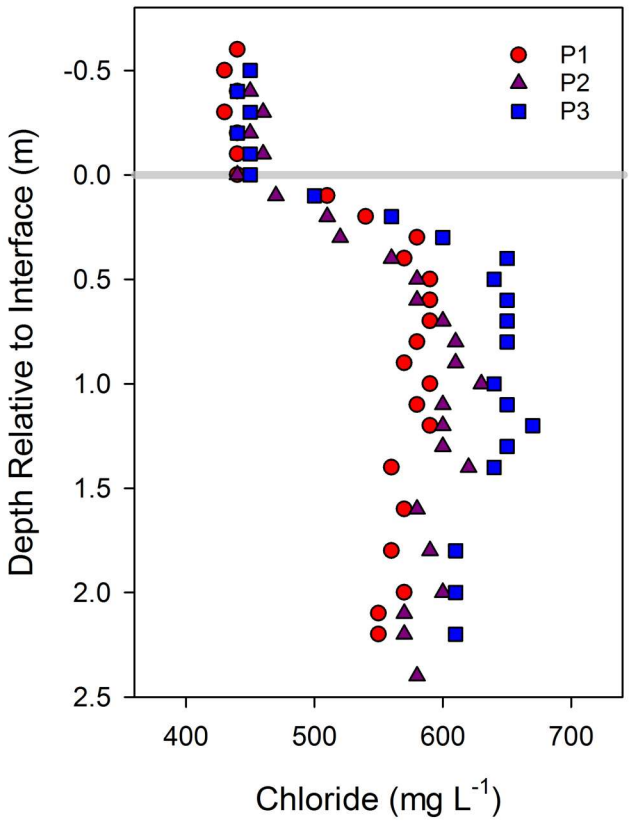

Figure 4-5. Depth profiles of dissolved Cl concentrations for FFT samples collected in August 2015. Depths are presented relative to the FFT-water interface, which is denoted by the solid horizontal line.

The pore water concentrations greater than 0.5 m below the FFT-water interface varied between sample locations; 580 ± 12 mg L^{-1} at Platform 1, 600 ± 18 mg L^{-1} at Platform 2, and 640 ± 19 mg L^{-1} at Platform 3. These values were consistent with water cover concentrations measured in May 2013, before substantial freshwater addition occurred (Figure 4-4). The pore water concentrations below 1.5 m were slightly lower than those between 0.5 and 1.5 m. This suggests that pore water Cl concentrations may have increased with time as FFT was placed in BML. A general enrichment of OSPW, which constitutes the FFT pore water, has been observed due to water reuse for the bitumen extraction process through the recycle water circuit (Baer, 2014; Baer and Barbour, 2013).

A continuously decreasing concentration was specified at the top of the modelled profile (Figure 4-4, top boundary 1) to reflect the water cover concentration trends measured by the

long-term sampling program. The numerical model with a diffusion-only mass transport regime and no FFT disturbance produced a 0.7 m transition depth; however, when an advective flux was added to the models, the transition zone depth decreased (Figure 4-6). This trend was similar for the simulations with FFT disturbance; however, the transition zone depth also increased with disturbance depth. Advection rates of 0.006 to 0.010 $m^3\ m^{-2}\ d^{-1}$ produced very similar Cl profiles within the FFT for all modelled disturbance depths.

The measured Cl profiles were normalized based on the average FFT pore water concentration at each location and the minimum concentration measured in the water cover (380 mg L^{-1}). The normalized concentration profiles were compared to the simulation results (Figure 4-6; Table 4-3). The RMSE values determined for the simulations with advection rates of 0.008 and 0.010 $m^3\ m^{-2}\ d^{-1}$ were not included in Table 4-3 as they were similar to the values provided for 0.006 $m^3\ m^{-2}\ d^{-1}$.

Table 4-3. RMSE (%) for each modelled scenario compared to field concentrations at each platform (P)

Advective Flux	**No FFT Mixing**			**0.5 m FFT Mixing**			**1 m FFT Mixing**		
($m^3\ m^{-2}\ d^{-1}$)	P1	P2	P3	P1	P2	P3	P1	P2	P3
0	12.5	7.8[a]	8.8[a]	29.4	18.2	26.2	49.2	41.9	46.9
0.0005	7.1[a]	13.9	9.7	19.0	9.3	15.0	42.7	34.0	40.9
0.001	9.2	17.7	13.9	9.7[a]	8.9[a]	7.4[a]	35.4	25.2	33.2
0.002	11.4	20.1	16.8	10.2	18.8	15.2	17.0	8.2[a]	13.4[a]
0.004	12.1	20.8	17.6	12.1	20.8	17.6	11.8[a]	20.5	17.2
0.006	12.2	20.8	17.7	12.2	20.8	17.7	12.2	20.8	17.7

[a]The lowest RMSE, indicating the calculated best-fit.

The pore water flux providing the best fit to the field data was not the same for all platforms for a given disturbance depth. In general, the lowest RMSE for Platform 1 was associated with a greater pore water flux than the best-fit scenarios for Platforms 2 and 3. The FFT-water interface sonar surveys detected differential settlement around BML revealing that FFT pore water movement likely varies with location. For example, the FFT-water interface exhibited the greatest elevation change in the northeast corner of BML, where Platform 2 is

located (Figure 4-1). Thus, greater pore water flux was expected at Platform 2 when compared to the other sample locations.

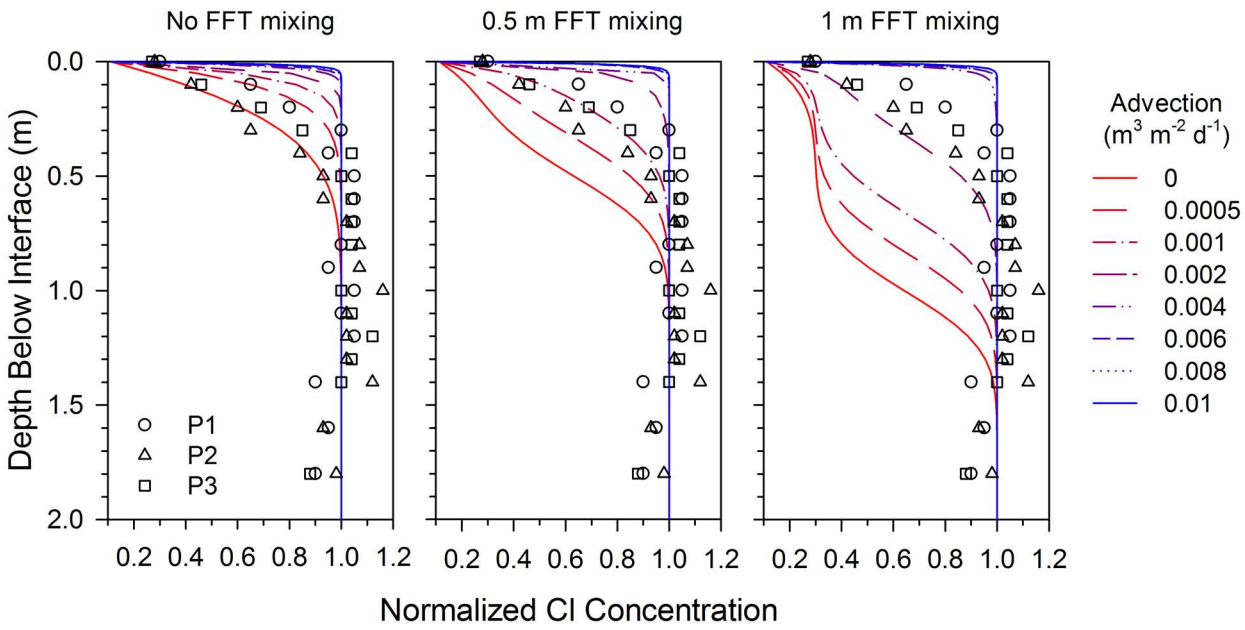

Figure 4-6. Normalized Cl concentrations from the field measurements and simulated advection-dispersion transport regimes with top boundary 1 and three disturbance depths (0, 0.5 m and 1 m) generated for the final sampling date (Aug. 5, 2015).

The FFT-water interface sonar surveys also indicated that a diffusion-only mass transport regime is unlikely given the measured FFT settlement. The modelled scenarios with a 0.5 m or 1 m disturbance generally corresponded to these field observations. Evidence of FFT disturbance was observed in the field as the water cover turbidity exhibited a rapid increase during unstable periods in the lake when the water column was completely mixed (Lawrence et al., 2016). Disturbance within the FFT was also supported by the previous tracer study (Dompierre and Barbour, 2016*a*).

The modelled scenarios were re-run with an alternate top boundary condition (top boundary 2; Figure 4-4) to determine the sensitivity of the simulations to the water cover concentration. This boundary condition was generated in the models using an approximate spline function based on the long-term Cl field measurements. The Cl profiles generated by these modified models

were similar to the original results (Figure 4-6), and did not alter the modelled scenarios providing the best fit to the field data.

Mass flux over the FFT-water interface was determined from the modelled scenarios with advection-dispersion mass transport regimes of 0.004 m^3 m^{-2} d^{-1} or less (Figure 4-7). In the scenarios with no FFT disturbance, the mass flux was fairly constant with time. The mass fluxes generated by the scenarios with disturbances exhibited sharp increases on the days the disturbance was simulated (i.e., October 15, both years). Mass flux from the FFT rapidly decreased afterwards as the concentration within the disturbed depth was equal to the water cover concentration at this time. The mass flux then gradually increased to a rate slightly lower than before the disturbance occurred, due to the decreasing water cover concentration and subsequently lower diffusion rates (Figure 4-4).

The cumulative mass released per square area of FFT between May 2013 and November 2015, was determined based on the simulated mass flux over the FFT-water interface (Figure 4-7). The general trends for cumulative mass release, produced by the models with and without a disturbance event, were fairly similar except for the shift accompanying the disturbance. The total mass released from the FFT with a diffusion-only mass transport regime and no disturbance was very different from the diffusion models with a disturbance; however, when the mass transport regime included a greater advective flux, the relative increase in the total mass released from the FFT was not as large when a disturbance was added to the model.

The simulated Cl released during each mass balance period was determined for comparison purposes. The FFT mass release during Period 2 was substantially less than Period 1 when a disturbance was added to the model (Table 4-4). During Period 1, the simulated Cl release increased with the disturbance depth; however, the mass released during Period 2 did not follow this same trend. As the disturbance increased, the Cl released from the FFT generally decreased in Period 2 for all advection-dispersion transport regimes, likely due to the simulated disturbance dates. The modelled disturbances occurred on October 15, 2013 and October 15, 2014. Consequently, Period 1 included the second simulated disturbance while Period 2 had none.

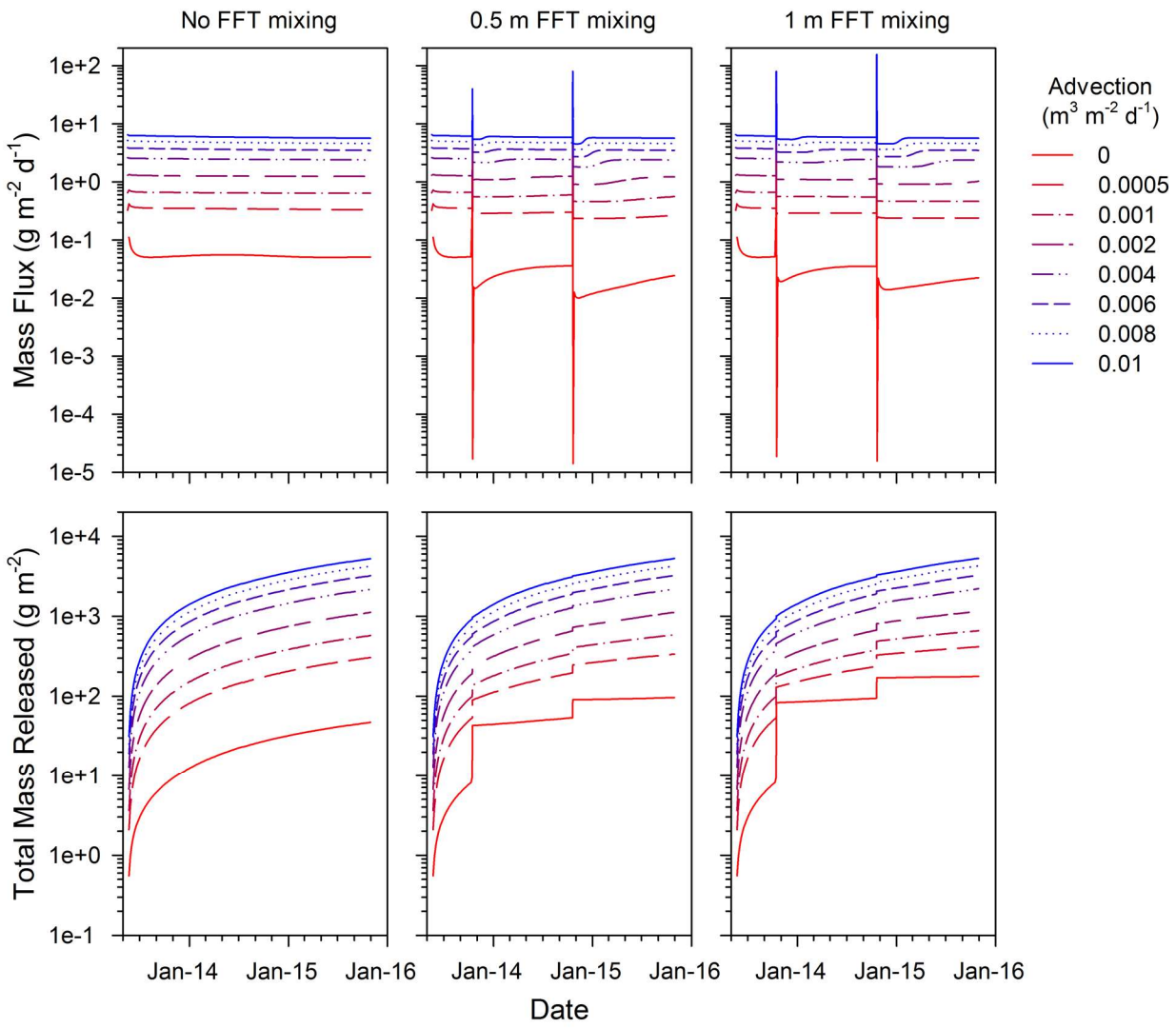

Figure 4-7. Chloride flux rates over the FFT-water interface and cumulative mass released from the FFT starting in May 2013.

The total mass released from the FFT, as determined by the two mass balances (296 g m^{-2} in Period 1 and 277 g m^{-2} in Period 2), was comparable to the simulated mass release over the same periods (Table 4-4). The results from the mass balances correspond to an advection-diffusion regime with a pore water flux between 0.001 and 0.002 m^3 m^{-2} d^{-1}. However, the mass balance sensitivity analysis indicated that the mass released from the FFT could potentially range from 200 to 395 g m^{-2} in Period 1, and 190 to 365 g m^{-2} in Period 2. The simulated pore water flux range associated with these mass flux values is 0.0005 to 0.004 m^3 m^{-2} d^{-1} (Table 4-4).

Table 4-4. Simulated Cl released (g m^{-2}) from the FFT during the two mass balance periods

Advective Flux	No Disturbance			0.5 m Disturbance			1 m Disturbance		
(m^3 m^{-2} d^{-1})	Period 1	Period 2	Total[a]	Period 1	Period 2	Total[a]	Period 1	Period 2	Total[a]
0	20	18	38	47	6	53	87	6	93
0.0005	130	120	250	160	88	240	200	86	280
0.001	230	230	460	270	180	440	310	170	470
0.002	460	450	900	490	380	870	530	340	870
0.004	890	870	1760	930	810	1740	970	750	1720

[a]The mass of Cl released in both Period 1 and Period 2 for each numerical scenario.

4.5 Discussion

The results from both the mass balance calculations and the numerical models confirmed that FFT was the dominant Cl source to the water cover during the study period. The numerical models provided additional insight into the main mechanisms potentially driving this mass release. Comparison of the simulations with the mass balance calculations and field observations indicate that the FFT is likely exhibiting a transient advection-dispersion mass transport regime, due to FFT settlement and shifting concentrations in the water cover over time.

Given an advective-dispersion mass transport regime, the results from the mass balances were also used to determine the FFT pore water flux associated with the calculated mass release. The pore water flux from the FFT, q_z (m^3 m^{-2} a^{-1}), was determined with:

$$M_{pw} = q_z \cdot C + n \cdot D_h \cdot \frac{\Delta C}{\Delta z} \tag{4.5}$$

given the calculated mass release from the FFT during each mass balance year, M_{pw} (300 g m^{-2} a^{-1} in Period 1 and 280 g m^{-2} a^{-1} in Period 2), the average FFT concentration at the FFT-water interface over the given period, C (480 g m^{-3} in Period 1 and 410 g m^{-3} in Period 2), the FFT porosity, n (0.86 m^3 m^{-3}), the hydrodynamic dispersion coefficient, D_h (0.03 m^2 a^{-1}), and the change in concentration with depth measured through the FFT, $\frac{\Delta C}{\Delta z}$ (300 g m^{-4} in Period 1 and 470 g m^{-4} in Period 2). The pore water fluxes determined from the above equation were 0.6 m^3 m^{-2} a^{-1} for Period 1 and 0.7 m^3 m^{-2} a^{-1} for Period 2, which both correspond to an approximate daily pore water flux of 0.002 m^3 m^{-2} d^{-1}. The estimated pore water flux was greater

for Period 2 even though the calculated mass flux from the FFT was less than Period 1. This was likely due to the lower average concentration at the FFT-water interface during this period.

The FFT-water interface sonar surveys revealed that settlement ranged from 0 to 2 m, between October 2013 and October 2015. The area-weighted average settlement was 1.49 m, or 0.75 $m^3\ m^{-2}\ a^{-1}$, assuming equal settlement in both years. This value is similar to the two pore water release rates calculated from the mass balances. Thus, the assumed advection-dispersion mass transport regime and mass balance method predicted a similar pore water release as observed in the field.

In addition to chemical mass transport via advection-dispersion, the results from the numerical models suggested that some form of FFT disturbance might also affect the water cover concentration over time. The simulated Cl profiles indicated a possible advection range, as the best-fit mass flux scenario changed with the simulated disturbance depth and the exact depth of the disturbance remains unknown.

The mass balance method and area-weighted average settlement suggest that the pore water movement through the FFT was approximately 0.002 $m^3\ m^{-2}\ d^{-1}$ over the study period. The numerical models were re-run with this advective flux and varying disturbance depths between 0.5 and 1 m, to evaluate the disturbance depth providing the best-fit to the measured chloride profiles (Table 4-5). At Platform 1, a 0.75 m disturbance provided the best fit, while 0.85 m and 0.95 m disturbances produced the lowest RMSE values for the Cl profiles from Platforms 3 and 2, respectively. Platforms 2 and 3 are closer to the shore, so these locations would likely experience greater impacts from waves, such as internal seiches, within the water cover. These results suggest that the influence of FFT disturbance on the movement of mass over the FFT-water interface likely varies with location at BML.

Overall, these findings are similar to the previous tracer investigation conducted at BML (Dompierre and Barbour, 2016*a*); however, this study demonstrates that multiple methods can be used to assess mass loading to an EPL from underlying FFT, and the mass transport mechanisms within the FFT are changing over time. The original study (Dompierre and Barbour, 2016*a*) found an advective mass transport regime of 0.004 $m^3\ m^{-2}\ d^{-1}$ and a 1.1 m FFT disturbance, while this investigation observed lower values for both advection and disturbance depth. The current study covered a later time period, so the smaller advective flux could be explained by

decreasing FFT settlement rates over time. In addition, disturbance within the FFT will likely decrease as the FFT-water interface elevation declines and the depth of the water cover increases.

Table 4-5. RMSE for simulated disturbance depth range and 0.002 $m^3\ m^{-2}\ d^{-1}$ advection compared to normalized field concentrations (%)

Disturbance	**Location**		
(m)	P1	P2	P3
0.5	10.2	18.8	15.2
0.55	9.6	18.1	14.5
0.6	8.9	17.1	13.4
0.65	8.1	15.9	12.1
0.7	7.4	14.3	10.6
0.75	7.3	12.6	9.1
0.8	8.0	10.8	8.0
0.85	9.5	9.1	7.7
0.9	11.6	7.8	8.7
0.95	14.2	7.4	10.7
1.0	32.4	15.7	31.2

4.6 Conclusions

The FFT in BML is undergoing self-weight consolidation causing substantial pore water and chemical mass loading to the overlying water cover, as confirmed by both the mass balance and numerical methods used in this study. The estimated Cl mass release from the FFT (average of 287 $g\ m^{-2}\ a^{-1}$) was substantially larger than other mass sources (Table 4-1). However, the advection-dispersion mass transport regime through the FFT will change over time, as FFT settlement by self-weight consolidation is anticipated to gradually decrease.

The multiple methods employed in this study allowed for a comprehensive consideration of mass transport over the FFT-water interface. Together, the mass balances and numerical models confirmed an advection-dispersion mass transport regime through the FFT with a seasonal disturbance ranging from 0.8 to 0.95 m at the three sample locations. The numerical simulations also provided insight on the overall effect of these disturbances on the mass loading to the water cover. Although the disturbance caused a sharp increase in mass flux over the FFT-water interface, its overall influence on the predicted cumulative mass release was relatively small,

given an advection-dispersion mass transport regime. This study demonstrated the benefit of using multiple methods for assessing mass transport.

The results from the chemical mass balance highlighted the importance of operational controls on the geochemical regime within an EPL. Pumping rates (in and out) were observed to largely control the water balance. These rates will determine the water cover volume, which based on the sensitivity analysis, was an important parameter in the mass balance calculations. Future anthropogenic changes may also affect BML. For example, the BML watershed is expected to increase as more surrounding land is reclaimed. The runoff water coming from this larger watershed may have a higher dissolved solids content than those observed in this study, causing runoff to be a more significant contributor to mass in the future. Thus, future EPL design must consider the movement of water and mass through the greater reclamation landscape.

The results from this study provide an initial assessment of the geochemical regime in the BML cover, which can be used as a baseline for future studies and will assist in the development of monitoring plans at this study site. This investigation also highlights essential considerations for future EPL design, such as self-weight consolidation rates, field conditions, operational controls, and surrounding reclamation activities, as these will affect the water and chemical balances in the water cover over time. The FFT contributed substantial mass to the water cover over the monitored periods revealing the importance of studying the geochemical characteristics of any waste material placed in an EPL or similar reclamation feature. Finally, this study highlights the need for large-scale reclamation design considering water and mass movement throughout the entire reclaimed landscape, particularly in regions like the AOSR where large areas of land have been disturbed.

CHAPTER 5 – SUMMARY AND RECOMMENDATIONS

As a whole, this thesis provides fundamental insight on the movement of heat (Chapters 2 and 3) and mass (Chapters 3 and 4) through FFT in the first EPL. Each manuscript employed multiple methods to answer the associated research questions, allowing for greater confidence in the presented results. Together the three manuscripts fulfilled all proposed objectives and developed a better understanding of: (1) the thermal conductivity and volumetric heat capacity of FFT; (2) the dominant mechanisms for heat transport within the FFT; (3) the characteristics of FFT settlement in BML; (4) the importance of other mass transport mechanisms over the FFT-water interface; and (5) the total mass contributed from the FFT to the BML water cover during its initial years as an EPL.

In addition to these original objectives, a better understanding of FFT properties was reached through the study program. For example, the typical range in FFT solids and bitumen contents and their general trends with depth in BML, and FFT dynamic viscosity and yield stress near the FFT-water interface, are now known. This study also led to the development of a new system for testing in-situ FFT properties. The system requires modification for future thermal properties analysis; however, its overall design can be used for other field experimentation or monitoring programs. Finally, the numerical models developed for heat and conservative mass transport can be used as a reference for further numerical analyses. A summary of the findings associated with this thesis and recommendations for future studies are provided below.

5.1 Review of Mass Transport Mechanisms

A conceptual model was developed to highlight the relative mass contributions to BML during the studied period (Figure 5-1). The FFT was the most significant Cl mass source to the water cover, confirming the need to assess mass transport mechanisms at the FFT-water interface.

5.1.1 Advection via FFT Settlement

The mass and heat transport via pore water flow observed at multiple locations around BML were comparable to FFT settlement measured by sonar surveys of the FFT-water interface,

and suggested that settlement is well distributed over the FFT surface. The release rate predicted by the second manuscript was 1.46 m/a, which was slightly higher than the amount of FFT settlement predicted by the BML consolidation model (Carrier et al., 2007). However, sonar surveys of the FFT-water interface over the modelled period (October 2013 and April 2014), found that the average FFT-water interface elevation dropped from 301.6 masl to 300.9 masl. These field measurements correspond to an average yearly pore water release rate of 1.6 m/a, suggesting that the original consolidation model underestimated FFT settlement rates during these initial years.

The pore water flux rates estimated from the Cl profiles in the third manuscript were generally between 0.18 and 1.46 m/a. The chloride loading obtained from the lake mass balance resulted in pore water fluxes of 0.37 to 0.73 m/a assuming an advection-dispersion regime within the upper FFT; however, the sensitivity analyses suggested that the pore water flux could range from 0.18 to 1.46 m/a. This is a similar flux range as estimated by the Cl transport models, but is slightly lower than those estimated from the temperature and isotope profiles and models. The lower flux rates were expected, as the Cl profiles were evaluated more than a year after the stable isotope and temperature profiles, and self-weight consolidation decreases exponentially over time. Overall, these results confirmed that advection is an important mechanism for mass transport within BML; however, advection rates will change over time as FFT settlement declines.

5.1.2 Enhanced Advection Mechanisms

An episodic disturbance was necessary to replicate the observed tracer profiles with the transport models from both the second and third manuscripts. For example, the transition zone from the deep FFT pore water to the lake water concentrations was found to be approximately 0.4 m for both stable isotopes of water and chloride samples. When the numerical models were compared to these field results, the advection-dominant regimes expected based on field settlement rates produced much smaller transition zones of less than 0.1 m for the isotope models and 0.3 m for the chloride models. The simulated transition zone increased when a disturbance was added to the model, providing a better fit to the field observations.

The potential for FFT erosion was confirmed by yield stress laboratory analysis of low solids content FFT, which corresponded to the top 0.3 m of FFT. Previous studies found the critical shear stress of soft tailings to be approximately 0.2 Pa, which is less than the critical shear

stress of natural sediments (Mian and Yanful, 2007; Yanful and Catalan, 2002). This provides a potential explanation for why the measured yield stresses were more similar to the lower limit of estimated yield stress with depth, based on literature obtained values for fluid muds (after McAnally et al., 2007; Figure 2-6). Thus, the top 0.2 m of FFT is likely below the critical shear stress associated with other soft tailings (Mian and Yanful, 2007; Yanful and Catalan, 2002). This depth is not as large as the disturbance events included in the numerical models but does suggest that erosion of the FFT-water interface is possible.

Lawrence et al. (2016) studied mixing mechanisms within the BML water cover and the potential for these mechanisms to cause FFT resuspension. They determined that the orbital velocities produced by typical wind speeds measured at the site would not generate velocities at the FFT-water interface large enough to disturb the FFT. However, they did list numerous other mixing mechanisms that could be present in BML. In particular, Lawrence et al. (2016) noted that currents or turbulence associated with internal seiches and smaller scale internal waves may cause erosion of the FFT-water interface.

Lawrence et al. (2016) also proposed the presence of an intermediate, turbid layer that would remain at the bottom of the water cover during calm periods but would be easily disturbed by wind events. Characteristics of this intermediate layer are not well understood; however, its depth is expected to vary spatially around BML given variation in the FFT-water interface elevation, which ranges in elevation by up to 4 m. This intermediate layer could have been included in field measurements believed to be collected below the FFT-water interface. Therefore, this proposed intermediate layer could be the region of the disturbance that was observed within the FFT.

Another form of enhanced advection potentially present within the BML system is ebullition. Bubble migration has been found to strip volatile pollutants from sediments (Yuan et al., 2007) through sorption of hydrophobic (organic) contaminants to bubble surfaces (McLinn and Stolzenburg, 2009). Therefore, the bubble migration through FFT in BML is likely associated with the release of organic constituents to the water cap. As the mass transport studies used conservative, non-organic tracers, these would not have been directly affected by ebullition within the FFT. However, methanogenesis, in addition to causing ebullition, may also lead to exchange reactions at the clay mineral surfaces, decreasing the electrical double layer and promoting settlement of the FFT (Dompierre et al., 2016). Thus, methanogenesis would increase

advective mass transport due to FFT settlement and affect the movement of chloride and stable isotopes of water.

Ebullition may also carry suspended solids into the intermediate, turbid layer, increasing the potential for solids release to the water cap (Lawrence et al., 2016). This upward movement of gas and solids may also destabilize the FFT-water interface contributing to the potential for disturbance within the FFT (Lawrence et al., 2016). Thus, ebullition enhances both advection due to FFT settlement and disturbance due to tailings destabilization near the FFT-water interface.

5.1.3 Diffusion

The stable isotope of water, temperature, and chloride profiles within the upper FFT were typical of diffusive mass transport as they exhibited a smooth transition from the water cover concentration to that of the FFT pore water. Diffusion occurred as a result of this observed difference in water cover and FFT pore water characteristics. In the initial EPL stages, advective pore water movement limits the diffusion depth – also referred to as the transition zone – within the FFT. However, as predicted by self-weight consolidation theory, FFT settlement and the corresponding advective mass flux will decrease over time. As advection decreases, diffusive mass transfer will become increasingly important to the mass transport regime within the EPL. At this stage, mass released from the FFT will depend on the concentration of the water cover. If the water cover concentration changes substantially over time, diffusion will also vary. However, if the water cover concentration remains fairly consistent, diffusive mass transport may reach a steady-state, with relatively constant mass release from the FFT.

The relative contribution of FFT to mass stored in the BML water cover will change with time given the declining advection rates and lower mass flux rates associated with diffusion. Though the other mass sources (precipitation, pump-in water, and runoff) were not significant for the water cover mass balance in the early years of EPL development, these inputs must be considered in the future (Figure 5-1).

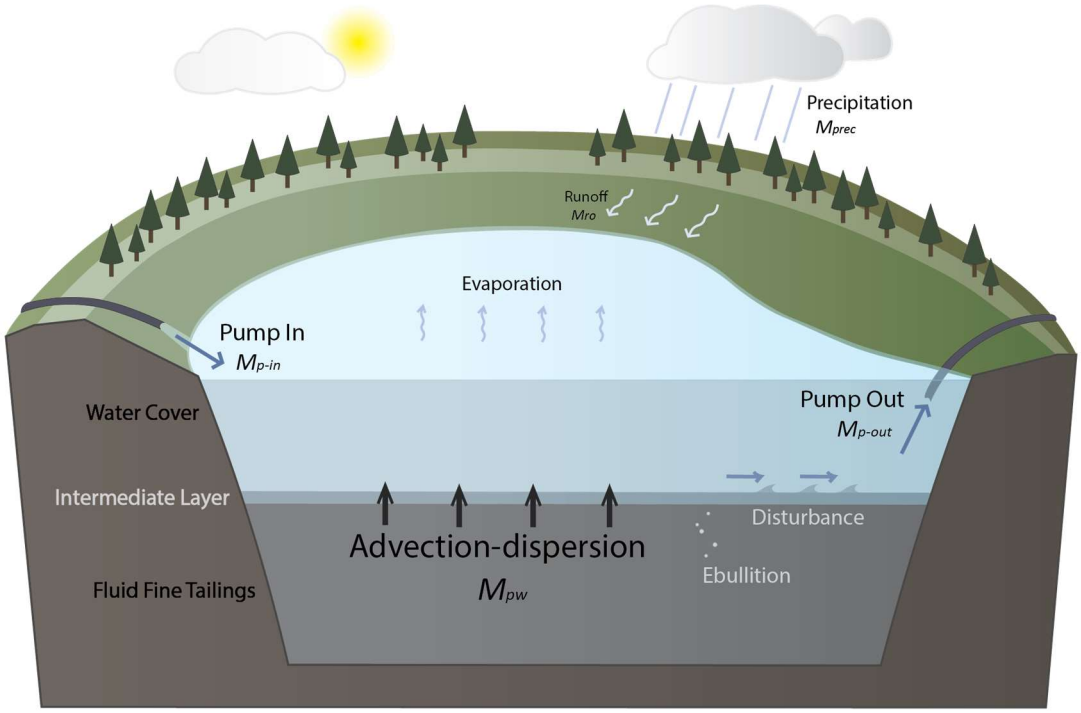

(a) EPL in the early years

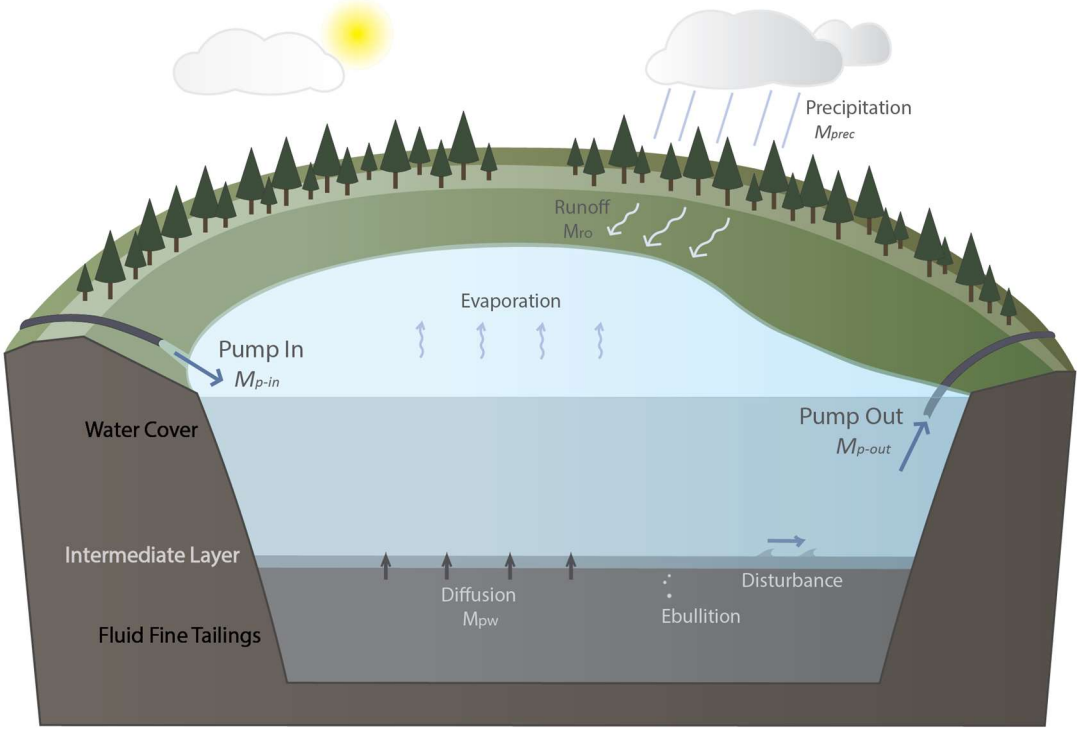

(b) EPL in the medium to long-term

Figure 5-1. Conceptual model of mass inputs and outputs for BML (a) during the studied years and (b) predicted in the future. Mechanisms and properties requiring further study are labeled with light text while confirmed mass sources are in black.

5.2 Review of Heat Transport Mechanisms

The thermal regime within the FFT was driven by the same mechanisms as the mass transport regime. As with the conservative mass tracers, temperatures through the FFT suggested that forced convection was an important mechanism for heat transport within the FFT. Conductive heat transport was evident based on the seasonal temperature variation measured through the FFT, reaching a maximum depth of 5 m. As the pore water flux associated with settlement decreases over time, the maximum and minimum FFT temperatures will likely reach greater depths as illustrated by the greater size of the temperature envelope when the simulated convective heat transfer decreased. Free convection within the FFT was determined to be unlikely, as the density differences produced by the inverted temperature profiles were associated with low Rayleigh numbers (<1).

Ebullition could affect the temperatures measured in BML. Bubbles moving through the FFT likely travel at faster rates that the pore water flux associated with tailings settlement, and they could carry energy associated with the deeper FFT upwards. Dompierre et al. (2016) found that methanogenesis is likely occurring within the top 10 m of FFT, based on the lower pH values observed in this region. As the field measurements illustrated, seasonal temperatures within the lake water affected temperatures within the top 5 m of FFT. Therefore, cooler temperatures during the fall and winter may lead to lower methanogenesis rates and less bubble release within the top 5 m of FFT.

Ebullition could cause the temperature profiles to shift towards a greater apparent advective mass transport regime in the summer months. Meanwhile during the winter months, decreased ebullition rates would have a reduced effect on the temperatures measured through the FFT. This would cause the seasonal temperature envelope to appear asymmetric. The asymmetry observed in the FFT temperature profiles was assumed to be due to the length of the collection period, which only covered half of the year. However, ebullition may have contributed to the observed asymmetry. Also, fluctuating ebullition rates could have caused the discrepancy in the simulated best-fit heat transport regimes for the maximum and minimum temperature profiles when no disturbance was included in the models. Temperature measurements through the FFT should be collected for a complete year to confirm the effect of ebullition on seasonal FFT temperatures.

Ultimately, energy movement through the FFT is controlled by the thermal properties associated with these tailings. Previous equations for the thermal properties of saturated porous

media (Cosenza et al., 2003; De Vries, 1963) were used as a theoretical basis for assessing the FFT thermal properties. Modification of these equations to include a bitumen term generated theoretical values that were similar to those measured in the laboratory. The thermal conductivity of the FFT in BML is expected to be approximately 0.57 W/m/K near the FFT-water interface, as this represents FFT with a high volumetric water content and bitumen present. Fluid fine tailings near the deposit bottom are expected to have a thermal conductivity of 0.93 W/m/K. Volumetric heat capacity is expected to decrease with depth from 4.2 $x10^6$ $J/m^3/K$ near the FFT-water interface to 3.2 $x10^6$ $J/m^3/K$ near the deposit bottom. These general trends correspond to the changing FFT solids content with depth; however, inconsistent bitumen contents with depth likely cause thermal conductivity to vary by approximately 0.1 W/m/K and volumetric heat capacity to vary by 0.4 $x10^6$ $J/m^3/K$ from these general trends.

Unfortunately, in-situ thermal properties testing did not provide as much insight as expected due to issues with shifting radius during installation and potential densification of the FFT immediately surrounding the system. The initial estimates for the FFT thermal conductivity in BML appeared to be similar to the laboratory results; however, future testing is necessary to confirm these results and evaluate the FFT volumetric heat capacity.

Given the average FFT temperature and the observed 2014 and 2015 pore water release rates, a simple calculation was completed to estimate the ratio of thermal energy released from the tailings to the energy stored within the BML water cover. The average temperature measured through the FFT (Figure 2-9) was approximately 10 °C or 283.15 K, and pore water release rates between 0.35 to 0.85 m a^{-1} were predicted for these years, over an approximate area of 6.4 $x10^6$ m^2. The average energy stored in the water cover can be calculated with the average water cover temperature (10 °C or 283.15 K) and volume (6.0 $x10^7$ m^3). Given this information, the ratio of energy from the released FFT pore water to the thermal energy of the water cover was predicated to be between 5 % and 10 %. Therefore, heat transport from the FFT could potentially carry substantial energy into the water cap. Future consideration of FFT energy release and consequences to the thermal regime within the water cover is necessary.

5.3 Recommendations

The mass balance portion of this study highlighted the importance in assessing mass transport from the FFT, as it was the greatest mass source to BML over the two measured

periods. Further study will be necessary to determine decreasing FFT settlement rates and the associated change in advection. Sonar surveys of the FFT-water interface have been previously used to monitor settlement at regular intervals. The tracer studies confirmed that the mass transport mechanisms within the FFT were comparable to the measured settlement rates so continued sonar surveys would be an acceptable approach to evaluating future FFT settlement.

All three tracers indicated that the top portion of FFT undergoes some form of disturbance; however, further study is required to fully characterize this disturbance. A field investigation of the horizontal fluid velocities above and below the FFT-water interface, particularly during spring and fall turnover, would provide critical information on the potential for waves within the water cover to affect FFT. Also, detailed tracer profiles collected over the FFT-water interface before and after unstable periods could verify the disturbance mechanism, assuming that the disturbance is episodic. These results can be compared to those discussed in the second and third manuscripts by using a stable isotope of water or Cl as the monitored tracer.

The influence of an intermediate layer on the observed disturbance should also be investigated. Field sampling during very calm periods could be completed to capture and characterize the intermediate layer. The mass transport simulations could be modified to incorporate an intermediate layer by including a region at the top of the modelled domain with a greater water content and higher diffusion coefficient. This intermediate layer could undergo disturbance events similar to the original models by further increasing its diffusion coefficient during instable periods.

Ebullition has been observed to promote FFT settlement and may potentially cause destabilization of the FFT-water interface. Ebullition may also influence the movement of energy through the FFT, as higher ebullition rates during warm months could augment heat transfer from the FFT to the water cover. Future evaluations of mass transport through the FFT should measure in-situ ebullition rates, estimate the remaining reactants available for methanogenesis, and predict long-term bubble production within the FFT in BML.

The results presented in this thesis provide the dominant mass transport mechanisms for conservative species; however, there are many constituents of interest in the FFT that are not conservative, such as naphthenic acids. Thus, the logical next step is to expand the numerical models to include reactive mass transport. The preliminary FFT pore water characteristics presented by Dompierre et al. (2016), subsequent high-resolution sampling over the FFT-water

interface at BML, and the physical mass transport models described in this thesis provide a strong basis for reactive transport work.

Given the issues encountered during in-situ thermal properties testing, further research is required to assess the effect of scale and gas bubbles on the FFT thermal conductivity and volumetric heat capacity. Future in-situ testing systems must be designed to limit the potential for FFT disturbance during installation. The rope supporting the system should be replaced with a material that will not allow wicking and FFT densification. Improvements to the in-situ testing system should also include spacers between the heating wire and thermistor string to ensure that the heating radius is known and remains constant throughout installation and testing. The thermal properties of the spacer material should be defined so that the numerical models can account for this addition.

The FFT heat transport modelling was conducted over a relatively short time. This model can be expanded to cover a longer period, for example, to consider heat released from the FFT over an entire year or multiple years during the EPL development phase. Information on heat transport over the FFT-water interface can be used to assess the energy balance in the water cover. The thermal regime within the BML water cover will be critical to the development of biotic activity and the hydrological performance of the lake, as it influences evaporation rates and ice cover duration. Preliminary estimates illustrate the importance of heat transfer from the FFT on the energy stored in the BML water cover.

5.4 Final Thoughts

Studies at conventional pit lakes indicated that multiple factors influence their geochemical characteristics. The results presented above reveal that the most significant factor at BML is the presence, depth, and properties of FFT. The tailings were by far the largest Cl mass source to the water cover (99 %) in the first 3 years of operation. The tailings volume in BML is substantially larger than the water cover volume. When BML was commissioned, the water cover was only 13 % of the total tailings volume. Based on these findings, future EPL design should consider the optimal water cover to tailings volume ratio that would result in the greatest water quality while providing storage for FFT. This ratio will also be important for the thermal regime within the water cover.

The BML water cover properties were not as important as the FFT characteristics and depth, but would have had an effect on FFT disturbance. The large water cover surface area, and resulting fetch lengths, allows greater fluid velocities to develop. The relatively small water cover depth would increase the probability of FFT disturbance given these fluid velocities. The water cover concentration is not as significant during these early years as it will be in the future when the dominant mass transport mechanism from the FFT is diffusion.

Human-controlled factors – including pumping water into and out of BML – were also important to BML water quality. Water pumped from BML was the dominant means for removing mass from the system. Changes to pumping volumes would have a substantial effect on the water cover mass balance. Thus, human factors cannot be overlooked when considering the geochemical conditions within an EPL.

These findings illustrate that initial EPL design is critical to the thermal and geochemical conditions present within the water cover. Oil sands operators are more likely to meet regulatory requirements by taking time to consider the shape and size of the EPL water cover, volume and characteristics of stored materials, and capacity to pump freshwater into and out of the pit. The presented manuscripts provide a foundation for future research at BML and the Demonstration Pit Lakes Project (COSIA, 2012*b*); however continued monitoring and study are necessary to fully characterize interactions between the FFT and water cover, particularly the major biogeochemical processes occurring within both of these domains.

REFERENCES

Abu-Hamdeh, N.H. and Reeder, R.C. 2000. Soil thermal conductivity: Effects of density, moisture, salt concentration, and organic matter. Soil Science Society of America Journal, 64(4): 1285-1290.

Abu-Hejleh, A.N. and Znidarčić, D. 1995. Desiccation theory for soft cohesive soils. Journal of Geotechnical Engineering, 121(6): 493-502.

Adu-Wusu, C., Yanful, E.K. and Mian, M. 2001. Field evidence of resuspension in a mine tailings pond. Canadian Geotechnical Journal, 38(4): 796-808.

Alberta Energy Regulator 2015. ST98-2015: Alberta's energy reserves 2014 and supply/demand outlook 2015-2024. Alberta Energy Regulator, ISSN 1910-4235, Calgary, AB, Canada.

Allen, E.W. 2008. Process water treatment in Canada's oil sands industry: I. Target pollutants and treatment objectives. Journal of Environmental Engineering Science, 7(2): 123-138.

Anderson, M.P. 2005. Heat as a ground water tracer. Ground Water, 43(6): 951-968.

Assael, M.J., Millat, J., Vesovic, V. and Wakeham, W.A. 1990. The thermal conductivity of methane and tetrafluoromethane in the limit of zero density. Journal of Physical and Chemical Reference Data, 19(5): 1137-1147.

ASTM. 2015*a*. D4052-15: Standard test method for density, relative density, and API gravity of liquids by digital density meter. ASTM International, West Conshohocken, PA, USA. DOI: 10.1520/D4052-15.

ASTM. 2015*b*. D4464-15: Standard test method for particle size distribution of catalytic materials by laser light scattering. ASTM International, West Conshohocken, PA, USA. DOI: 10.1520/D4464-15.

ASTM. 2015*c*. D5002-15: Standard test method for density and relative density of crude oils by digital density analyzer [online]. ASTM International, West Conshohocken, PA, USA. doi: 10.1520/D5002-15.

ASTM. 2014*a*. C1070-01(2014): Standard test method for determining particle size distribution of alumina or quartz by laser light scattering. ASTM International, West Conshohocken, PA, USA. DOI: 10.1520/C1070.

ASTM. 2014*b*. D854-14: Standard test methods for specific gravity of soil solids by water pycnometer. ASTM International, West Conshohocken, PA, USA. DOI: 10.1520/D0854-14.

ASTM. 2014*c*. D5334-14: Standard test method for determination of thermal conductivity of soil and soft rock by thermal needle probe procedure. ASTM International, West Conshohocken, PA, USA. DOI: 10.1520/D5334-0814.

Aubinet, M., Vesala, T. and Papale, D. 2012. Eddy covariance: a practical guide to measurement and data analysis. Springer Science & Business Media, New York, NY, USA.

Baer, T. 2014. An evaluation of the use of natural stable isotopes of water to track water movement through oil sands mine closure landforms. M.Sc. Thesis, Civil Engineering, University of Saskatchewan, Saskatoon, SK, Canada.

Baer, T. and Barbour, S.L. 2013. An evaluation of the use of stable water isotopes to characterize and track water through oil sands mine closure landforms. 66th Canadian Geotechnical Conference, Sep. 29 – Oct. 3, 2013, Montreal, QC, Canada.

Baer, T., Barbour, S.L. and Gibson, J.J. 2016. The stable isotopes of site wide waters at an oil sands mine in northern Alberta, Canada. Journal of Hydrology, In Press: http://dx.doi.org/10.1016/j.jhydrol.2016.08.017.

Balistrieri, L.S., Tempel, R.N., Stillings, L.L. and Shevenell, L.A. 2006. Modeling spatial and temporal variations in temperature and salinity during stratification and overturn in Dexter Pit Lake, Tuscarora, Nevada, USA. Applied Geochemistry, 21: 1184-1203.

Barbour, S.L., Hendry, M.J. and Wassenaar, L.I. 2012. In situ experiment to determine advective-diffusive controls on solute transport in a clay-rich aquitard. Journal of Contaminant Hydrology, 131(1-4): 79-88.

Bear, J. 1972. Dynamics of Fluids in Porous Media. Dover Publications, Inc., New York, NY, USA, p. 654.

Been, K. and Sills, G.C. 1981. Self-weight consolidation of soft soils: an experimental and theoretical study. Géotechnique 31(4): 519-535.

Bennacer, R. and Lakhal, A. 2005. Numerical and analytical analysis of thermosolutal convection in an annular field: Effect of thermodiffusion. In: Ingham, D.B. and Pop, I. (Eds.), Transport Phenomena in Porous Media III, Elsevier Science Ltd., Oxford, UK, 341-365.

Bertoldi, C., Dachs, E. and Appel, P. 2007. Heat-pulse calorimetry measurements on natural chlorite-group minerals. American Mineralogist, 92(4): 553-559.

BGC Engineering Inc. 2010. Review of reclamation options for oil sands tailings substrates. Oil Sands Research and Information Network, University of Alberta School of Energy and the Environment, Edmonton, AB. OSRIN Report No. TR-2.

Blanken, P.D., Rouse, W.R., Culf, A.D., Spence, C., Boudreau, L.D., Jasper, J.N., Kochtubajda, B., Schertzer, W.M., Marsh, P. and Verseghy, D. 2000. Eddy covariance measurements of evaporation from Great Slave Lake, Northwest Territories, Canada. Water Resources Research, 36(4): 1069-1077.

Blasch, K., Constantz, J. and Stonestrom, D.A. 2007. Thermal methods for investigation ground-water recharge. U.S. Geological Survey Professional Paper, 1703, 353-376.

Boudreau, B.P. 1996. The diffusive tortuosity of fine-grained unlithified sediments. Geochimica et Cosmochimica Acta, 60(16): 3139-3142.

Bredehoeft, J.D. and Papadopulos, I.S. 1965. Rates of vertical groundwater movement estimated from the earth's thermal profile. Water Resources Research, 1(2): 325-328.Bristow, K.L. 1998. Measurement of thermal properties and water content of unsaturated sandy soil using dual-probe heat-pulse probes. Agricultural and Forest Meteorology, 89(2): 75-84.

Bristow, K.L., White, R.D. and Kluitenberg, G.J. 1994. Comparison of single and dual-probes for measuring soil thermal properties with transient heating. Australian Journal of Soil Research, 32(3): 447-464.

Buttle, J.M. 1998. Fundamentals in small catchment hydrology. In: Kendall, C. and McDonnell, J.J. (Eds.), Isotope Tracers in Catchment Hydrology, Elsevier Science Ltd., Amsterdam, The Netherlands, 1-49.

Caldwell, D.R. 1974. Thermal conductivity of sea water. Deep-Sea Research, 21(2): 131-137.

Carey, S.K. 2008. Growing season energy and water exchange from an oil sands overburden reclamation soil cover, Fort McMurray, Alberta, Canada. Hydrological Processes, 22(15): 2847-2857.

Carrier, D., Shaw, B. and Lee, J. 2007. Syncrude West in Pit (WIP) 1995 to 2006: Consolidation modelling summary. Syncrude Canada Ltd., Internal Report.

Castendyk, D.N. and Webster-Brown, J.G. 2007. Sensitivity analysis in pit lake prediction, Martha mine, New Zealand 1: Relationship between turnover and input water density. Chemical Geology, 244: 42-55.

Castro, J.M. and Moore, J.N. 2000. Pit lakes: their characteristics and the potential for their remediation. Environmental Geology, 39: 1254-1260.

Catalan, L.J.J. and Yanful, E. K. 2002. Sediment-trap measurements of suspended mine tailings in shallow water cover. Journal of Environmental Engineering, 128(1): 19-30.

Caughill, D.L., Morgenstern, N.R. and Scott, J.D. 1993. Geotechnics of nonsegregating oil sand tailings. Canadian Geotechnical Journal, 30(5): 801-811.

CEMA (Cumulative Environmental Management Association). 2012. End pit lakes guidance document [online]. Cumulative Environmental Management Association Reclamation Working Group. Available at: www.cemaonline.ca Accessed: May 28, 2016.

Cervantes-Espinosa, L.M., Castillo-Alvarado, F.L., Lara-Hernández, G., Cruz-Orea, A., Medoza-Alvarez, J.G., Valcárcel, J.P. and García-Quiroz, A. 2012. Thermal characterization, using the photopyroelectric technique, of liquids used in the automobile industry. International Journal of Thermophysics, 33(10): 1916-1923.

Chalaturnyk, R.J., Scott, J.D. and Özüm, B. 2002. Management of oil sands tailings. Petroleum Science and Technology, 20(9-10): 1025-1046.

Chapuis, R.P. 2012. Predicting the saturated hydraulic conductivity of soils: a review. Bulletin of Engineering Geology and the Environment, 71(3): 401-434.

Chen, M., Walshe, G., Chi Fru, E., Ciborowski, J.J.H. and Weisener, C.G. 2013. Microcosm assessment of the biogeochemical development of sulfur and oxygen in oil sands fluid fine tailings. Applied Geochemistry, 37: 1-11.

Constantz, J. 2008. Heat as a tracer to determine streambed water exchanges. Water Resources Research, 44(4), W00D10, DOI: 10.1029/2008WR006996.

Coplen, T.B., Herczeg, A.L. and Barnes, C. 2000. Isotope engineering – using stable isotopes of the water molecule to solve practical problems. In: Cook, P. and Herczeg, A.L. (Eds.), Environmental Tracers in Subsurface Hydrology, Kluwer Academic Publishers, Norwell, MA, USA.

Cosenza, P., Guérin, R. and Tabbagh, A. 2003. Relationship between thermal conductivity and water content of soils using numerical modelling. European Journal of Soil Science, 54(3): 581-587.

COSIA (Canada's Oil Sands Innovation Alliance Inc.) 2012*a*. Focus areas: Tailings [online]. Available at: http://www.cosia.ca [accessed 6 Jul 2016].

COSIA 2012*b*. Pit Lake Research [online]. Available at: http://www.cosia.ca/pit-lake-research [accessed 23 Aug 2016].

COSIA 2012*c*. Technical guide for fluid fine tailings management [online]. Available at: http://www.cosia.ca/initiatives/project-research [accessed 27 Jul 2016].

Côté, J. and Konrad, J.-M. 2009. Assessment of structure effects on the thermal conductivity of two-phase porous geomaterials. International Journal of Heat and Mass Transfer, 52(3-4): 796-804.

Côté, J. and Konrad, J.-M. 2005. Thermal conductivity of base-course materials. Canadian Geotechnical Journal, 42(1): 61-78.

Cox, M.H., Su, G.W. and Constantz, J. 2007. Heat, chloride, and specific conductance as ground water tracers near streams. Ground Water, 45(2): 187-195.

Cussler, E.L. 1997. Diffusion – Mass transfer in fluid systems (2nd ed.). Cambridge University Press, Cambridge, United Kingdom.

Davis, S.N., Thompson, G.M., Bentley, H.W. and Stiles, G. 1980. Ground-water tracers – A short review. Ground Water, 18(1): 14-23.

De Vries, D.A. 1963. Thermal properties of soils. In: W.R. van Wijk (Ed.), Physics of Plant Environment, North Holland Publishing, Amsterdam, The Netherlands, pp. 210-235.

De Vries, D.A. 1958. Simultaneous transfer of heat and moisture in porous media. Transactions, American Geophysical Union, 39(5): 909-916.

Dean, E.W. and Stark, D.D. 1920. A convenient method for the determination of water in petroleum and other organic emulsions. Journal of Industrial and Engineering Chemistry, 12(5): 486-490.

DeLapp, R.C., LeBoeuf, E.J. and Bell, K.D. 2004. Thermodynamic properties of several soil- and sediment-derived natural organic materials. Chemosphere, 54(4): 527-539.

Denimal, S., Bertrand, C., Mudry, J., Paquette, Y., Hochart, M. and Steinmann, M. 2005. Evolution of the aqueous geochemistry of mine pit lakes – Blanzy-Montceau-les-Mines coal basin (Massif Central, France): Origin of sulfate contents; effects of stratification on water quality. Applied Geochemistry, 20: 825-839.

Diersch, H.-J.G. and Kolditz, O. 2002. Variable-density flow and transport in porous media: Approaches and challenges. Advances in Water Resources, 25(8-12): 899-944.

Dimitrova, R.S., and Yanful, E.K. 2012. Factors affecting the shear strength of min tailings/clay mixtures with varying clay content and clay mineralogy. Engineering Geology, 125: 11-25.

Domenico, P.A. and Schwartz, F.W. 1998. Physical and chemical hydrogeology (2nd ed.). John Wiley & Sons, Inc., New York, NY, USA.

Dompierre, K.A., and Barbour, S.L. 2016*a*. Characterization of physical mass transport through oil sands fluid fine tailings in an end pit lake: a multi-tracer study. Journal of Contaminant Hydrology, 189: 12-26.

Dompierre, K.A., and Barbour, S.L. 2016*b*. Thermal properties of oil sands fluid fine tailings: Laboratory and in-situ testing methods. Canadian Geotechnical Journal, In Press, DOI: 10.1139/cgj-2016-0235..

Dompierre, K.A., and Barbour, S.L. 2015. Evaluation of thermal properties of oil sand fluid fine tailings. In: 68th Canadian Geotechnical Conference, Quebec City, QC, Canada, 20 – 23 September 2015. Canadian Geotechnical Society, Richmond, BC, Canada.

Dompierre, K.A., Barbour, S.L. and Halferdahl, G.M. 2014. Characterisation of the thermal regime through oil sands fluid fine tailings in an end pit lake. In: 67th Canadian Geotechnical Conference, Regina, SK, Canada, 28 September – 1 October 2014. Canadian Geotechnical Society, Richmond, BC, Canada.

Dompierre, K. A., Lindsay, M. B. J., Cruz-Hernández, P. and Halferdahl, G. M. 2016. Initial geochemical characteristics of fluid fine tailings in an oil sands end pit lake. Science of the Total Environment, 556: 157-177.

Easteal, A.J., Edge, A.V.J., and Woolf, L.A. 1984. Isotope effects in water. Tracer diffusion coefficients for $H_2{}^{18}O$ in ordinary water. The Journal of Physical Chemistry, 88(24): 6060-6063.

Elam, S.K., Tokura, I., Saito, K. and Altenkirch, R.A. 1989. Thermal conductivity of crude oils. Experimental Thermal and Fluid Science, 2(1): 1-6.

Elder, J.W. 1967. Steady free convection in a porous medium heated from below. Journal of Fluid Mechanics, 27(1): 29-48.

Environment Canada, 2015. Canadian Climate Data [Online]. Available at: http://climate.weather.gc.ca. Accessed: January 10, 2016.

Farouki, O.T. 1981. Thermal properties of soils. CRREL Monograph 81-1. United States Army Corps of Engineers, Cold Regions Research and Engineering Laboratory, Hanouver, NH, USA.

Fedorak, P.M., Coy, D.L., Dudas, M.J., Simpson, M.J., Renneberg, A.J. and MacKinnon, M.D. 2003. Microbially-mediated fugitive gas production from oil sands tailings and increased tailings densification rates. Journal of Environmental Engineering and Science, 2(3): 199-211.

Fendinger, N.J., Adams, D.D. and Glotfelty, D.E. 1992. The role of gas ebullition in the transport of organic contaminants from sediments. The Science of the Total Environment, 112(2-3): 189-201.

Ferguson, H.L., O'Neill, A.D.J. and Cork, H.F. 1970. Mean evaporation over Canada. Water Resources Research, 6(6): 1618-1633.

Feth, J. H. 1981. Chloride in natural continental water – A review [online]. U.S. Geological Survey, Water Supply Paper 2176. Available at: https://pubs.er.usgs.gov/publication/wsp2176 [accessed 16 February 2016].

Fetter, C.W. 1999. Contaminant hydrogeology (2nd ed.). Waveland Press, Inc., Long Grove, IL, USA.

Flynn, M.R., Surma, C. and Bara, B. 2015. The dynamic viscosity and yield stress of OSPW-diluted FFT collected from Base Mine Lake, Syncrude Canada Ltd., Internal Report.

Fredlund, D.G. and Rahardjo, H. 1993. Soil mechanics for unsaturated soils. John Wiley & Sons, Inc., Hoboken, NJ, USA.

Gailhanou, H., Blanc, P., Rogez, J., Mikaelian, G., Kawaji, H., Olives, J., Amouric, M., Denoyel, R., Bourrelly, S., Montouillout, V., Vieillard, P., Fialips, C.I., Michau, N. and Gaucher, E.C. 2012. Thermodynamic properties of illite, smectite and beidellite by calorimetric methods: Enthalpies of formation, heat capacities, entropies and Gibbs free energies of formation. Geochimica et Cosmochimica Acta, 89: 279-301.

Gammons, C.H., Harris, L.N., Castro J.M., Cott, P.A., and Hanna, B.W. 2009. Creating lakes from open pit mines: Processes and considerations - with emphasis on northern environments. Canadian Technical Report of Fisheries and Aquatic Scienc*es*, 2826.

Gammons, C.H., Poulson, S.R., Pellicori, D.A., Reed, P.J., Roesler, A.J. and Petrescu, E.M. 2006. The hydrogen and oxygen isotopic composition of precipitation, evaporated mine water, and river water in Montana, USA. Journal of Hydrology, 328(1-2): 319-330.

Gelhar, L.W., Welty, C. and Rehfeldt, K.R. 1992. A critical review of data on field‐scale dispersion in aquifers, Water Resources Research, 28(7): 1955-1974.

GEO-SLOPE International Ltd. 2014. Thermal modeling with TEMP/W, Version 2012 [computer program], GEO-SLOPE International Ltd., Calgary, AB, Canada.

GEO-SLOPE International Ltd. 2013. Seepage modeling with SEEP/W, Version 2012 [computer program], GEO-SLOPE International Ltd., Calgary, AB, Canada.

GEO-SLOPE International Ltd. 2012. Contaminant modeling with CTRAN/W, Version 2012 [computer program], GEO-SLOPE International Ltd., Calgary, AB, Canada.

Gibson, J.J. and Edwards, T.W.D. 2002. Regional water balance trends in evaporation-transpiration partitioning from a stable isotope survey of lakes in northern Canada, Global Biogeochemical Cycles. 16(2): 10-1–10-14.

Gibson, J.J., Edwards, T.W.D. and Prowse, T.D. 1996. Development and validation of an isotopic method for estimating lake evaporation. Hydrological Processes, 10(10): 1369-1382.

Gibson, J.J., Edwards, T.W.D., Birks, S.J., St. Amour, N.A., Buhay, W.M., McEachern, P., Wolfe, B.B. and Peters, D.L. 2005. Progress in isotope tracer hydrology in Canada. Hydrological Processes, 19(1): 303-327.

Gibson, J.J., Birks, S.J., Moncur, M. Yi, Y., Tattrie, K., Jasechko, S., Richardson, K. and Eby, P. 2011. Isotopic and geochemical tracers for fingerprinting process-affected waters in the oil sands industry: a pilot study. Oil Sands Research and Information Network, Report No. TR-12, University of Alberta School of Energy and the Environment, Edmonton, AB, Canada.

Gibson, R.E., Schiffman, R.L. and Cargill, K.W. 1981. The theory of one dimensional consolidation of saturated clays. II. Finite non-linear consolidation of thick homogeneous layers. Canadian Geotechnical Journal, 18(2): 280-293.

Gosselin, P., Hrudey, S.E., Naeth, M.A., Plourde, A., Therrien, R., Van Der Kraak, G. and Xu, Z. 2010. Environmental and Health Impacts of Canada's Oils Sands Industry. The Royal Society of Canada, Ottawa, ON, Canada.

Government of Alberta 2016. Alberta Energy: About our business – Oil sands [online]. Available at: www.energy.alberta.ca/About_Us/oilsands.asp. Accessed: May 23, 2016.

Government of Alberta, 2015. Lower Athabasca Region – Tailings management framework for the mineable Athabasca oil sands. Government of Alberta, ISBN: 978-1- 4601-2174-0.

Government of Alberta. 2014. Alberta's oil sands: Alberta's clean energy future [online]. Available at: http://oilsands.alberta.ca/reclamation.html. Accessed: May 23, 2016.

Gray, M.R. 2015. Upgrading oilsands bitumen and heavy oil. University of Alberta Press, Edmonton, AB, Canada.

Gražulis, S., Chateigner, D., Downs, R.T., Yokochi, A.F.T., Quirós, M., Lutterotti, L., Manakova, E., Butkus, J., Moeck, P. and Le Bail, A. 2009. Crystallography open database – An open-access collection of crystal structures. Journal of Applied Crystallography, 42(4), 726-729.

Han, X., MacKinnon, M.D. and Martin, J.W. 2009. Estimating the in situ biodegradation of naphthenic acids in oil sands process waters by HPLC/HRMS. Chemosphere, 76: 63-70.

Hendry, M.J. and Wassenaar, L.I. 2011. Millennial-scale diffusive migration of solutes in thick clay-rich aquitards: evidence from multiple environmental tracers. Hydrogeology Journal, 19(1): 259-270.

Hiraiwa, Y. and Kasubuchi, T. 2000. Temperature dependence of thermal conductivity of soil over a wide range of temperature (5-75°C). European Journal of Soil Science, 51(2): 211-218.

Huang, M., Hilderman, J.N. and Barbour, L. 2015. Transport of stable isotopes of water and sulphate within reclaimed oil sands saline-sodic mine overburden. Journal of Hydrology, 529(3): 1550-1561.

Incropera, F.P. and DeWitt, D.P. 2002. Fundamentals of Heat and Mass Transfer (5th ed.). John Wiley and Sons, Inc., Hoboken, NJ, USA.

ISO. 2015. 22007-2: Determination of thermal conductivity and thermal diffusivity - Part 2: Transient plane heat source (hot disc) method. International Organization for Standardization, Geneva, Switzerland.

Jacquet, N.G. 1976. Ground-water and surface-water relationships in the glacial province of northern Wisconsin – Snake Lake. Ground Water, 14(4): 194-199.

Jeeravipoolvarn, S., Scott, J.D. and Chalaturnyk, R.J. 2009. 10 m standpipe tests on oil sands tailings: Long-term experimental results and prediction. Canadian Geotechnical Journal, 46(8): 875-888.

Kachhwal, L.K., Yanful, E.K. and Lanteigne, L. 2011. Water cover technology for reactive tailings management: A case study of field measurement and model predictions. Water, Air & Soil Pollution, 214(1-4): 357-382.

Kamp, G. van der, Luba, L.D., Cherry, J.A. and Maathuis, H. 1994. Field study of a long and very narrow contaminant plume. Groundwater, 32(6): 1008-1016.

Kasperski, K.L. and Mikula, R.J. 2011. Waste streams of mined oil sands: Characteristics and remediation. Elements, 7(6): 387-392.

Kavanagh, R.J., Frank, R.A., Oakes, K.D., Servos, M.R., Young, R.F., Fedorak, P.M., MacKinnon, M.D., Solomon, K.R., Dixon, D.G. and Van Der Kraak, G. 2011. Fathead minnow (Pimephales promelas) reproduction is impaired in aged oil sands process-affected waters. Aquatic Toxicology, 101(1): 214-220.

Kluitenberg, G.J., Ham, J.M. and Bristow, K.L. 1993. Error analysis of the heat pulse method for measuring soil volumetric heat capacity. Soil Science Society of America Journal, 57(6): 1444-1451.

Lawrence, G.A., Tedford, E.W. and Pieters, R. 2016. Suspended solids in an end pit lake: potential mixing mechanisms. Canadian Journal of Civil Engineering, 43(3): 211-217.

Lee, D.R., Cherry, J.A. and Pickens, J.F. 1980. Groundwater transport of a salt tracer through a sandy lakebed. Limnology and Oceanography, 25(1): 45-61.

Li, M., Barbour, S.L. and Si, B.C. 2015. Measuring solid percentage of oil sands mature fine tailings using the dual probe heat pulse method. Journal of Environmental Quality, 44: 293-298.

Li, Y.H. and Gregory, S. 1974. Diffusion of ions in sea-water and in deep-sea sediments. Geochimica et Cosmochimica Acta, 38: 703-714.

Liu, G. and Si., B.C. 2011. Single-and dual-probe heat pulse probe for determining thermal properties of dry soils. Soil Science Society of America Journal, 75(3): 787-794.

Liu, G., Si, B.C., Jiang, A.X., Li, B.G., Ren, T.S. and Hu, K.L. 2012. Probe body and thermal contact conductivity affect error of heat pulse method based on infinite line source approximation. Soil Science Society of America Journal, 76(2): 370-374.

Locat, J. and Demers, D. 1988. Viscosity, yield stress, remolded strength, and liquidity index relationships for sensitive clays. Canadian Geotechnical Journal, 25(4): 799-806.

Masliyah, J., Zhou, Z., Xu, Z., Czarnecki, J. and Hamza, H. 2004. Understanding water-based bitumen extraction from Athabasca Oil Sands. The Canadian Journal of Chemical Engineering, 82(4): 628-54.

McAnally, W.H., Friedrichs, C., Hamilton, D., Hayter, E., Shrestha, P., Rodriguez, H., Sheremet, A. and Teeter, A. 2007. Management of fluid mud in estuaries, bays and lakes. I: Present state of understanding on character and behaviour. Journal of Hydraulic Engineering, 133(1): 9-22.

McCutcheon, S.C., Martin, J.L. and Barnwell, T.O. Jr. 1993. Water quality. In: Maidment, D.R. (Ed.), Handbook of Hydrology, McGraw-Hill, New York, NY, USA, p. 11.3.

McGuire, K.J., McDonnell, J.J., Weiler, M., Kendall, C., McGlynn, B.L., Welker, J.M. and Seibert, J. 2005. The role of topography on catchment-scale water residence time. Water Resources Research, 41(5), W05002, DOI: 10.1029/2004WR003657.

McKay, L.D., Gillham, R.W. and Cherry, J.A. 1993. Field experiments in a fractures clay till: 2. Solute and colloid transport. Water Resources Research, 29(12): 3879-3890.

McLinn, E.L. and Stolzenberg, T.R. 2009. Ebullition-facilitated transport of manufactured gas plant tar from contaminated sediment. Environmental Toxicology and Chemistry, 28(11): 2298-2306.

Mian, M.H. and Yanful, E.K. 2007. Erosion characteristics and resuspension of sub-aqueous mine tailings. Journal of Environmental Engineering and Science, 6(2): 175-190.

Midttømme, K., Roaldset, E. and Aagaard, P. 1998. Thermal conductivity of selected claystones and mudstones from England. Clay Minerals, 33(1): 131-145.

Mikula, R.J., Muñoz, V.A. and Omotoso, O. 2009. Centrifugation options for production of dry stackable tailings in surface-mined oil sands tailings management. Journal of Canadian Petroleum Technology, 48(9): 19-23.

Millero, F.J., Perron, G. and Desnoyers, J.E. 1973. Heat capacity of seawater solutions from 5° to 35°C and 0.5 to 22‰ chorinity. Journal of Geophysical Research, 78(21): 4499-4507.

Mills, R. 1973. Self-diffusion in normal and heavy water in the range 1-45°. The Journal of Physical Chemistry, 77(5): 685-688.

Morgenstern, N.R. and Nixon, J.F. 1971. One-dimensional consolidation of thawing soils. Canadian Geotechnical Journal, 8(4): 558-565.

Murray, W.A. 1981. The 1981 snowpack survey in the AOSERP study area. Alberta Environment, Research Management Division.

Nield, D.A. 1968. Onset of thermohaline convection in a porous medium. Water Resources Research, 4(3): 553-560.

Osacky, M., Geramian, M., Dyar, M.D., Sklute, E.C., Valter, M., Ivey, D.G., Liu, Q. and Etsell, T.H. 2013*a*. Characterisation of petrologic end members of oil sands from the Athabasca region, Alberta, Canada. The Canadian Journal of Chemical Engineering, 91(8), 1402-1415.

Osacky, M., Geramian, M., Ivey, D.G., Liu, Q. and Etsell, T.H. 2013*b*. Mineralogical and chemical composition of petrologic end members of Alberta oil sands. Fuel, 113: 148-157.

Oswald, C.J. and Rouse, W.R. 2004. Thermal characteristics and energy balance of various-size Canadian Shield lakes in the Mackenzie River Basin. Journal of Hydrometeorology, 5(1): 129-144.

Peacey, V., Yanful, E.K. and Payne, R. 2002. Field study of geochemistry and solute fluxes in flooded uranium mine tailings. Canadian Geotechnical Journal, 39: 357-376.

Peinerud, E. 2003. Water covers: A literature review on subaqueous tailings disposal. MiMi-Report, 2003:5. Luleå, Sweden (ISSN 1403-9478, ISBN 91-89350-29-4).

Penman, H.L. 1948. Natural evaporation from open water, bare soil and grass. Proceedings of the Royal Society of London, Series A, 193: 120-145.

Penner, T.J. And Foght, J.M. 2010. Mature fine tailings from oil sands processing harbour diverse methanogenic communities. Canadian Journal of Microbiology, 56(6): 459-470.

Plantier, F., Bessières, D., Daridon, J.L. and Montel, F. 2008. Structure and thermodynamic consistency of heavy oils: A study on the basis of acoustic measurements. Fuel, 87(2): 196-201.

Pop, I. and Ingham, D.B. 2001. Convective heat transfer: Mathematical and computational modelling of viscous fluids and porous media. Elsevier Science Ltd., Oxford, UK, p. 3.

Prakash, S., Vendenberg, J.A. and Buchak, E. 2011. The oil sands pit lake model – sediment diagenesis module. In: Chan, F., Marinova, D. and Anderssen, R.S. (Eds.), 19th International Congress on Modelling and Simulation, Modelling and Simulation Society of Australia and New Zealand, Perth, Australia, 3761-3767.

Province of Alberta. 2014. Environmental protection and enhancement act: Conservation and reclamation regulation. Alberta Regulation 115/1993 – 160/2014, Alberta Queen's Printer, Edmonton, Canada.

Ramos-Padrón, E., Bordenave, S., Lin, S., Bhaskar, I.M., Dong, X., Sensen, C.W., Fournier, J., Voordouw, G. and Gieg, L.M. 2011. Carbon and sulfur cycling by microbial communities in a gypsum-treated oil sands tailings pond. Environmental Science & Technology, 45(2): 439-446.

Rathore, M.M. and Kapuno, R.R.A. 2011. Engineering Heat Transfer (2nd ed). Jones & Bartlett Learning, Sudbury, MA, USA.

Raymond, J., Robert, G., Therrien, R. and Gosselin, L. 2010. A novel thermal response test using heating cables. In: Proceedings of the World Geothermal Congress, Bali, Indonesia, 25 – 30 April 2010. International Geothermal Association, Bochum, Germany.

Raymond, J., Therrien, R. and Gosselin, L. 2011. Borehole temperature evolution during thermal response tests. Geothermics, 40(1): 69-78.

Ren, T., Ochsner, T. E., Horton, R. and Ju., Z. 2003. Heat-pulse method for soil water content measurement: Influence of the specific heat of the soil solids. Soil Science Society of America Journal, 67(6): 1631-1634.

Richet, P., Bottinga, Y., Denielou, L., Petitet, J.P. and Tequi, C. 1982. Thermodynamic properties of quartz, cristobalite and amorphous SiO_2: drop calorimetry measurements between 1000 and 1800 K and a review from 0 to 2000 K. Geochimica et Cosmochimica Acta, 46(12): 2639-2658.

Rimmer, A., Aota, Y., Kumagai, M. and Eckert, W. 2005. Chemical stratification in thermally stratified lakes: A chloride mass balance model. Limnology and Oceanography, 50(1): 147-157.

Robie, R.A. and Hemingway, B.S. 1991. Heat capacities of kaolinite from 7 to 380 K and of DMSO-intercalated kaolinite from 20 to 310 K. The entropy of kaolinite $Al_2Si_2O_5(OH)_4$. Clays and Clay Minerals, 39(4): 362-368.

Rouse, W.R., Oswald, C.M., Binyamin, J., Blanken, P.D., Schertzer, W.M. and Spence, C. 2003. Interannual and seasonal variability of the surface energy balance and temperature of central Great Slave Lake. Journal of Hydrometeorology, 4(4): 720-730.

Saar, M.O. 2011. Review: Geothermal heat as a tracer of large-scale groundwater flow and as a means to determine permeability fields. Hydrogeology Journal, 19(1): 31-52.

Sacks, L.A., Swancar, A. and Lee, T.M. 1998. Estimating ground-water exchange with lakes using water-budget and chemical mass-balance approaches for ten lakes in ridge areas of Polk and Highlands Counties, Florida [online]. U.S. Geological Survey, Water-Resources Investigations Report 98-4133. Available at: https://pubs.er.usgs.gov/publication/wri984133 [accessed 16 February 2016].

Samad, M.A. and Yanful, E.K. 2005. A design approach for selecting the optimum water cover depth for subaqueous disposal of sulfide mine tailings. Canadian Geotechnical Journal, 42: 207-228.

Sarsby, R. 2000. Environmental geotechnics. Thomas Tedford Publishing, London, UK.

Scandella, B.P., Varadharajan, C., Hemond, H.F., Ruppel, C. and Juanes, R. 2011. A conduit dilation model of methane venting from lake sediments. Geophysical Research Letters, 38(6): L06408.

Schiffman, R.L. 1982. The consolidation of soft marine sediments. Geo-Marine Letters, 2 (3-4): 199-203.

Schiffman, R.L. and Pane, V. 1985. Non-linear finite strain consolidation of soft marine sediments. In: Denness, B. (Ed.), Seabed Mechanics (Part II). International Union of Theoretical and Applied Mechanics, Newcastle upon Tyne, UK, 123-130.

Siddique, T., Fedorak, P.M. and Foght, J.M. 2006. Biodegradation of short-chain n-alkanes in oil sands tailings under methanogenic conditions. Environmental Science & Technology, 40(17): 5459-5464.

Siddique, T., Fedorak, P.M., MacKinnon, M.D. and Foght, J.M. 2007. Metabolism of BTEX and naphtha compounds to methane in oil sands tailings. Environmental Science and Technology, 41(7): 2350-2356.

Siddique, T., Penner, T., Semple, K. and Foght, J.M. 2011. Anaerobic biodegradation of longer-chain n-alkanes coupled to methane production in oil sands tailings. Environmental Science and Technology, 45(13): 5892-5899.

Siddique, T., Kuznetsov, P., Kuznetsova, A., Arkell, N., Young, R., Li, C., Guigard, S., Underwood, E. and Foght, J.M. 2014*a*. Microbially-accelerated consolidation of oil sands tailings. Pathway I: changes in porewater chemistry. Frontiers in Microbiology, 5 (Article 106).

Siddique, T., Kuznetsov, P., Kuznetsova, A., Li, C., Young, R., Arocena, J.M. and Foght, J.M. 2014*b*. Microbially-accelerated consolidation of oil sands tailings. Pathway II: solid- phase biogeochemistry. Frontiers in Microbiology, 5 (Article 107).

Song, Y., Ham, J.M., Kirkham, M.B. and Kluitenberg, G.J. 1998. Measuring soil water content under turfgrass using the dual-probe heat-pulse technique. Journal of the American Society for Horticultural Science, 123(5): 937-941.

Spellman, F.R. and Whiting, N.E. 2014. Handbook of mathematics and statistics for the environment. CRC Press, Taylor & Francis Group, Boca Raton, FL, USA.

Sridharan, A. and Prakash, K. 2003. Self weight consolidation: Compressibility behaviour of segregated and homogeneous finegrained sediments. Marine Georesources and Geotechnology, 21(2): 3-80.

Stallman, R.W. 1965. Steady one-dimensional fluid flow in a semi-infinite porous medium with sinusoidal surface temperature. Journal of Geophysical Research, 70(12): 2821-2827.

Stasik, S. and Wendt-Potthoff, K. 2014. Interaction of microbial sulphate reduction and methanogenesis in oil sands tailings ponds. Chemosphere, 103: 59-66.

Stasik, S., Loick, N., Knöller, K., Weisener, C. and Wendt-Potthoff, K. 2014. Understanding biogeochemical gradients of sulfur, iron and carbon in an oil sands tailings pond. Chemical Geology, 382: 44-53.

Steffe, J.F. 1996. Rheological Methods in Food Process Engineering (2nd ed.). Freeman Press, East Lansing, MI, USA.

Stonestrom, D. A. and Constantz, J. 2003. Heat as a tool for studying the movement of ground water nears streams. U.S. Geological Survey Circulation, 1260: 1-96.

Sudicky, E.A and Illman, W.A. 2011. Lessons learned from a suite of CFB Borden experiments. Groundwater, 49(5): 630-648.

Suthaker, N.N. and Scott, J.D. 1996. Measurement of hydraulic conductivity in oil sand tailings slurries. Canadian Geotechnical Journal, 33(4): 642-653.

Suzuki, S. 1960. Percolation measurements based on heat flow through soil with special reference to paddy fields. Journal of Geophysical Research, 65(9): 2883-2885.

Sworska, A., Laskowski, J.S. and Cymerman, G. 2000. Flocculation of the Syncrude fine tailings – Part I. Effect of pH, polymer dosage and Mg^{2+} and Ca^{2+} cations. International Journal of Mineral Processing, 60(2): 143-152.

Taylor, R.G. and Howard, K.W.F. 1996. Groundwater recharge in the Victoria Nile basin of east Africa: support for the soil moisture balance approach using stable isotope tracers and flow modelling. Journal of Hydrology, 180(1-4): 31-53.

Van Der Kamp, G., Luba, L.D., Cherry, J.A. and Maathuis, H. 1994. Field study of a long and very narrow contaminant plume. Groundwater, 32(6): 1008-1016.

Von Stockar, U., Marison, I.W. and Liu, J.S. 2000. Endothermic microbial growth. A calorimetric investigation of an extreme case of entropy-driven microbial growth. Pure and Applied Chemistry, 72(10): 1835-1838.

Wassenaar, L.I., Hendry, M.J., Chostner, V.I. and Lis, G.P. 2008. High resolution pore water δ^2H and $\delta^{18}O$ measurements by H_2O(liquid)-H_2O(vapor) equilibration laser spectroscopy. Environmental Science & Technology, ASC, 42: 9262-9267.

Wong, R.C.K., Mills, B.N. and Liu, Y.B. 2008. Mechanistic model for one-dimensional consolidation behaviour of nonsegragating oil sands tailings. Journal of Getoechnical and Geoenvironmental Engineering, 134(2): 195-202.

Wu, J., Liu, Z., Jin, X. and Pan, J. 2005. Thermal conductivity of some oxygenated fuels and additives in the saturated liquid phase. Journal of Chemical and Engineering Data, 50(1): 102-104.

Yanful, E.K. and Catalan, L.J.J. 2002. Predicted and field-measured resuspension of flooded mine tailings. Journal of Environmental Engineering, 128(4): 341-351.

Yuan, Q., Valsaraj, K.T., Reible, D.D. and Willson, C.S. 2007. A laboratory study of sediment and contaminant release during gas ebullition. Journal of the Air & Waste Management Association, 57(9): 1103-1111.

APPENDIX A: NUMERICAL MODELLING DETAILS

In-situ Thermal Properties Experiment (Chapter 2)

GeoStudio© TEMP/W and SEEP/W were used to simulate the heating and cooling trends through the FFT. An axisymmetric domain was established with a central offset of 0.0005 m (the radius of the heating wire), which was necessary for applying a heating rate along the inside boundary. The domain was 5 m tall with the top 1 m representing the bottom of the lake water, and the rest of the domain was FFT (3 m of FFT were beside the heating wire and 1 m was below it). The domain radius was 3.5 m which was tested to ensure that this was a far-field boundary. The mesh was discretized to 0.004 m quadrilaterals.

SEEP/W analyses were included in the model to generate continuously changing FFT properties with depth (constant over time). Pressure head boundary conditions were set throughout the domain to establish changing pore water pressures with depth: (1) –0.3 m at the top of the domain (y = 1 m); (2) –0.4 m at the top of the FFT (y = 0 m); and (3) –1 m at the bottom of the heating wire (y = –3 m). A volumetric water content function was inputted to establish the expected change in volumetric water content with depth given the pressure heads generated with these boundary conditions (Figure A-1). Functions were also created for thermal conductivity and volumetric heat capacity (versus volumetric water content) such that the simulated thermal properties continuously changed with depth.

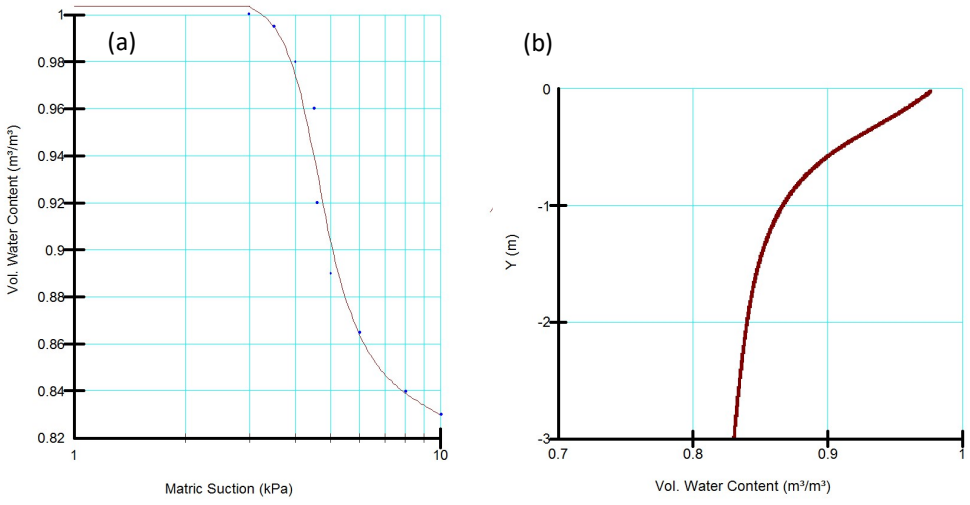

Figure A-1. (a) Volumetric water content function over the generated range of suctions, and (b) the associated water contents with depth along the simulated heating wire.

The initial temperatures throughout the domain were set using a spatial function, given the field measurements immediately before the heating test began. The first TEMP/W analysis ran for two hours with exponentially increasing time intervals (61 intervals with an initial increment size of 12 s). A heating flux of 2860 J/s/m^2 was applied along the central boundary of the domain. This value was determined by dividing the measured heating rate (9 J/s/m) by the circumference the energy was applied to (given the wire radius of 0.0005 m). A subsequent 300-second TEMP/W analysis simulated the FFT cooling immediately after the heating wire was disconnected from the power source, using the final temperatures from the first TEMP/W analysis as the initial conditions. This analysis had 30 time intervals, exponentially increasing in size from an initial time increment of 5 s. Another TEMP/W analysis was added after this one to simulate FFT cooling for a total of 4 hours after heating stopped. The second cooling analysis had linear time intervals of 90 s. The flux boundary condition was removed for both of the cooling analyses.

Isotope Transport Model (Chapter 3)

The isotope simulations were completed with the GeoStudio© SEEP/W and CTRAN/W products. The model domain included the top 5 m of FFT, separated into five regions (all 1 m deep), and the entire overlying water cover (8.5 m). The regions were discretized so as to generate a one-dimensional FFT/water column, by specifying the number of divisions as 1 for each of the horizontal lines. The vertical mesh element size was set to 0.01 m for the water cover and the top two FFT regions, while the bottom three FFT regions were discretized in 0.05 m intervals.

A steady-state SEEP/W analysis produced the constant flow conditions through the column. The pressure head at the top of the domain was set to 0 m. A constant flux (q) boundary condition was applied at the FFT bottom, ranging from 0.002 to 0.01 m/d. A saturated-only material model was used for the analysis. The hydraulic conductivity of FFT does change with void ratio (water content); however, a constant saturated hydraulic conductivity was applied throughout the entire FFT profile (1 m/day) as a constant flow was imposed in both analyses. The volumetric water content of each FFT region decreased with depth (Table 3-1) while the water content of the water cover was set as 1 m^3/m^3.

The seepage results from the SEEP/W analysis were used by the subsequent transient advection-dispersion CTRAN/W analysis (except for the diffusion-only case which only included a CTRAN/W analysis similar to described below). Advection-dispersion was modelled over a 1-year period, with time increments of 1 day. The coefficient of molecular diffusion for each FFT region was set based on the volumetric water content and average temperature through the FFT (Table 3-1). The diffusion coefficient in the water cover was either: (1) 0.000125 m^2/d to represent stratification; or (2) 1 m^2/d to represent fully mixed lake conditions. The longitudinal dispersivity was set as 0.003 m for all of the FFT regions, and 1 m for the water cover. Stable isotopes of water are considered a conservative species so adsorption was set to 0 g/g for all regions.

The initial conditions were set using the activation concentration option in the KeyIn Materials window. Normalized concentrations were used for the mass transport analysis, so the five FFT regions and the water cover had activation concentrations of 1 g/m^3 and 0 g/m^3, respectively. A mass flux boundary condition was applied at the bottom of the domain to correspond to the seepage rate (e.g., 0.002 m/d of seepage corresponded to a mass flux of 0.002 g/m/d).

Mixing events in the FFT were simulated by modifying the original model. At the time of the mixing event (day 110), the simulated transition from the lake concentration to that of the FFT was less than the two mixing depths (less than 0.5 m from the interface). Thus, the CTRAN/W model was modified to start at the time of the mixing event. The analysis duration was changed to 255 days (with 1-day time intervals). The initial concentrations were 1 g/m^3 in the unaffected FFT regions, and 0 g/m^3 in the mixed FFT and the lake water.

Seasonal Heat Transport Model (Chapter 3)

GeoStudio© SEEP/W and TEMP/W were used to simulate heat transport through the FFT. The model domain included the top 5 m of FFT, separated into five regions (all 1 m deep). Similar to the isotope transport model, the regions were discretized to generate one-dimensional heat and water flow by specifying the number of divisions as 1 for each horizontal line. The vertical mesh element size was set to 0.1 m.

The materials were defined using the simplified thermal and saturated-only material models for the TEMP/W and SEEP/W analyses, respectively. The volumetric water content

specified for each region decreased with depth from 0.86 to 0.82 m^3/m^3 (Table 3-1). The thermal properties also changed with depth based on the volumetric water content (Table 3-1). The same value was entered for the frozen and unfrozen thermal properties as the tailings do not reach temperatures below 0 ºC. Similar to the isotope transport model, a constant saturated hydraulic conductivity was applied throughout the entire FFT profile ($1x10^{-7}$ m/s).

An initial steady-state TEMP/W analysis was used to generate the initial temperature profile through the FFT. These temperatures were set based on field measurements at the beginning of the simulated period (Figure A-2). An initial steady-state SEEP/W analysis was used to generate the constant flow conditions associated with convective heat flux for the subsequent TEMP/W analysis. A constant pressure head boundary condition was applied to the top of the domain (8 m) to represent the lake level. A constant water flux was specified at the FFT bottom (0.002 to 0.01 m/d), similar to the steady-state SEEP/W analysis in the isotope transport model.

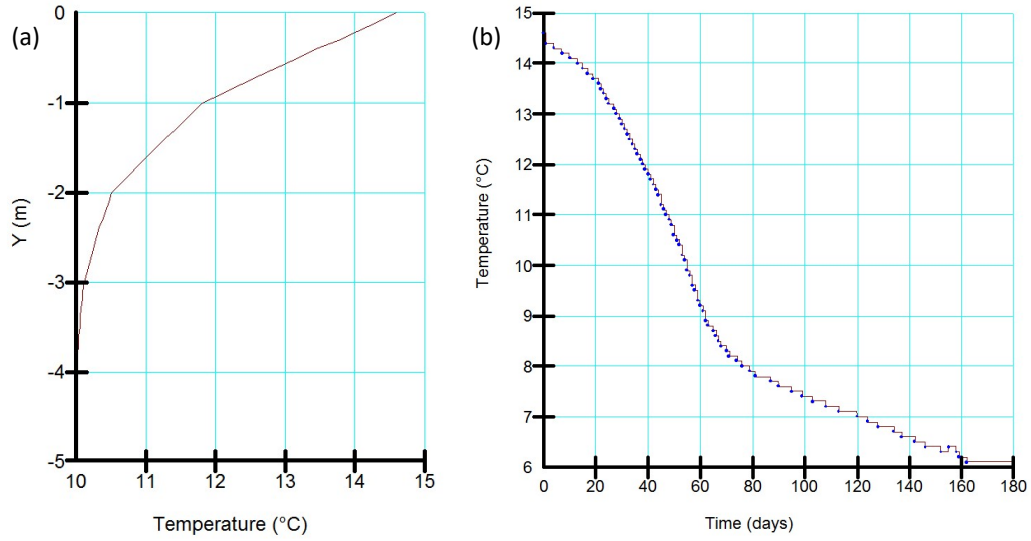

Figure A-2. Boundary conditions applied to the heat transport model: (a) the initial temperature conditions through the FFT; and (b) the temperature applied at the top of the domain over time.

A coupled Convective Heat Transfer analysis (TEMP/W + SEEP/W) followed the steady-state SEEP/W analysis. This transient analysis ran for 170 days, with linearly specified time intervals of half a day. A constant temperature boundary condition (10 °C) was applied at the bottom of the modelled domain. The top temperature boundary condition was specified as a

function given the measured lake temperatures over time (Figure A-2). The pore water flux applied at the bottom of the FFT column remained the same as in the steady-state SEEP/W analysis (0.002 to 0.01 m/d) and the same flux (but negative to represent water flowing out of the domain) was also applied at the top boundary. For the conduction-only heat transport regime, only TEMP/W analyses were used (as described above).

In order to include a mixing event within the FFT, a secondary Convective Heat Transfer analysis was added to the model. A spatial temperature function was used to set the initial temperature conditions of this analysis. The temperature results from the original Convective Heat Transfer analysis at day 30 (corresponding to October 15, 2013) were used as the initial temperatures for the bottom portion of the FFT column (regions unaffected by mixing) and the temperature within the mixed zone (from y = 0 m to either y = –0.5 or –1 m) was set to the temperature in the lake on this day (12.8 °C). The second Convective Heat Transfer analysis ran for 140 days with half-day intervals. Otherwise, this analysis was the same as the original Convective Heat Transfer analysis.

Chloride Transport Model (Chapter 4)

GeoStudio Preview (early release of GeoStudio 2017) was used to assess chloride transport through the FFT. Similar to the isotope and heat transport simulations, the top 5 m of the FFT was modelled with flow only in the vertical dimension. The model was set up as a true one-dimensional model (available only in GeoStudio Preview/2017). The material properties of the FFT were set to continuously change using the (negative) pressure profile to specify the saturated volumetric water content with depth through the domain. The FFT profile was turned upside-down in the model so that seepage could be incorporated (the seepage was included as an infiltration flux on the top of the profile).

An initial steady-state SEEP/W model was used to specify the pressures through the domain. A constant pressure head of –7 m was applied at the FFT-water interface (bottom of the modelled domain). The top boundary, representing FFT at 5 m depth, had a constant pressure head of –12 m. This generated a linearly changing pressure head profile, which was used to specify a continuously changing volumetric water content with depth by selecting the saturated-unsaturated material model and specifying a volumetric water content function (Figure A-3). A

constant hydraulic conductivity of 0.1 m/s was specified for all pore water pressures (so it did not change with depth).

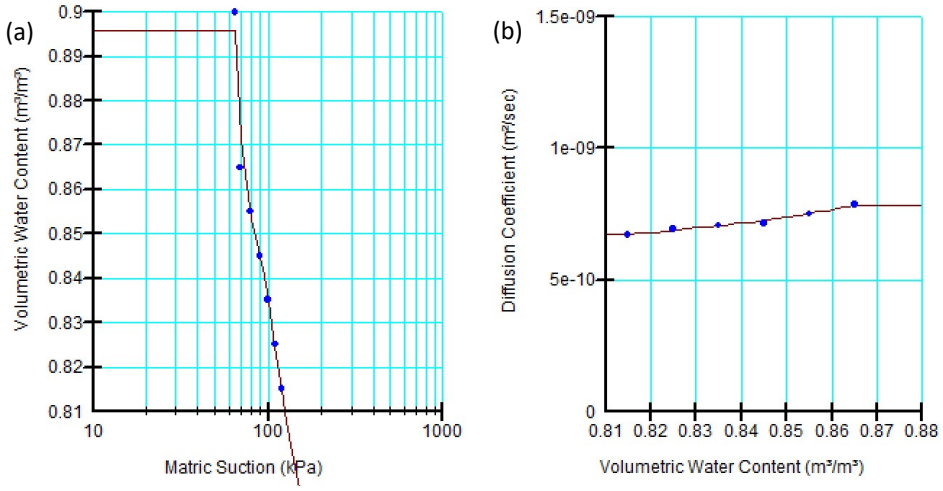

Figure A-3. The volumetric water content and diffusion coefficient functions inputted to generate continuously changing FFT properties with depth.

A second analysis was developed in CTRAN/W using both the solute and water transfer options (defined in the KeyIn Analyses window). This analysis ran for 885 days (from May 29, 2013 to October 31, 2015) with linear time steps (12 minutes). The same saturated-unsaturated material model from the steady-state seepage model was used to define the hydraulic properties in the transient CTRAN/W analysis. The solute transport parameters were specified as: (1) 0.004 m for longitudinal dispersivity; (2) 0 g/g adsorption; and (3) a diffusion coefficient function was defined over the modelled volumetric water content range such that the coefficient changed with depth (Figure A-3).

The initial hydraulic conditions of the CTRAN/W analysis were obtained from the steady-state seepage analysis, and the initial concentrations were set using a spatial function, with a normalized concentration of 1 g/m^3 specified through the entire FFT column. A constant water flux was applied at the top boundary (between 0 and 0.01 m/d) while the original pressure head imposed at the domain bottom was maintained throughout the CTRAN/W analysis. A constant concentration boundary condition of 1 g/m^3 was applied at the top of the model domain (FFT at 5 m depth). Two functions were defined for normalized concentration over time at the FFT-water

interface (bottom of the domain) based on field measurements collected in the water cover (Figure A-4).

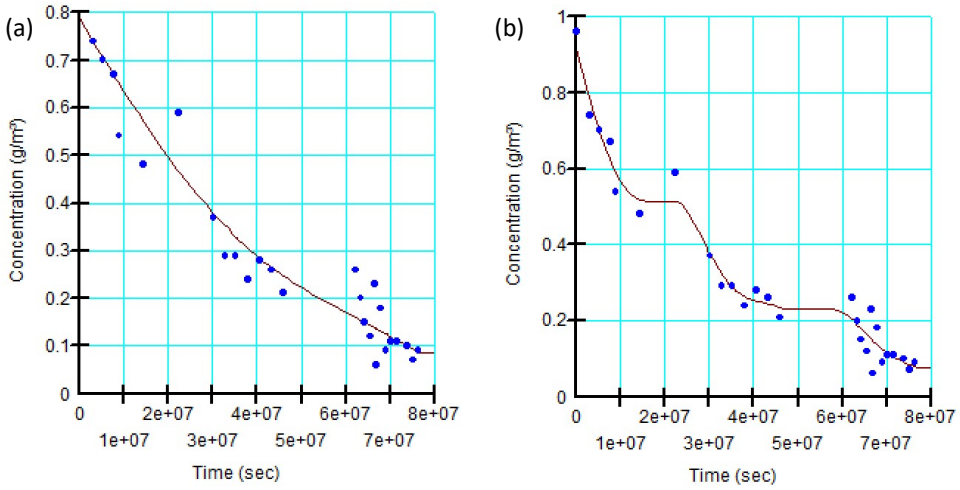

Figure A-4. Spline boundary functions applied to the FFT-water interface: (a) gradually changing concentration over time (approximate spline with a 27% exact curve fit and 57% curved line segments); and (b) intermittently declining concentration (approximate spline with a 50% exact curve fit and 30% curved line segments).

Mixing events were added on October 15, 2013 (day 150) and October 15, 2014 (day 515). The CTRAN/W model was broken up into three analyses: (1) before any mixing event, days 1 to 150; (2) after the first mixing event and before the second, days 151 to 515; and (3) after the second mixing event, days 516 to 885. The same boundary conditions and material models were applied to the domain. The initial conditions for the three analyses were set using spatial functions. The initial spatial function was the same as used by the original CTRAN/W model. The spatial functions used to reset the FFT pore water concentrations after a mixing event were calculated with the results from the previous analysis. The normalized FFT pore water concentration in the disturbed zone, $C_{FFT}{}'$, after a mixing event was calculated by:

$$C_{FFT}{}' = \frac{C_{lake} \cdot d_{lake} + C_{FFT\,avg} \cdot d_{mixing} \cdot n}{d_{lake} + d_{mixin} \cdot n} \qquad \text{(A.1)}$$

where C_{lake} is the normalized concentration of the lake on the day of the mixing event (mg/L), d_{lake} is the depth of the lake (8.5 m), $C_{FFT\,avg}$ is the average normalized FFT pore water

concentration in the disturbed zone simulated the day before the mixing event (mg/L), d_{mixing} is the depth of the disturbed zone (either 0.5 or 1 m), and n is the porosity of the FFT in the disturbed zone (0.86).

APPENDIX B: BASE MINE LAKE PIT CAPACITY CURVE

The pit capacity curve for BML was provided by Syncrude Canada Ltd. and can be found in the following report: *2015 Base Mine Lake: FFT Physical Assessment Report. June 2016. Barr Engineering Company, Calgary, AB.*

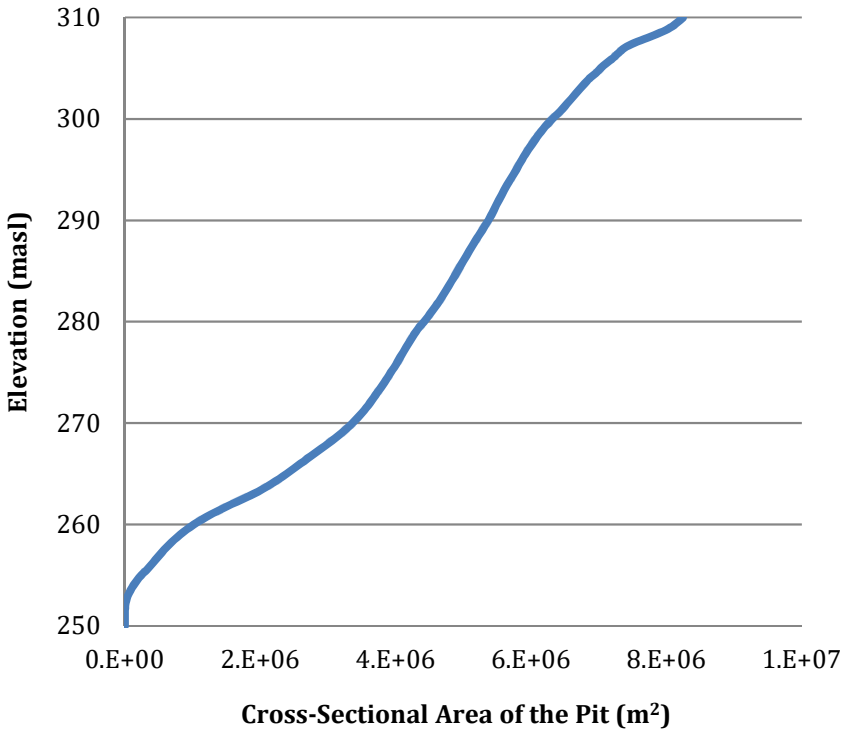

Figure B-1. Base Mine Lake mine pit capacity curve.

APPENDIX C: IN ERRATUM

2.3.1, p. 21: The sample volume was 1000 mL.

2.3.3, p. 24: No spacers were used in the deployed system.

2.4.1, p. 26: The FFT samples were collected from six locations, not three.

Figure 2-11, p. 38: The high-resolution FFT samples were collected according to the Fixed Interval Fluid Sampling™ methods described in 3.3.1.

Figure 2-12, p. 39: The data presented in this figure are from all thermistors along the heating wire. The grey lines are not colour-coded in any way.

2.4.3.2, p. 40: The models discussed in the second paragraph of the numerical modelling section (results presented in Figure 2-13) were homogeneous models that were run multiple times with varying properties.

2.5, p. 46: The first sentence in the third paragraph should read: "The in-situ experiment and associated numerical model produced initial estimates of thermal conductivity with depth through the FFT, and demonstrated that in-situ testing of thermal *conductivity* is possible in soft sediments or tailings."

3.3.3, p. 58: The temperatures were monitored from September 16, 2013 to March 5, 2014. The system was installed with the intent to measure temperatures over a full year but ice damage of the thermistor string prevented this.

3.3.5, p. 62: Only one mixing event, on Oct. 15, 2013, was included in each model.

3.4.1, p. 63: The statement "Pore water pressure in the FFT increases with depth due to the self-weight of the tailings" should include the following reference: Geoff Halferdahl, Syncrude Canada Ltd.

Figure 3-12, p. 74: The maximum and minimum points are the maximum and minimum values measured in the field at each individual thermistor or simulated at each individual node by the numerical models. They do not necessarily correspond to the same time interval.